Silicon Nano-Photonic Devices

Pu, Minhao

Publication date:
2011

Document Version
Publisher's PDF, also known as Version of record

Technical University of Denmark

Silicon Nano-Photonic Devices

by

Minhao Pu

A thesis submitted in partial fulfillment for the
degree of Doctor of Philosophy

in the

DTU Fotonik
Department of Photonics Engineering

November 2010

Abstract

This thesis deals with the design, fabrication and characterization of nano-photonic devices including ridge waveguide components, microring resonators, and photonic crystal components, and explore the potential for these devices in different applications ranging from optical communication to microwave systems and biosensing devices.

An ultra-low loss inverse taper coupler for interfacing silicon ridge waveguides and optical fibers is introduced and insertion losses of less than 1 dB are achieved for both transverse-electric (TE) and transverse-magnetic (TM) polarizations. Integrated with the couplers, a silicon ridge waveguide is utilized in nonlinear all-optical signal processing for optical time division multiplexing (OTDM) systems. Record ultra-high-speed error-free optical demultiplexing and waveform sampling are realized and demonstrated for the first time.

Microwave phase shifters and notch filters based on tunable microring resonators are proposed and analyzed. Based on a single microring resonator, a maximum radio frequency (RF) phase shift of 336° is obtained, but with large power variation. By utilizing a dual-microring resonator, a RF phase shifting range larger than 2π is achieved with small power variation. A widely tunable microwave notch filter is also experimentally demonstrated at 40 GHz. Other application such as pulse repetition rate multiplication by using microring resonator is also presented.

Photonic crystal components are studied. Two different types of photonic crystal structures are analyzed concerning index sensitivity, dispersion engineering, and slow-light coupling. Several photonic crystal devices such as index sensor, slow-light coupler, and all-optical tunable cavity are presented.

Acknowledgements

During the last three years, I have enjoyed my time in DTU Fotonik and the chance to work with such a technically gifted group of people. The project would not have been possible without their help, so that I would like to take the opportunity to thank here.

First and foremost, I want to thank Professor Jørn M. Hvam for offering me the Ph.D position in DTU Fotonik, a wonderful place for study and research. I am also grateful to my supervisors Professor Jørn M. Hvam, Associate Professor Kresten Yvind, Associate Professor Haiyan Ou for their continuous support and encouragement during my Ph.D project. I would like also thank Dr. Lars H. Frandsen, my previous co-supervisor, for guiding me along in the nanophotonic world and sharing his experiences in fabrication.

Special thanks to Assistant Professor Liu Liu, who did many advising work in the last year of my project. I have learnt a lot from him in theory, fabrication and characterization. Without his help, it would be much harder for me to finish this thesis work.

I am also very grateful to the people in high-speed optical communication group: Hua Ji, Hao Hu, Michael Galili, Leif Katsuo Oxenløwe, Palle Jeppesen. We had close cooperation within the "NANO·COM" project, and they have made great contributions to most of the system experiments for silicon waveguide- and microring-based high speed signal processing.

I also thank my colleagues Weiqi Xue, Lirong Yang, exchange PhD student Yunhong Ding for good collaborations in different projects. I would also thank Assistant Professor Sanshui Xiao, my colleagues Yaohui Chen, Yuntian Chen, Lei Wei, Martin Schubert for those inspiring discussions. In addition, I also acknowledge Jørn M. Hvam, Liu Liu, Martin Schubert for careful proofreading the thesis and providing many comments.

Thanks for my friends inside or outside Denmark. They have made my daily life rich and colorful.

Last but not the least, many thanks to Xiaoyu Xing and my family for their continuous support, encouragement, and patient through these years.

Ph.D Publications

Peer Reviewed Journal Publications

1. Liu Liu, ***Minhao Pu***, Kresten Yvind, and Jørn M. Hvam, "High-efficiency, large-bandwidth silicon-on-insulator grating coupler based on a fully-etched photonic crystal structure," *Applied Physics Letters* 96, 051126-3 (2010).

2. ***Minhao Pu***, Liu Liu, Weiqi Xue, Yunhong Ding, Lars H. Frandsen, Haiyan Ou, Kresten Yvind, and Jørn M. Hvam, "Tunable microwave phase shifter based on silicon-on-insulator microring resonator," *IEEE Photonics Technology Letters* 22, 869-871 (2010).

3. ***Minhao Pu***, Liu Liu, Weiqi Xue, Yunhong Ding, Haiyan Ou, Kresten Yvind, and Jørn M. Hvam, "Widely tunable microwave phase shifter based on silicon-on-insulator dual-microring resonator," *Optics Express* 18, 6172-6182 (2010).

4. ***Minhao Pu***, Liu Liu, Weiqi Xue, Haiyan Ou, Kresten Yvind, and Jørn M. Hvam, "Ultra-low-loss inverted taper coupler for silicon-on-insulator ridge waveguide," *Optics Communications* 283, 3678-3682 (2010).

5. Yunhong Ding, Christophe Peucheret, ***Minhao Pu***, Beata Zsigri, Jorge Seoane, Liu Liu, Jing Xu, Haiyan Ou, Xinliang Zhang, and Dexiu Huang, "Multi-channel WDM RZ-to-NRZ format conversion at 50 Gbit/s based on single silicon microring resonator," *Optics Express* 18, 21121-21130 (2010).

6. Hua Ji, Michael Galili, Hao Hu, ***Minhao Pu***, Leif K. Oxenløwe, Kresten Yvind, Jørn M. Hvam and Palle Jeppesen, "1.28 Tbit/s Demultiplexing of an OTDM DPSK Data Signal Using a Silicon Waveguide," *IEEE Photonics Technology Letters* 22, 1762-1764(2010).

7. Hua Ji, ***Minhao Pu***, Hao Hu, Michael Galili, Leif Katsuo Oxenløwe, Kresten Yvind, Jørn M. Hvam, and Palle Jeppesen, "Optical Waveform Sampling and Error-free Demultiplexing of 1.28

Tbit/s Serial Data in a Nano-engineered Silicon Waveguide," *IEEE Journal of Lightwave Technology* [invited] 29, 426-431 (2011).

8. Yunhong Ding, Jing Xu, Christophe Peucheret, ***Minhao Pu***, Jorge Seoane, Haiyan Ou, Xinliang Zhang, and Dexiu Huang, "Multi-Channel 40 Gbit/s NRZ-DPSK Demodulation Using a Single Silicon Microring Resonator," *IEEE Journal of Lightwave Technology* 29, 677-684 (2011).

9. Leif Katsuo Oxenløwe, Hua Ji, Michael Galili, ***Minhao Pu***, Hao Hu, Kresten Yvind, Anders T. Clausen, Jørn M. Hvam, and Palle Jeppesen, "Optical Waveform Sampling and Error-free Demultiplexing of 1.28 Tbit/s Serial Data in a Nano-engineered Silicon Waveguide," *IEEE Journal of Lightwave Technology* [invited] (in press).

Peer Reviewed Conference Publications

1. ***Minhao Pu***, H. Ji, Lars H. Frandsen, Michael Galili, Leif K. Oxenløwe, and Jørn. M. Hvam, "High-Q Microring Resonator with Narrow Free Spectral Range for Pulse Repetition Rate Multiplication," The conference on lasers and electro-optics (CLEO) 2009, CThBB7, Baltimore, MD, US.

2. Hua Ji, ***Minhao Pu***, Michael Galili, Leif K. Oxenløwe, and Palle Jeppesen, "Compact pulse repetition rate multiplication scheme using micro ring resonator," European Conference on Lasers and Electro-Optics (CLEO/Europe) 2009, CF.P.27, Munich, Germany.

3. ***Minhao Pu***, Lars. H. Frandsen, Haiyan Ou, Kresten Yvind, and Jørn. M. Hvam, "Low Insertion Loss SOI Microring Resonator Integrated with Nano-Taper Couplers," The Conference on Frontiers in Optics (FiO) 2009, FThE1, San Jose, CA, US.

4. Liu Liu, ***Minhao Pu***, Kresten Yvind, and Jørn M. Hvam, "Fully-etched photonic crystal grating coupler as an interface between single-mode fibers and photonic circuits on silicon-on-insulator," The Conference on Optical Fiber Communication (OFC) 2010, OWJ2, San Diego, CA, US.

5. ***Minhao Pu***, Lirong Yang, Lars H. Frandsen, Haiyan Ou, Kresten Yvind, and Jørn M. Hvam, "Topology-optimized slow-light couplers for ring-shaped photonic crystal waveguide," The Conference on Optical Fiber Communication (OFC) 2010, JWA30, San Diego, CA, US.

6. ***Minhao Pu***, Liu Liu, Haiyan Ou, Kresten Yvind, and Jørn M. Hvam, "Silicon-on-insulator ring-shaped photonic crystal waveguides for refractive index sensing," The Conference on Optical Fiber Communication (OFC) 2010, JWA20, San Diego, CA, US.

7. Hua Ji, Hao Hu, Michael Galili, Leif K. Oxenløwe, ***Minhao Pu***, Kresten Yvind, Jørn M. Hvam, and Palle Jeppesen, "Optical Waveform Sampling and Error-free Demultiplexing of 1.28 Tbit/s Serial Data in a Silicon Nanowire," The Conference on Optical Fiber Communication (OFC) 2010, PDPC7 (postdeadline paper), San Diego, CA, US.

8. Hua Ji, Michael Galili, ***Minhao Pu***, Leif K. Oxenløwe, Palle Jeppesen, "Silicon based ultrafast all-optical waveform multiple-shot sampling," The Conference on Photonics Europe, Nonlinear Optics and its Applications (the Best Student Paper), 7728-06, Brussels, Belgium.

9. Yunhong Ding, ***Minhao Pu***, Jing Xu, Christophe Peucheret, Haiyan Ou, Xinliang Zhang, and Dexiu Huang, "Bandwidth tunable filter based on silicon microring-MZI structure," The 15th European Conference on Integrated Optics (ECIO) 2010, ThP20, Cambridge, UK.

10. ***Minhao Pu***, Weiqi Xue, Liu Liu, Haiyan Ou, Kresten Yvind, and Jørn M. Hvam, "360 degree tunable microwave phase shifter based on silicon-on-insulator dual-microring resonator" The 15th European Conference on Integrated Optics (ECIO) 2010, WeD3, Cambridge, UK

11. ***Minhao Pu***, Liu Liu, Haiyan Ou, Kresten Yvind, and Jørn M. Hvam, "All-optical tunable photonic crystal cavity," The 15th European Conference on Integrated Optics (ECIO) 2010, WeP3, Cambridge, UK.

12. ***Minhao Pu***, Liu Liu, Weiqi Xue, Lars H. Frandsen, Haiyan Ou, Kresten Yvind, and Jørn M. Hvam, "Microwave photonic phase shifter based on tunable silicon-on-insulator microring resonator" The conference on lasers and electro-optics (CLEO) 2010, paper CThJ2, San Jose, CA, USA, (2010)

13. Hua Ji, Michael Galili, ***Minhao Pu***, Liu Liu, Leif K. Oxenløwe, Palle Jeppesen, Torben. Veng, and Lars Grüner-Nielsen, "Silicon waveguide based ultra-fast all-optical waveform sampling," The conference on lasers and electro-optics (CLEO) 2010, CMA2, San Jose, CA, US.

14. Yunhong Ding, Christophe Peucheret, ***Minhao Pu***, Beata Zsigri, Jorge Seoane, Liu Liu, Jing Xu, Haiyan Ou, Xinliang Zhang, and Dexiu Huang, "RZ to NRZ Format Conversion at 50 Gbit/s based on Silicon Microring Resonator," OptoElectronics and Communications Conference (OECC) 2010, pp. 862-863, Sapporo, Japan.

15. ***Minhao Pu***, Liu Liu, Haiyan Ou, Kresten Yvind, and Jørn M. Hvam, "Ultra-Low Loss Nano-Taper Coupler for Silicon-on-Insulator Ridge Waveguide," The European conference on optical communication (ECOC) 2010, Tu.5.C.6, Torino, Italy.

16. Yunhong Ding, Jing Xu, Christophe Peucheret, ***Minhao Pu***, Jorge Seoane, Haiyan Ou, Xinliang Zhang, and Dexiu Huang, "Multi-Channel 40 Gbit/s NRZ-DPSK Demodulation Using a Single Silicon Microring Resonator" The European Conference on Optical Communication (ECOC) 2010, P2.01, Torino, Italy.

17. Hao Hu, Hua Ji, Michael Galili, ***Minhao Pu***, Hans C. H. Mulvad, Leif K. Oxenløwe, Kresten Yvind, Jørn M. Hvam and Palle Jeppesen, "320 Gb/s Phase-Transparent Wavelength Conversion in a Silicon Nanowire," The Conference on Optical Fiber Communication (OFC) 2011, OWG6, Los Angeles, CA, US.

18. Hao Hu, Hua Ji, Michael Galili, ***Minhao Pu***, Hans C. H. Mulvad, Leif K. Oxenløwe, Kresten Yvind, Jørn M. Hvam and Palle Jeppesen, "Silicon Chip based Wavelength Conversion of Ultra-High Repetition Rate Data Signals," The Conference on Optical

Fiber Communication (OFC) 2011, PDPA8 (postdeadline paper), Los Angeles, CA, US.

19. ***Minhao Pu***, Hao Hu, Hua Ji, Michael Galili, Leif K. Oxenløwe, Kresten Yvind, Palle Jeppesen, and Jørn M. Hvam, "Ultra-Broadband Tunable Wavelength Conversion of Sub-Picosecond Pulses in a Silicon Nanowire," The conference on lasers and electro-optics (CLEO) 2011, CMAA1, Baltimore, MD, US.

Contents

List of Figures

Abbreviations

BER	**B**it-**E**rror-**R**ate
CMOS	**C**omplementary **M**etal-**O**xide-**S**emiconductor
CW	**C**ontinuous **W**ave
DMRR	**D**ual-**M**icro-**R**ing **R**esonator
EDFA	**E**rbium **D**oped **F**iber **A**mplifier
ESA	**E**lectrical **S**pectrum **A**nalyzer
FBG	**F**iber **B**ragg **G**rating
FCA	**F**ree **C**arrier **A**bsorption
FCD	**F**ree **C**arrier **D**isperison
FDTD	**F**inite-**D**ifference **T**ime-**D**omain
FSR	**F**ree **S**pectral **R**ange
FWHM	**F**ull **W**idth **H**alf **M**aximum
FWM	**F**our **W**ave **M**ixing
GVD	**G**roup **V**elocity **D**ispersion
ICP	**I**nductively **C**oupled **P**lasma
MRR	**M**icro-**R**ing **R**esonator
MZ	**M**ach **Z**ehnder
MZM	**M**ach **Z**ehnder **M**odulator
OSA	**O**ptical **S**pectrum **A**nalyzer
OSC	**O**ptical **S**ampling **O**scilloscope

OTDM	**O**ptical **T**ime **D**ivision **M**ultiplexing
PBG	**P**hotonic **B**and-**G**ap
PC	**P**olarization **C**ontroller
PD	**P**hoto **D**etector
PhC	**Ph**otonic **C**rystal
PRRM	**P**ulse **R**epetition **R**ate **M**ultiplication
RF	**R**adio **F**requency
RIE	**R**eactive **I**on **E**tching
RPhC	**R**ing-shaped **Ph**otonic **C**rystal
SEM	**S**canning **E**lectron **M**icroscope
SOI	**S**ilicon-**O**n-**I**nsulator
TE	**T**ransverse-**E**lectric
TLS	**T**unable **L**ight **S**ource
TM	**T**ransverse-**M**agnetic
TMLL	**T**unable **M**ode-**L**ocked **L**aser
TO	**T**hermo-**O**ptic
TPA	**T**wo **P**hoton **A**bsorption

Chapter 1

Introduction

1.1 Silicon photonics

As the first semiconductor transistor was demonstrated in 1943 and the later invention of integrated circuit, microelectronics has kept developing in a very fast pace. The size of complementary metal-oxide-semiconductor (CMOS) transistors, as a key factor concerning the computer performance, has been continuously scaled following the Moore's Law, which states that the number of transistors on an integrated circuit will double approximately every two years [1]. Large-scale integration became the leading driver in the semiconductor industry, since it provided enormous reductions of the chip size and system cost, and tremendous improvement in performance and applications. To achieve higher performance, a recent trend towards multiple core processors has shifted the bottlenecks of scaling from the size of the transistor to the size of the microprocessor data bus (i.e. from microprocessor to memory or between multiple processors). However, conventional copper (Cu) electronic interconnects are not suitable for the ultra-high bandwidth on-chip communication in future which makes the optical interconnect a better solution for this application due to its larger bandwidth, lower power consumption, smaller interconnect delays, and better resistance to electromagnetic interference.

Silicon (Si), the second most abundant element on earth, has dominated in microelectronics for many decades. It can also be used for optical interconnects due to its transparency in the range of optical telecom wavelengths which will enable a platform for a monolithic integration of optics and microelectronics. Silicon photonics is the technology associated with signal generation, processing, transmission and detection where the signal is carried by light in silicon-based components. Pioneering work in silicon photonics by Soref and Petermann in the late 1980s and early 1990s stimulated research in this area [2, 3]. The advent and universal adoption of CMOS-compatible silicon-on-insulator (SOI)[1] substrates accelerated the development of research activities in silicon photonics. Leveraging the many-billion-dollar CMOS foundry, very large-scale electronic and photonic integrated circuits can be envisioned.

The major building blocks for silicon photonic circuits include light sources, modulators, waveguides, and detectors. Silicon waveguides with extreme low loss down to 0.8 dB/cm have been demonstrated [4]. Compact silicon modulators based on Mach-Zehnder (MZ) interferometers and microring resonators (MRRs) utilizing the free carrier plasma effect have been demonstrated by Intel [5, 6] and Cornell [7, 8], respectively. Although Si cannot absorb light above about 1.2 μm wavelength, germanium photodiodes can be selectively grown directly on the SOI wafer to make Ge-on-Si detectors [9]. Until now, all the basic Si-based components have been demonstrated with good performance except Si-based light sources. Owing to its indirect bandgap, silicon is normally recognized as a poor light-emitting material. Although optically pumped Si-based Raman lasers have been demonstrated, the power dissipation and efficiency are extremely poor [10]. The current preferred solution is to flip-chip bond a III-V material laser to the SOI chip and couple the light into a silicon waveguide [11, 12]. Integrating lasers using this hybrid silicon laser technology, Intel has announced the first silicon-based 50 Gb/s optical data connection this year which proves that the light

[1] SOI consists of a thin silicon layer on top of an oxide cladding layer carried on a bare silicon wafer. With its silicon core ($n_{Si} = 3.45$) and its oxide cladding ($n_{SiO_2} = 1.45$), it has a high vertical refractive index contrast. In addition, both the silicon and the oxide are transparent at telecom wavelength of 1.3 μm and 1.55 μm.

beams can replace electronic signals for the future computers [13]. However, the integration process for the III-V material on SOI wafers in the hybrid technology is outside the CMOS foundry. To achieve monolithically integrated lasers on Si using CMOS foundry processes, a number of research groups has reported their promising reports based on different ideas including Si quantum dots, erbium-doped Si, doped Ge quantum wells and direct bandgap Ge/Si heterostructures [14]. As all the technologies are approaching a high level of maturity, silicon photonics will first be beneficial to the on-chip interconnect for computing and then impact a wide range of applications, including rack-to-rack, fibre-to-the-home and chemical or medical lab-on-a-chip applications.

1.2 Waveguides

In nano-photonic integrated circuits, ridge waveguides are crucial elements. It is basically a conventional waveguide with a small cross section, typically with a width of 300-500 nm, where the light is guided by total internal reflection. Due to the high index contrast of the SOI material, the light can be tightly confined to the waveguide core. The strong light confinement can enhance the electromagnetic field in sub-micron dimension waveguide core, which induces enhancement of the nonlinear effects in silicon [15, 16]. Since the group velocity dispersion (GVD) of the ridge waveguide, which is a critical parameter for many nonlinear processes such as self-phase modulation [17], cross-phase modulation [18], and four-wave mixing (FWM) [19], can be engineered by modifying the waveguide dimensions, silicon ridge waveguide can be utilized as nonlinear photonic devices. Different optical nonlinear applications including signal regeneration [20], amplification [21], wavelength conversion [22–24], demultiplexing [25], and tunable delays [26], have been demonstrated by using silicon waveguide in the past five years. The potential of employing silicon waveguides for ultra-high-speed (Terabit) data signal processing is investigated in this thesis.

Although the strong light confinement in silicon ridge waveguides allows high-level integration of photonic components, it may also lead to coupling difficulties between the sub-micron silicon waveguide and micron-size fibers due to the large mode mismatch and index mismatch. This problem arise from the high index of refraction of silicon that induces high losses due to refractive index and mode mismatch between the fibers and the silicon waveguides. Grating couplers were proposed to solve the coupling problem [27–29] and a peak coupling efficiency up to 69% has been achieved [29]. However, an additional lithography and etching step is normally necessary to make the shallowly etched grating. Still, the coupling loss is relatively large and the coupling response is wavelength and polarization dependent. To further enhance the coupling efficiency and the bandwidth, an inverted taper coupler featuring a taper from the normal waveguide dimensions to a smaller tip can be utilized [30–32]. An optimization of the inverse taper coupler is presented in this thesis.

1.3 Microring resonators

Silicon MRRs, consisting of a microring and side-coupled waveguides, are important photonic components that offer periodic filtering functions. The high index contrast in SOI waveguides allows small bending radii with low propagation losses leading to ultra-compact resonators and high-density integration of photonic devices. Different research groups have reported very low losses in the microring, e.g., 0.02-0.03 dB/round-trip for a bending radius of 6.5 μm [33], 0.004 dB per 90° bend for a bending radius of 5 μm [34] and 0.01-0.02 dB/round-trip for a bending radius of 5 μm [35]. Therefore, ultra-small MRRs with high quality factors can be realized [36] and utilized in a wide range of applications. In optical communications, the MRR is most often used as a building block in filters [35, 37, 38], electro-optical modulators [39–41], optical switches [42, 43], lasers [12], optical buffers [33] and all-optical signal processing [44, 45]. However, MRRs can also find applications in other fiels such as biophotonics, and microwave photonics.

Microwave photonics is an interdisciplinary field where microwave signals is processed in the optical domain [46, 47] and has been growing dramatically over the past several decades. The microwave system could benefit from the photonic components due to their compact size, large bandwidth, fast tunability, immunity to electromagnetic interference and low weight. Different photonic components including optical fibers [48], semiconductor optical amplifiers [49], and lasers [50] have already been demonstrated in microwave system as radio frequency (RF) phase shifters, which are key components in many microwave applications, such as phased array antennas [51] and microwave filters [52]. In this thesis, a MRR-based RF phase shifter is proposed and the experimental results show the potentials of MRRs in realizing microwave filters.

1.4 Photonic Crystals

Photonic crystals (PhCs) are artificially created materials in which the index of refraction varies periodically between high-index regions and low-index regions [53, 54]. Because of the refractive index difference, light will be scattered very strongly throughout the structure, and the scattered waves from each period can either add up or cancel out, depending on the wavelength of the light. In this way, all light inside the crystal within a certain wavelength range may undergo destructive interference and no propagation thereby experience a photonic band gap (PBG). This unique property has opened up exciting new methods to control light, leading to proposals for many novel devices [55]. A complete PBG can occur only in three-dimensional PhCs. Although these three-dimensional PhCs look very promising and have been theoretically widely studied, the fabrication of such structures is still a challenge [56]. Therefore, the concept of PhC slabs consisting of a thin two-dimensional PhC surrounded by a lower-index material has emerged and has been investigated intensively since it promises easier fabrication using existing techniques.

Defects in PhCs give rise to local optical states and open for e.g. routing of optical signal along line-defects or give resonant states with high

quality factor in point-defects. The line-defect PhC structures including waveguides [57], T-branches [58], sharp bends [59], and channel-drop [60] have already been demonstrated for passive control of light flow. A very interesting phenomenon found in the PhC waveguide is the so-called slow-light phenomenon in which the light can propagate with an extremely low group velocity compared to that in the conventional waveguide due to the large dispersion in PhC waveguides. The dispersion properties can be altered via a structure tuning of the waveguide geometry which will be presented in this thesis. Linear effects including gain, thermo-optic (TO) and electro-optic interaction scale with the slowdown factor which is defined as the ratio of the phase velocity over the group velocity, whereas nonlinear effects may scale with its square [61]. Because of this, PhCs can be utilized in a wide range of applications [62] such as optical buffer, lasers, amplifiers, detectors, absorption modulators, and wavelength converters.

PhC cavities, which can be formed by introducing point defects as already mentioned, are also attracting considerable attentions due to their small size and strong confinement of light. Recently, ultra-small PhC cavities were demonstrated [63, 64]. The quality factor of such PhC cavities has increased greatly [63–65] and has now reached 1.2×10^6 for silicon membrane structures. This makes the device very promising for realization of ultra-small filters with high resolution [66], ultra-small sensors [67], low-threshold lasers [68], single-photon emitters [69], optical-buffer memories [70], optical switching [71, 72], and optical transistors [73]. In this thesis, a PhC cavity with all-optical tunability with the potential in all optical switch is presented.

1.5 Scope and structure of the thesis

The scope of this thesis is to discuss and demonstrate the design, fabrication, and characterization of different nano-photonic components realized in SOI materials and explore the potentials of these devices in different applications. The nano-photonic devices of interest include ridge waveguide, MRRs, and PhC components. The thesis is organized as follows:

Chapter 2 deals with silicon waveguide components. The basic theory for waveguides is introduced. The coupling issue concerning interfacing silicon waveguides and optical fibers is addressed. An optimized inverse taper coupler is presented and characterized. The fabrication process for the silicon waveguide integrated with inverse taper couplers is also included. Thereafter, the characterization of the silicon waveguide in FWM processes is described. In the end, the silicon waveguide-based ultra-high-speed (Terabit) nonlinear signal processing is experimentally demonstrated.

Chapter 3 focuses on different applications for MRRs. Descriptions of transfer characteristics for two basic type structures for MRR are provided before the application parts for each type strcuture. In microwave applications, tunable microwave phase shifters and filters based on all-pass type MRRs are proposed and tested experimentally. In optical communication applications, the experimental results in pulse repetition rate multiplication (PRRM) based on the add/drop type MRR is also presented.

Chapter 4 investigates PhC components. Some fabrication issues for patterning PhC structures are discussed first. Then the basic theory and modelling methods of PhC are given. Then the standard PhC and ring-shaped photonic crystal (RPhC) structures are studied, respectively, including their transmission and dispersion properties, and sensitivities to ambient index. Experimental results for PhC-based components including all-optical tunable cavities, index sensors, slow-light couplers are presented at last.

Chapter 5 sums up this thesis and gives perspectives for future research.

Chapter 2

Ridge waveguide components

Silicon ridge waveguides are an basic and crucial component in nanophotonic integrated circuits. The light is guided in the waveguide through total internal reflection and its confinement is largely determined by the refractive index between the waveguide core and the surrounding cladding. The silicon-on-insulator (SOI) material provide very high refractive index contrast and make it possible to confine the light tightly to a waveguide core with sub-micron dimensions. Typically, silicon ridge waveguides have width smaller than 500 nm to obtain a single-mode operation when operating at telecom wavelength between 1.3 μm and 1.6 μm. The high index contrast for the silicon ridge waveguide allows for very compact elements, such as sharp bends [34], corner mirrors [74], and ring resonator [75]. However, it also make the waveguide more sensitive to scattering loss due to the sidewall roughness. By optimizing the fabrication technology, the propagation loss has reached 2 dB/cm [76]. The propagation loss can be further decreased to 0.8 dB/cm employing a post-fabrication roughness reduction process [4].

Although the high refractive index contrast offers potential for ultra compact devices, interfacing these waveguides to single mode fibers could be problematic. Coupling to and from these devices usually involves

high losses due to the mode-size and effective-index mismatch between the optical fiber and the waveguide structure, which induces coupling to radiation modes and back-reflection. To alleviate this coupling problem, inverse tapers, from the waveguide dimensions to the dimensions of a small tip [32, 77], can be utilized. In this chapter, we optimize the inverse taper structure and obtain an ultra-high efficient coupler.

Due to the sub-micron cross-sectional dimensions, the silicon ridge waveguide can provide an maximal confinement of light for index guiding structures which enables large enhancement of nonlinear interactions and the dispersion engineering [16]. These two properties make the silicon ridge waveguide suited for many optical nonlinear signal processing applications. In the last five years, the silicon-based optical signal processing has gained considerable interest, with pioneering work on optical signal regeneration [20] followed by very recent high-speed advances such as 160 $Gbit/s$ switching [25]. In this chapter, we investigate the potential of using silicon ridge waveguide for ultra-fast (Terabit) signal processing in optical time division multiplexing (OTDM) system.

This chapter begins with the basic principles of the ridge waveguide. Then an ultra-low loss inverse coupler for interfacing silicon ridge waveguide to optical fiber will be introduced followed by its fabrication processes. Some general introduction for the major fabrication facilities are also covered here. Following that, the characterization of silicon waveguide in nonlinear four-wave mixing (FWM) process is presented. Finally, the experimental results for the record-high speed optical demultiplexing and waveform sampling in silicon waveguide are demonstrated.

2.1 Theory of Waveguide

The light propagation in waveguide can be described by macroscopic Maxwell equations [78]:

$$\nabla \cdot \mathbf{B}(\mathbf{r},t) = 0 \tag{2.1}$$

$$\nabla \cdot \mathbf{D}(\mathbf{r},t) = \rho(\mathbf{r},t) \tag{2.2}$$

$$\nabla \times \mathbf{E}(\mathbf{r},t) + \frac{1}{c}\frac{\partial \mathbf{B}(\mathbf{r},t)}{\partial t} = 0 \tag{2.3}$$

$$\nabla \times \mathbf{H}(\mathbf{r},t) - \frac{1}{c}\frac{\partial \mathbf{D}(\mathbf{r},t)}{\partial t} = \frac{4\pi}{c}\mathbf{J}(\mathbf{r},t) \tag{2.4}$$

where $\mathbf{E}$(r,t) and $\mathbf{H}$(r,t) are the electric and magnetic fields, $\mathbf{D}$(r,t) and $\mathbf{B}$(r,t) are the displacement and magnetic induction fields, and ρ(r,t) and $\mathbf{J}$(r,t) are the free charges and currents. Normally, we assume that the material is non-magnetic, isotropic, lossless and the field strengths are so low that the material is operated in the linear regime. Then we can relate the electromagnetic fields by the expressions below:

$$\mathbf{D}(\mathbf{r},t) = \varepsilon\mathbf{E}(\mathbf{r},t) = \varepsilon_r\varepsilon_0\mathbf{E}(\mathbf{r},t) \tag{2.5}$$

$$\mathbf{B}(\mathbf{r},t) = \mu\mathbf{H}(\mathbf{r},t) = \mu_r\mu_0\mathbf{H}(\mathbf{r},t) \tag{2.6}$$

where ε, and μ are the permittivity, and permeability of the material, respectively. For the dielectric material like silicon, the magnetic permeability can be assumed to be unity. In addition, we can set ρ=$\mathbf{J}$=0 since there are no light sources in the silicon material. Based on all the above assumption, we can rewrite the Maxwell equations as below:

$$\nabla \cdot \mathbf{H}(\mathbf{r},t) = 0 \tag{2.7}$$

$$\nabla \cdot \varepsilon\mathbf{E}(\mathbf{r},t) = 0 \tag{2.8}$$

$$\nabla \times \mathbf{E}(\mathbf{r},t) + \frac{1}{c}\frac{\partial \mathbf{H}(\mathbf{r},t)}{\partial t} = 0 \tag{2.9}$$

$$\nabla \times \mathbf{H}(\mathbf{r},t) - \frac{\varepsilon}{c}\frac{\partial \mathbf{E}(\mathbf{r},t)}{\partial t} = 0 \tag{2.10}$$

Taking the curl of the eq. (2.9) and (2.10), we can rewrite the equation as below:

$$\nabla^2\mathbf{E}(\mathbf{r},t) - \varepsilon\frac{\partial^2}{\partial t^2}\mathbf{E}(\mathbf{r},t) = \nabla(\nabla\cdot\mathbf{E}(\mathbf{r},t)) \tag{2.11}$$

This equation can be further reduced with the application of some vector identities to the form:

$$\nabla^2\mathbf{E}(\mathbf{r},t) - \varepsilon\frac{\partial^2}{\partial t^2}\mathbf{E}(\mathbf{r},t) = -2\nabla(\nabla ln(n)\cdot\mathbf{E}(\mathbf{r},t)) \tag{2.12}$$

where n is the refractive index and is defined as $n = \sqrt{\varepsilon_r}$. If we assume the electric field, $\mathbf{E}$, to be harmonically varying in time t at an angular frequency ω which can be written in the form $\mathbf{E}(\mathbf{r},t) = \mathbf{E}(\mathbf{r})e^{i\omega t}$. The eq. (2.12) can then be expressed as the Helmholtz equation:

$$\nabla^2\mathbf{E}(\mathbf{r},t) + \varepsilon\omega^2\mathbf{E}(\mathbf{r},t) = 0 \tag{2.13}$$

Making the substitutions: $\omega = \frac{2\pi c}{\lambda}$ and $\varepsilon = \frac{n^2}{c^2}$, where λ is the vacuum wavelength, and c is the speed of light in vacuum, the following equation is obtained:

$$\nabla^2\mathbf{E}(\mathbf{r},t) + \frac{4\pi^2 n^2}{\lambda^2}\mathbf{E}(\mathbf{r},t) = 0 \tag{2.14}$$

In defining the waveguide structure, we assume that the z-axis is the direction a guided mode propagates along the waveguide and the electric field can be expressed as $\mathbf{E}(\mathbf{r}) = \mathbf{E}(x,y)e^{-i\beta z}$, where β represents the propagation constant. Substituting the Laplacian operator, eq. (2.14) becomes:

$$\frac{\partial^2\mathbf{E}(x,y)}{\partial x^2} + \frac{\partial^2\mathbf{E}(x,y)}{\partial y^2} = (\beta^2 - k_0^2 n^2)\mathbf{E}(x,y) \tag{2.15}$$

where k_0 is the vacuum wae vector, defined as $k_0 = \frac{2\pi}{\lambda}$. Equation (2.15 is an eigenvalue equation, where β^2 is the eigenvalue and $\mathbf{E}(x,y)$ is the eigenfunction. A similar equation can be derived for the magnetic field $\mathbf{H}(x,y)$. By solving the eq. (2.15), we can get two pieces of basic information about how the electromagnetic fields behave in a waveguide. The first is the effective index, defined as $n_{eff} = \frac{\beta}{k_0}$, which is the equivalent of the eigenvalue, for any given mode. The second is a detailed mode profile, consisting of the various vectorial components of the electromagnetic field. Normally, there is no analytical solution for the equations.

Approximations (e.g. the Marcatili approximation [79]) and numerical techniques (e.g. finite difference [80], mode matching method [81], and finite-difference time-domain (FDTD) method [82]) are generally used to find a solution.

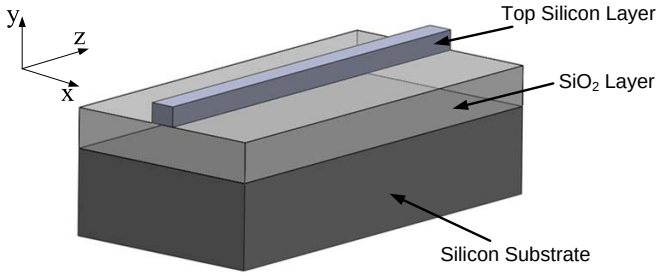

FIGURE 2.1: (a) Schematic drawing of a ridge waveguide in a typical SOI slab configuration.

2.1.1 Single mode condition

The silicon ridge waveguides studied in this thesis are all fabricated in silicon material at the top layer of SOI wafers as shown in fig. 2.1. The SOI wafer have a top silicon layer of 300-nm thickness with the refractive index of 3.45, a 1-μm thick silicon dioxide buffer layer with refractive index of 1.45, and a thick silicon substrate which is always larger than 500 μm.

In the calculation, all the solution can be separatd into two distinct polarizations. One is transverse-electric (TE) modes which have the magnetic field **H** perpendicular to the xz-plane and the electric field **E** in the xz-plane. Another is transverse magnetic (TM) modes which have the electric field **E** perpendicular to xz-plane and magnetic field **H** in the plane. For each polarization, there may exist several different modes. However, the correct operation of many waveguide device types is critically dependant upon the propagation of only a single guided optical mode. Higher order guided modes will introduce cross-talk in Arrayed

Waveguide Gratings (AWGs) [83], unexpected split ratios in Y-junctions and Multi-mode-Interference devices (MMIs) and low extinction ratios in directional coupler type switches. For a waveguide supporting multiple modes, the light will inevitably be scattered from the fundamental waveguide mode at the optical fiber to waveguide interface, at a junction between straight and curved waveguides or in a straight waveguide itself due to the sidewall roughness. Therefore, single mode propagation is highly desirable for the waveguide devices.

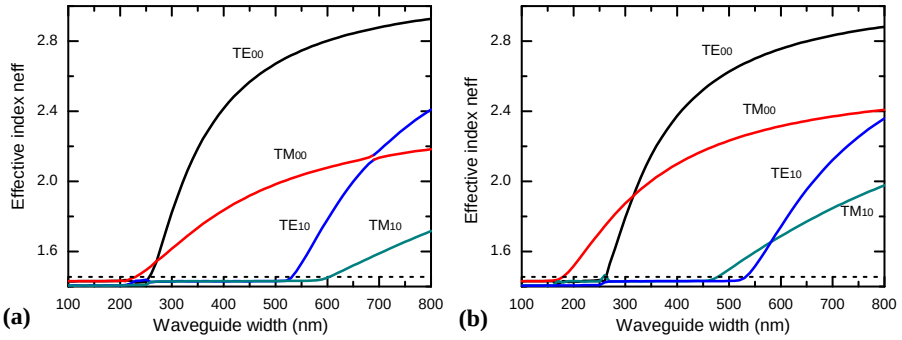

FIGURE 2.2: Calculated effective index of the two lowest order TE and TM modes as a function of the waveguide width for two silicon slab thicknesses: (a) 250 *nm* (b) 300 *nm*.

The cross-sectional dimension of the silicon ridge waveguide determines the number of guided modes. Figure 2.2 shows the calculated effective index for the two lowest TE and TM modes as a function of waveguide width for two different silicon slab thicknesses. Since the structure is asymmetric along the y direction, there exists a cutoff width for each of the modes. If the effective index of a mode is less than the refractive index of silica 1.45, the mode will leak to the silica and can not be guided by the silicon waveguide. The single mode condition then can be easily drawn from fig. 2.2.

For the 250-*nm* thick silicon ridge waveguide, the cutoff waveguide width is about 220 *nm*. The waveguide begin to support only TM_{00} mode as the waveguide width increases to 250 *nm* and then support two fundamental TE and TM modes as the waveguide width increases further to 530 *nm*. To make a truly single-mode waveguide for 250-*nm* thick

silicon slab, the waveguide width should be controlled to be less than 220 nm which makes the waveguide no longer confines the light tightly. The evanescent field of the mode will largely increase and begin to dominate which introduces large additional loss due to the surface scattering. However, the waveguide can confine the light tightly in its core if the waveguide width increases to e.g. 500 nm for 250-nm thick waveguide. Therefore, we refer the single mode waveguide to a waveguide supporting only fundamental TE and TM modes. If the waveguide width is further increased, the waveguide begins to support high order modes such as TE_{10} and TM_{10}.

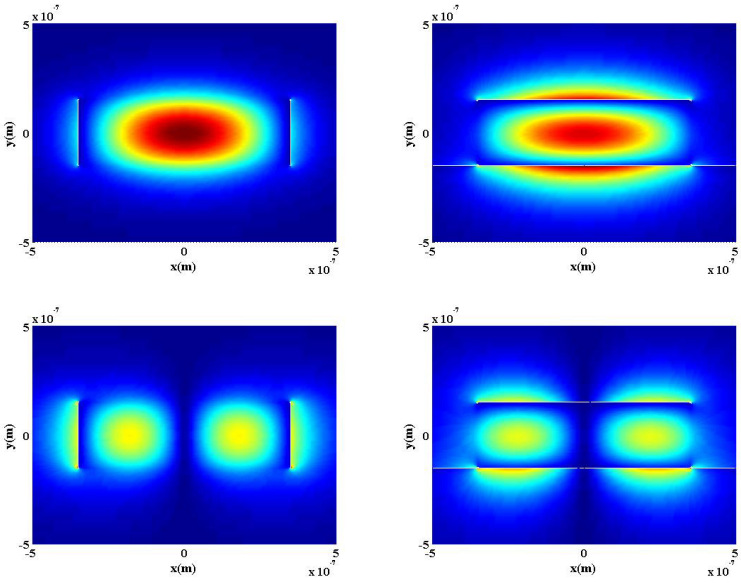

FIGURE 2.3: The calculated field distribution of different modes for the silicon ridge waveguide with a cross-sectional dimension of 300 × 700 nm^2: (Top-left) TE_{00}, (Top-right) TM_{00}, (Bottom-left) TE_{10}, and (Bottom-right) TM_{10}.

For the 300-nm thick silicon ridge waveguide, a waveguide width less than ∼460 nm is necessary to secure the single mode propagation. Any larger waveguide width results in multiple modes with different field patterns. Figure 2.3 shows the calculated field patterns of the two lowest

TE and TM modes for a silicon ridge waveguide with a cross-sectional dimension of 300×700 nm^2.

2.1.2 Dispersion

The effective index does not just vary as a function of waveguide dimension, it also varies with the wavelength. Figure 2.4(a) shows the calculated effective index as a function of wavelength. As wavelength increases, the effective refractive index N_{eff} decreases since the field penetrates more to the cladding lower refractive index material. Therefore, the light at different wavelength will propagate along the waveguide with different group velocity due to the wavelength dependent index variation. The group velocity of a guided mode, v_g, is given by [80]:

$$v_g = \frac{c}{n - \lambda \frac{\partial n_{eff}}{\partial \lambda}} = \frac{c}{n_g} \tag{2.16}$$

where n_g is the effective group index associated with a mode. Fig. 2.4(b) shows the calculated group effective index for the silicon ridge waveguide with a cross-sectional dimension of 300 × 450 nm^2. The effective group index also varies significantly as wavelength changes which inevitably result in the dispersion problem. The group velocity dispersion (GVD) offers a description of how the differential delay, $\triangle t$, over certain length of waveguide, L, relates to the bandwidth, $\triangle \lambda$, and can be expressed as below:

$$GVD = \frac{\triangle t}{L \triangle \lambda} = -\frac{\lambda}{c} \frac{\partial^2 n_{eff}}{\partial \lambda^2} \tag{2.17}$$

The GVD is determined by both the intrinsic material dispersion and by a contribution from the light confinement in the waveguide. For a typical low-index contrast waveguide with core sizes on the order of a few microns, the GVD is dominated by the material dispersion but with a small correction due to the waveguide contribution [84, 85]. However, for a large index contrast waveguide like the silicon ridge waveguide, the waveguide dispersion becomes dominant to the degree that the material dispersion is a small correction to the waveguide dispersion. In this case, the GVD can be highly engineered by tailoring the waveguide dimension.

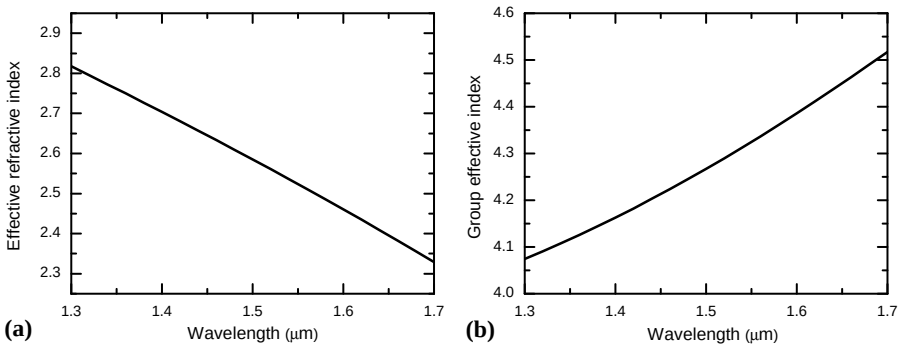

FIGURE 2.4: Calculated effective index (a) and group effective index (b) as a function of wavelength for a silicon ridge waveguide with cross section of $300 \times 450\ nm^2$.

Figure 2.5(a) shows the pure waveguide GVD for the silicon ridge waveguides with different dimensions. The waveguide dispersion seems highly controllable when the waveguide dimension is tailored. And the waveguide can be made with anomalous-GVD or normal-GVD in a specific wavelength range. Figure 2.5(b) shows the overall-GVD of the silicon ridge waveguide when the material-GVD is included. Comparison of the overall-GVD and waveguide-GVD illustrates the dominance of the waveguide dispersion over the material dispersion for the silicon ridge waveguide. A wide variety of the overall-GVD values can be accessible at the specific wavelengths of interest. For many nonlinear optical processes, the group-velocity dispersion is of critical importance [86]. The GVD controls the broadening of ultrafast pulses, the walkoff between pump and probe pulses, the phase-matching of parametric processes, and the generation of temporal optical solitons. Therefore, the dispersion engineered silicon waveguide is highly desirable in the relevant nonlinear applications. In section 2.4, the ultra-fast signal processing including optical waveform sampling and demultiplexing for OTDM based on the single straight silicon ridge waveguide will be discussed.

Before implementing the silicon waveguide devices into any optical system, we will face the coupling problem between the sub-micron waveguide and optical fibers. Due to the high refractive index of silicon, the

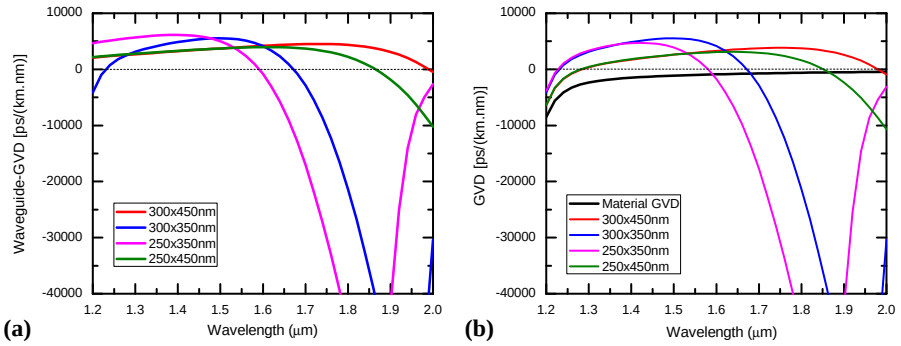

FIGURE 2.5: Waveguide contribution to the GVD (a) and overall GVD (b) including the material dispersion.

single mode silicon ridge waveguide normally have a much smaller optical field dimensions compared with that of optical fibers which results in large mode mismatch thereby leads to an inefficient coupling. In addition, the large refractive index difference between these two materials also contributes to the inefficient coupling. Proper couplers are necessary to integrated with the waveguides to solve this problem and will be discussed in the following section.

2.2 Interfacing SOI ridge waveguide and fiber

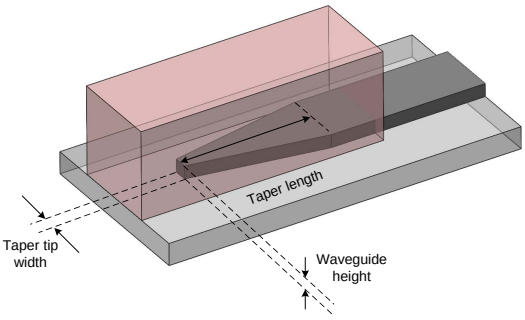

FIGURE 2.6: Schematic drawing of the inverse taper coupler.

As mentioned before, the coupling could be a problem that need to be solved first for the ridge waveguide. The direct coupling between the SOI ridge waveguide and a single mode fiber will result in up to 20 dB coupling loss which is not acceptable for practical applications. The most simple way to improve the coupling for the ridge waveguide is by using tapers from sub-micron waveguide dimension to few microns at the end of the device. The coupling loss can be reduced significantly but still larger than 5 dB per coupling since the tapering is only in one dimension and the mode at the end of the taper is still very different from that for the fiber. The most efficient structure is the inverse taper structure together with a cladding waveguide. Figure 2.6 shows the schematic diagram of the inverse taper structure that achieves low loss coupling. In this coupler, the width of the silicon ridge waveguide is tapered from its origin width down to a tiny tip end in order to expand the guided mode. The silicon ridge waveguide and the taper are embedded in a cladding waveguide with a cross-sectional dimension matched to the access fibers. In this way, as the light propagating along the inverse taper structure, the silicon ridge waveguide mode becomes the cladding waveguide mode which is designed to match the fiber mode.

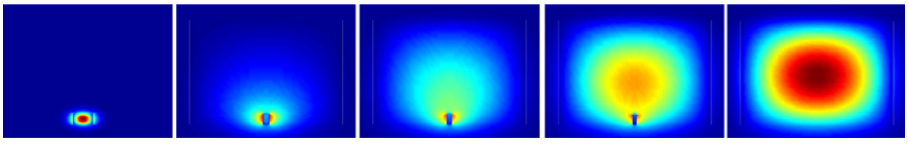

FIGURE 2.7: The calculated mode field distributions with different silicon taper width for the inverse taper coupler. ((a) 450 nm, (b) 150 nm, (c) 100 nm, (d) 50 nm, (e) 0 nm)

Figure 2.7 shows how the light field distribution changes in the taper. Initially the light is confined within the silicon ridge waveguide core, but at the width of around 150 nm, the light starts to escape from the silicon core. As the width of the silicon taper further decreased, the light finally becomes a mode of the cladding waveguide which is much larger than the original mode in the silicon ridge waveguide. Since the cladding waveguide is made to have a similar refractive index and mode size as optical fibers, the coupling between the cladding waveguide and a single mode fiber could be very efficient.

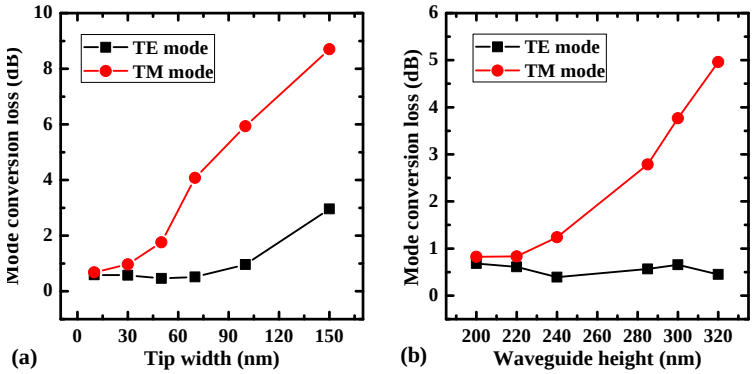

FIGURE 2.8: Calculated mode conversion loss for nano-taper couplers with different tip widths (waveguide height=340 nm) (a) and different waveguide heights (tip width=80 nm) (b). Here, the taper length is always assumed to be 300 μm.

2.2.1 Optimization of the inverse taper coupler

The performance of the inverse taper coupler is highly dependent on its geometrical dimensions: the taper length L, the taper tip width W, and the waveguide height H. Figure 2.8(a) shows the calculated coupling loss as a function of the taper tip width for a 340×450 nm^2 ridge waveguide. It is clear that the coupler has different performance for the different modes. For the TE mode, the coupling loss is reduced to less than 1 dB when the tip end width is decreased to 100 nm. However, the coupling loss for the TM mode is still very large at this point. Due to the different field distributions of the TE and TM modes as mentioned in section. The TE mode, which has its electric field in the silicon slab plane, can see the inverse tapering much more than the TM mode since the inverse tapering is only in one dimension (the xz-plane). Therefore, the TE mode can be expanded easily to achieve efficient coupling without an ultra-narrow taper tip. In [32], a 200-μm long taper with a 60-nm wide tip is fabricated to obtain a coupling loss of 1 dB for a 300×300 nm^2 ridge waveguide, and in [77], a 150-μm long taper with 75-nm wide tip end was utilized to achieve the same level of loss for a 220×450 nm^2 ridge waveguide. However, the coupling loss of these couplers for TM mode is relatively large (∼2 dB). In order to obtain a coupling loss less

than 1 dB for the TM mode, the tip end width is necessary to reduced to a extreme narrow width smaller than 20 nm.

The coupling loss for the inverse taper structure with different waveguide height is also calculated as shown in fig. 2.8(b). Here, we fixed the taper tip width at 80 nm. The coupling loss for the TM mode is reduced significantly as the height decreases, while the coupling loss for the TE mode remains almost the same.

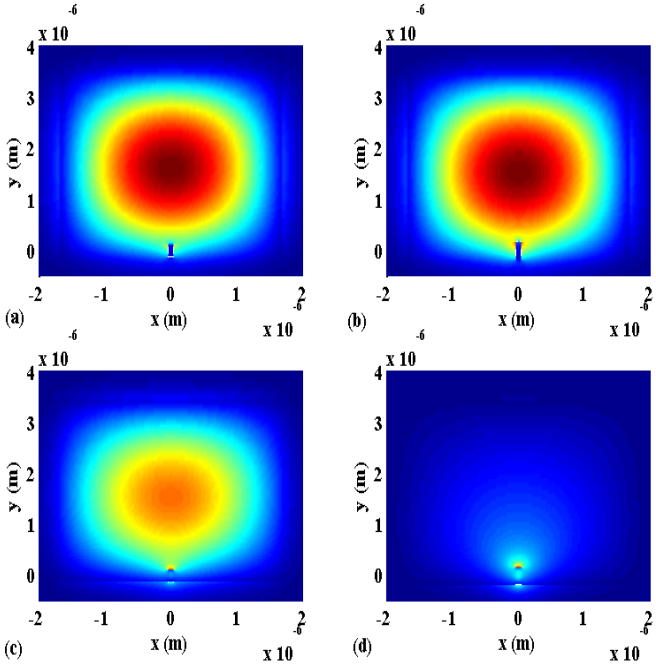

FIGURE 2.9: Mode field distributions at the tip ends of the nano-taper couplers with different waveguide heights for different polarizations: (a) 240 nm, TE mode. (b) 320 nm, TE mode. (c) 240 nm, TM mode. (d) 320 nm, TM mode. The tip end width and the taper length are assumed to be 80 nm and 300 μm, respectively.

Figure 2.9 shows the mode distributions at the tip ends of the taper with different waveguide heights (320 nm and 240 nm) for both TE and TM modes. As shown in figs. 2.9(a) and 2.9(b), for TE polarization, the mode can be fully expanded for both heights. However, for TM

polarization, the mode field is still well confined within the silicon core region when the height of the waveguide is 320 nm, which will lead to a large mode mismatch loss. Thus, in order to make a low-loss coupling for both TE and TM modes, It is desirable to use a SOI wafer with a top silicon layer thickness less than about 250 nm.

2.2.2 Sample preparation and characterization setup

We first fabricated the inverse taper couplers in the SOI wafer with a top silicon thickness of 340 nm and a 1-μm buried silicon dioxide. A detailed fabrication processes will be presented in the following section. The inverse taper structures were made utilizing the standard fabrication process without any thermal treatment. A series of couplers were fabricated with different tip widths and different taper lengths. Figure 2.10(a) shows the silicon taper tip with the smallest reproducible width of 30 nm. It is difficult to make the tip end smaller than that due to the high aspect ratio of the tip end structure. The narrow taper tip is very fragile and easy to fall down during the fabrication process. Figure 2.10(b) shows a "fallen down" taper with the tip width of 25 nm.

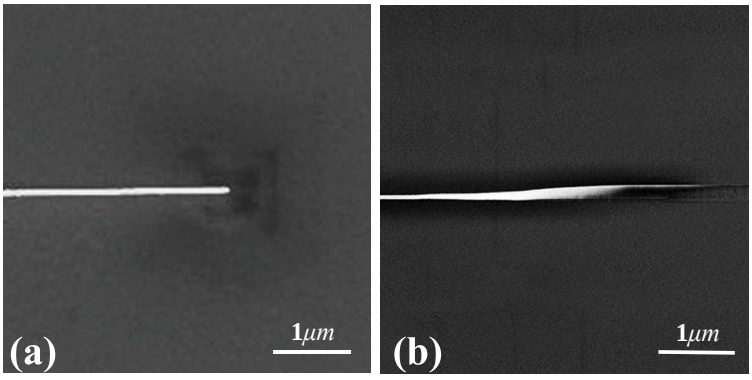

FIGURE 2.10: The SEM picture of the fabricated inverse taper with different tip widths (a) 30 nm and (b) 25 nm.

We also fabricated the inverse taper couplers in SOI wafer with a 250-nm thick silicon layer. Since an extreme narrow taper tip is necessary

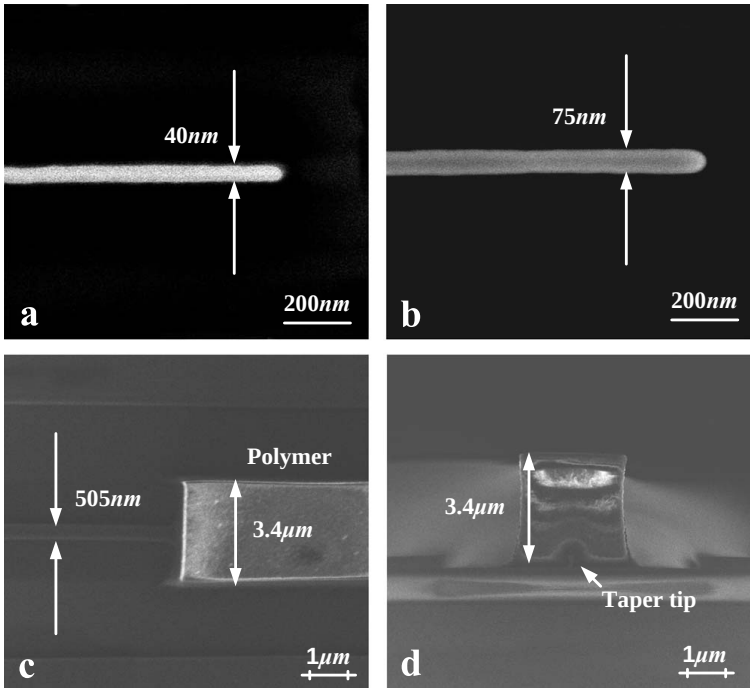

FIGURE 2.11: The SEM pictures of the sample: (a) Silicon nano-taper tip end before oxidation process. (b) Silicon nano-taper tip end after oxidation process. (c) Junction point of polymer core and silicon waveguide. (d) Cross-section view of the nano-taper coupler.

to make high efficient coupling for TM mode, we can utilize the thermal oxidation process to further decrease the taper tip width. In this method, a taper with a relatively wide tip can be first fabricated and then the tip width is further reduced by the thermal oxidation process at $900°C$ for 270 minutes. Figures 2.11(a) and 2.11(b) shows the scanning electron microscope (SEM) pictures for a 40-nm wide taper tip before and after oxidation. During the thermal oxidation process, a thin oxide cladding layer is formed surrounding the whole silicon structure including the waveguide and the tapers. The width of the taper tip with the thin oxide layer is 75 nm. Due to the consumption of the silicon material in the oxidation process, the taper tip becomes narrower. Since the amount of silicon consumed during the oxidation process is $\sim$46%

of the total thickness of the oxide layer according to the relative densities and molecular weights of silicon and silicon dioxide. The estimated width for the taper tip end is about 12 nm which could be very helpful to enhance the coupling efficiency. In addition, the thin oxide layer can be also served as a protection layer for the narrow tip end during the fabrication process which makes the taper structure robust. Figure 2.11(c) and 2.11(d) show the SEM pictures for the conjunction part and the side view of the cross section for the fabricated polymer waveguide. The dimension 3.4×3.4 μm^2 of the polymer waveguide dimension is optimized to minimize the mode mismatch between the fiber we used and the polymer waveguide.

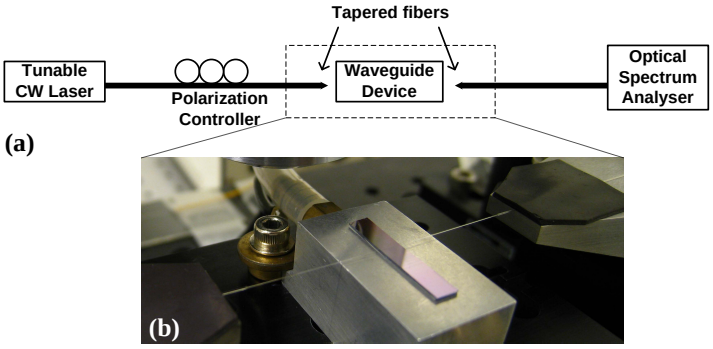

FIGURE 2.12: (a)Transmission characterization setup. (b) Cleaved SOI chip on stage and two tapered fibers for coupling.

The characterization setup used for measuring the transmission characteristics of the fabricated nano-photonic components is shown in fig. 2.12. Tunable laser is used as the light source with the wavelength tuning range within 1480∼1620 nm. A polarization controller (PC) is used to select the proper polarization. To increase the fiber-to-waveguide coupling efficiency, tapered lensed fibers with spot diameter of 2.9 μm are mounted on two micro-stages. The device under test is mounted on a vacuum holder on a temperature controller to avoid any thermal sensitivity. Before mounting the device, the fabricated samples are cleaved to 3×20 mm^2 to fit the vacuum holder. And the taper coupler or inverse taper couplers are designed at both ends of the cleaved chip for the fiber coupling. The fiber alignment are performed under the microscope with

50× magnification through adjusting the micro-stages by piozo-resistive elements. The transmission spectra are recorded by an optical spectrum analyzer (OSA) with a typical resolution of 0.1 nm.

2.2.3 Characterization

The inverse taper couplers fabricated on the SOI wafer with 340-nm thick silicon layer were first measured. The measured fiber-to-fiber loss for a 5-mm long SOI ridge waveguide integrated with two inver-taper couplers is 4.7 dB. The taper length and the tip width for the taper coupler are 300 μm and 30 nm, respectively. The insertion loss includes the propagation loss in the silicon waveguide and the insertion loss of the inverse-taper coupler. The tapered fibers have a non-negligible insertion loss themselves. This was quantified using continuous wave (CW) light and measuring the photocurrent from a large-area photodiode at the exit of the tapered fiber and, using the same photodiode, at the input connector. From the ratio of the two currents, we calculate that the insertion losses of the two tapered fibers used in the measurement are 0.49 dB and 0.61 dB, respectively. The total insertion loss of the 5-mm long SOI ridge waveuigde and two inverted taper couplers is then calculated to be ∼3.6 dB for TM mode. This loss includes the propagation loss in the silicon waveguides and the coupling loss of the inverted taper couplers.

The cut-back method was used to evaluate the propagation loss of the SOI ridge waveguide. Figure 2.13 shows the transmission spectra measured for the waveguide with different lengths from 5 mm to 30 mm for TM polarization. Each spectrum is normalized to the transmission through a 5-mm waveguide. Figure 2.13(b) shows the linear fit to the transmissions for TM modes at the wavelength of 1550 nm, which gives the propagation loss of 4.69 dB/cm for TM modes. Therefore, the insertion losses of each inverted taper coupler can be calculated by subtracting the propagation loss.

Figure 2.14 shows the extracted coupling loss of the inverse taper coupler with different tip width and taper lengths. As we expected, the coupling loss for the TE mode is very small even when the tip width is as large

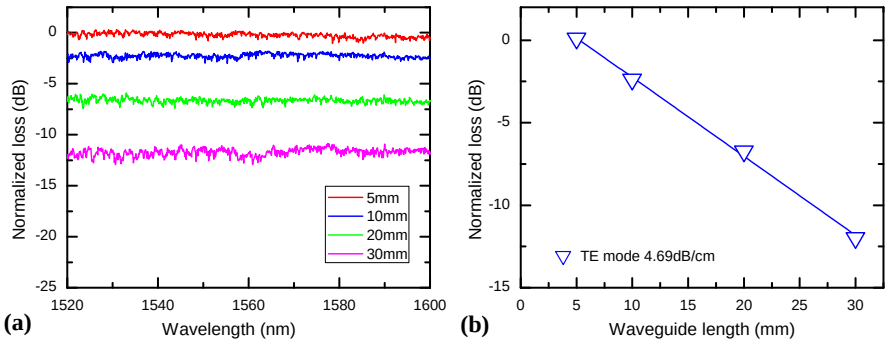

FIGURE 2.13: (a) Measured transmission spectra for the TE mode for waveguides with different lengths from 5 mm to 30 mm. (b) The transmission as a function of waveguide length at the wavelength of 1550 nm.

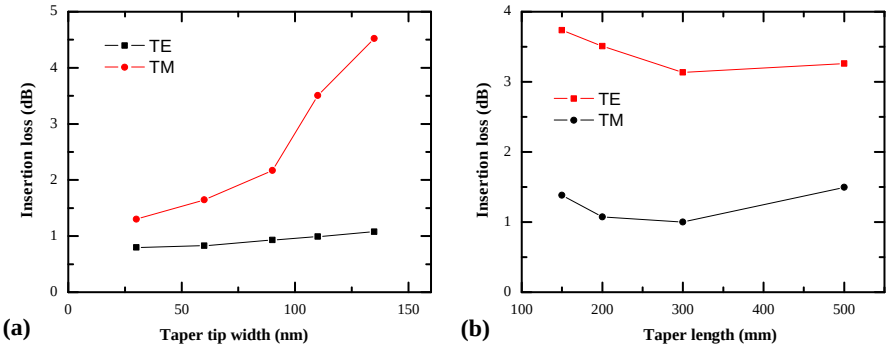

FIGURE 2.14: Measured insertion loss for couplers with different taper tip width (a)(for 300-μm taper length) and taper length (b)(for 100-nm taper tip width).

as 120 nm while the coupling loss for the TM mode is much large. And the inverse taper coupler with the narrowest tip width (30 nm) gives the best performance. Besides, the coupling loss is also dependent on the taper length. In principle, the conversion loss would become smaller as the taper become longer. However, the coupling loss increased when the taper length becomes larger than 300 μm which is not as the simulation predicted. It is probably because the propagation loss in the tapered part

will increase as the taper length increases due to the large mode intensity at the interface between inverse taper and the polymer waveguide.

The inverse taper couplers fabricated on the SOI wafer with 250-nm thick silicon layer are also tested. The thermal oxidation process is applied for these couplers to achieve ultra-narrow tip width (12 nm). Figure 2.15 shows the transmission spectrum of a 3-mm long SOI ridge waveguide integrated with two inverted taper couplers. Figure 2.15(b) shows the additional loss with misalignment in vertical and horizontal directions for the TM mode. The misalignment tolerance of the inverted taper coupler is relatively large, with 3 dB of additional loss for ± 1.5 μm misalignment in both vertical and horizontal directions. This is a result of the 3.4×3.4 μm^2 cross-section dimension of the polymer waveguide. The measured fiber-to-fiber loss for the waveguide is $\sim$3.13 dB for the TM mode and $\sim$3.69 dB for the TE mode. The observed variations of the coupling efficiency are about 0.4 dB and 0.3 dB for the TE and TM mode, respectively.

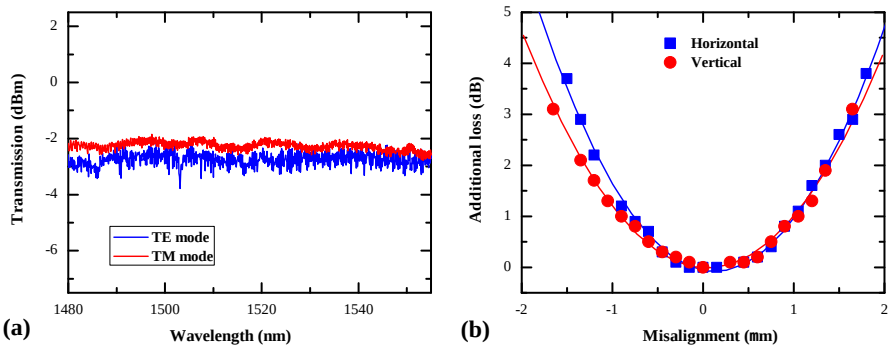

FIGURE 2.15: (a) Measured transmission spectra for a 3-mm long SOI ridge waveguide for both TE and TM modes. (b) the measured additional insertion loss of nano-taper coupler due to the fiber-to-coupler misalignment for the TM mode.

The propagation loss for the waveguide were measured at first. Figure 2.16(a) shows the measured transmission spectra for the waveguide with different lengths for TM mode. From figure 2.16(b), we find that the propagation loss for the waveguide are 4.24 ± 0.008 dB/cm and 4.37 ± 0.014 dB/cm for TE and TM modes, respectively, which are about

0.5 dB smaller compared with the previous waveguide. Due to the thermal oxidation process, the sidewall roughness became smaller as the silicon material consumes which make the waveguide much more smooth thereby reduce the surface scattering [4]. The propagation loss could be further reduced by much longer thermal oxidation process. However, the large consumption of silicon material in the long thermal oxidation process changes the waveguide geometry significantly and special designed SOI wafer is needed for this purpose. As the SOI ridge waveguide is 3-mm long, the propagation losses will contribute 1.31 dB and 1.27 dB to the total insertion losses for TM and TE modes, respectively. Therefore, the insertion losses of each nano-taper coupler are concluded to be 0.36 dB and 0.66 dB for TM and TE mode, respectively.

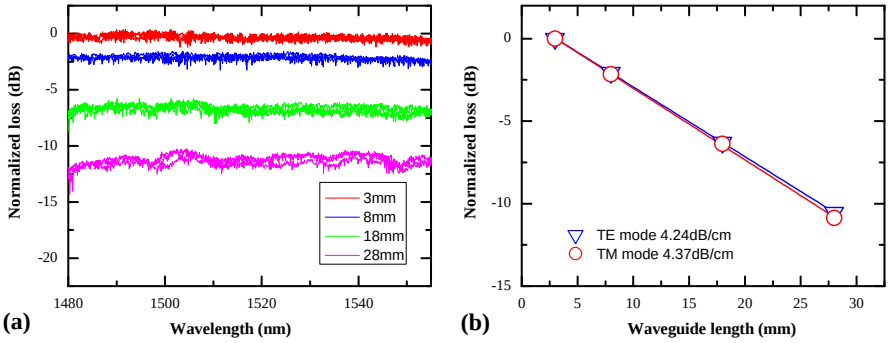

FIGURE 2.16: (a) Measured transmission spectra for the TM mode for waveguides with different lengths from 3 mm to 28 mm. (b) The inset shows the transmission as a function of waveguide length for both TE and TM modes at the wavelength of 1500 nm.

As mentioned previously, the coupling loss for the inverted taper coupler mainly consists of mode conversion loss and scattering loss resulting from the roughness of the interface around the tapered silicon core. In principle, the mode conversion loss for both TE and TM mode can be reduced to a low level if the tip width can be made narrow enough. However, since the silicon dioxide layer formed by thermal oxidation process is not removed, the roughness at both interfaces between the silicon waveguide and silicon dioxide layer and between the silicon dioxide layer and the polymer waveguide makes the scattering loss in the taper different for TE and TM mode. The mode field for TE polarization is

more sensitive to the sidewall roughness than the TM polarization due to their different mode field distributions during the mode conversion along the taper. This will probably lead to a larger scattering loss in the silicon taper for TE mode and therefore a slightly larger coupling loss for the inverted taper coupler.

Compared with the former coupler without thermal oxidation, it is found that the coupling loss for the TM mode has been largely reduced while the coupling loss for the TE mode do not change that much. Therefore, it seems not necessary to utilize the thermal oxidation process for the inverse taper coupler since most of the waveguide device works at the TE polarization. However, it is recently found that many waveguide devices would perform better under TM polarization and some of them even work only for TM mode. For instance, an integrated tunable device with liquid-crystal cladding offers larger tunability for TM mode [87]; a SOI waveguide provides larger bandwidth for TM polarized light in wavelength-conversion applications [23], and a refractive index sensor based on photonic crystal (PhC) pillars only works in TM mode [88]. Thus, it is very useful to utilize the thermal oxidation process to achieve ultra-low coupling loss for the TM mode.

2.3 Fabrication

Fabrication of the waveguide with feature size down to a few tens of nanometers need very high resolution lithography and highly anisotropic etching processes. The major processes includes the electron-beam lithography and reactive-ion-etching. In this section, fabrication process of the SOI ridge waveguide integrated with the inverse taper couplers will be presented at first. And then the basic introduction for e-beam lithography and inductively coupled plasma reactive ion etching (ICP-RIE) will be described.

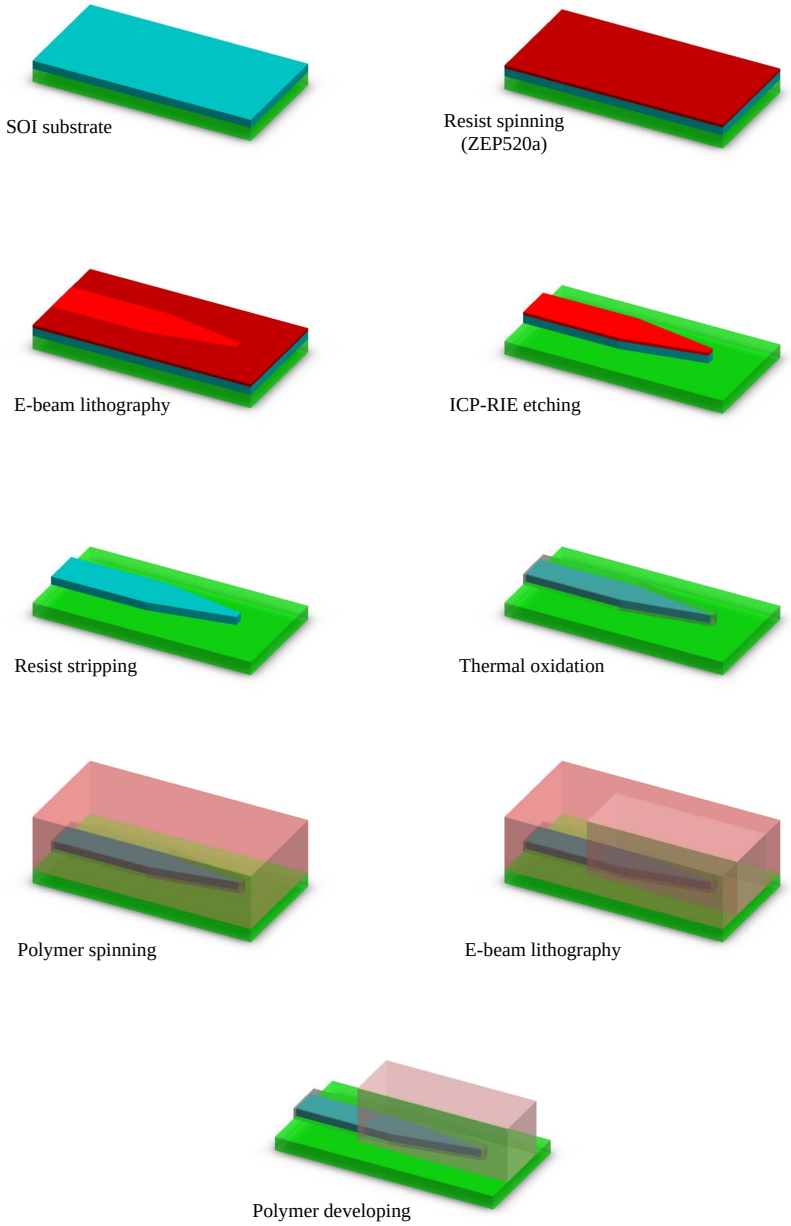

FIGURE 2.17: Schematic overview of the fabrication process for ridge waveguide with inverse taper coupler.

2.3.1 Process overview

The main steps in the fabrication of the SOI waveguide integrated with inverse-taper couplers is shown in fig. 2.17. Electron-beam resist ZEP520A was spin-coated on the SOI wafer to create a 110-nm thick masking layer. To make the masking layer as thin as 100 nm, the 11% ZEP520A resist is diluted 1:1 with anisole before spinning. Then the SOI wafer is spinning at 6000 rpm for 60 seconds. After that, a 2-minute baking at 160°C is necessary. The waveguide and taper structure was defined in the ZEP520A layer by utilizing electron-beam lithography. All the patterns will be formed in the resist layer by developing the sample in the developer ZED-N50 for 1 minute. Then, the sample need to have a post-bake process at 110°C for 5 minutes to harden the resist for the etching process. The patterns were subsequently transferred to the top silicon layer by employing ICP-RIE. Then, a dry thermal oxidation was applied at 900°C for 270 minutes. After the oxidation process, a very thin silicon dioxide layer was formed around the silicon which results in some consumption of the silicon material for the waveguide and taper. A top cladding of 3.4-μm polymer (SU8-2005) was then spin-coated on the chip with 6000 rpm speed and 3000 $rpmm$ acceleration within total 45 seconds. Before the spinning the SU8 resist, a long time prebake of the SOI wafer at 250°C is very important to enhance the adhesion between the polymer and SOI wafer. The polymer waveguide structures were also defined by electron-beam lithography and directly formed by developing in DEV-SU8 following a post-bake at 90°C for 3 minutes. No extra etching process is needed since the SU8 is a negative resist.

2.3.2 Electron beam lithography

The electron beam lithography is a method to define pattern by scanning a beam of electrons across the desired material surface covered by a resist layer. After that, the region exposed (un-exposed) to the electron beam can be selectively removed for positive (negative) resist. In this way, the subsequent etching process can be performed to transfer the resist pattern to the substrate material.

In the DANCHIP cleanroom is JEOL JBX-9300FS electron beam lithography system. In this system, a thermal field emission type cathode and ZrO/W for the emitter is used to generate an electron beam. The beam generated from the emitter is accelerated by a high voltage and processed through a four-stage e-beam focusing lens system and forms a spot beam on the workpiece. The focused electron beam can be controlled by a deflection system to scan point by point according the the wanted pattern shapes in a limited writing field with typical size of $500 \times 500\ \mu m^2$. For defining a pattern larger than one writing field, the equipment divides the pattern into multiple writing fields and move the workstage one by one. This movement control need high accurate alignment and always lead to unavoidable stitching errors (less than 30 nm for the JBX-9300FS). In this case, one need to avoid placing the critical structure at the writing field edges. Compared to the conventional optical lithography, this point by point scanning is much time-consuming and it normally takes tens of minutes to several hours to write a functional device. However, the ultra-small electron beam width down to less than 10nm make it possible for patterning in nanometers instead of the hundreds nanometers for the optical methods.

For different resist in the e-beam lithography, different parameters like dose, current, and step size need to be chosen. Clearance doses need to be used to completely remove the exposed resist like ZEP520A and the unexposed resist like SU8. The dose Q can be expressed as:

$$Q = \frac{t \times I}{A} \tag{2.18}$$

where t is the dwell time of the electron beam, I the current, and A the pattern writing area. The current could be chosen according to the smallest feature size of the structure since the beam diameter increases with larger current. For instant, a current of 2 nA in the JEOL JBX-9300FS system is corresponding to a beam width of 8 nm. The step size related to the pattern writing area should be chosen slightly smaller than the beam size to obtain a good exposure uniformity. For the JEOL JBX-9300FS system, the operation speed for the deflection system is 25 MHz which corresponds to a minimum 40 ns dwell time. Therefore,

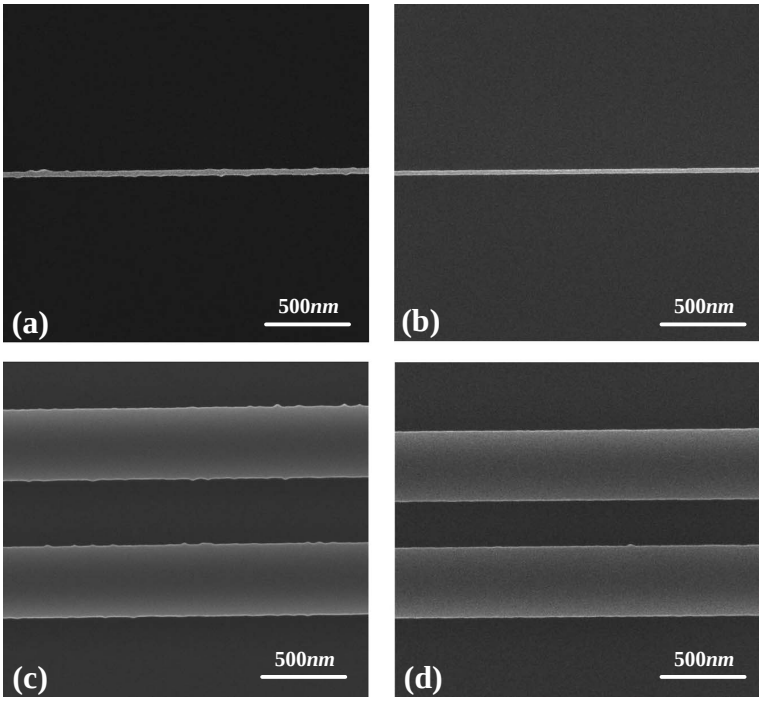

FIGURE 2.18: The SEM pictures of the fabricated 50-nm wide nanowires (a,b) and the 450-nm wide waveguides (c,d) with different e-beam exposure dose: (a,c) 200 $\mu C/cm^2$ (b,d) 250 $\mu C/cm^2$.

all the parameters need to be chosen according the feature size of the structure and also the acceptable dwell time.

For patterning the waveguide and tapering, different test structures are fabricated with different combination of these parameters. Figure 2.18 shows the fabricated waveguide and also the nanowires with different doses. It is clear, for the dose of 200 $\mu C/cm^2$, the sidewall is very rough which will results in high propagation loss for the waveguide as mentioned in section. However, as the dose increases to 250 $\mu C/cm^2$, the waveguide can be pattern with much smooth sidewall as shown in figs. 2.18(b) and 2.18(d). Also similar test structures are fabricated for the SU8 polymer waveguide. The optimized parameters are dose 4 $\mu C/cm^2$, current 0.21 nA, and step size 12 nm.

2.3.3 Reactive-ion-etching

Reactive-ion-etching (RIE) technology as an anisotropic etching, has been widely used for etching semiconductors, dielectrics, and metals. In RIE, chemically reactive plasma is used to remove material deposited on wafers. The plasma is typically generated by a radio frequency (RF) electric field. For silicon etching, SF_6 gas is used. SF_6 dissociates into atomic fluorine and heavy SF_5^+ ions in plasma during the process:

$$SF_6 + e^- \rightarrow SF_5^+ + F + 2e^- \tag{2.19}$$

Silicon is then subsequently etched by the fluorine according to the reaction:

$$Si(s) + 4F(g) \rightarrow SiF_4(g) \tag{2.20}$$

Due to an inherent electrial potential difference between the plasma and the substrate, the ions formed in the plasma will bombard the surface of the substrate which helps clear the surface of reaction products, thereby enhancing the etch rate. The anisotropy can be increased by adding carbon-fluorides or oxygen, which forms protective films on the substrate surfaces. The directional ion bombardment is more important in removing these films. However, the protective films on the vertical surface are removed much slowly compared with that on the horizontal surface which results in the an increased vertical/horizontal etch rate ratio. A RIE is typical capacitively coupled system where the plasma density and energy of ion bombarding the substrate are correlated. While the plasma density and the ion bombardment energy can be adjusted by using ICP system. The inductive coupling method produces a highly dense plasma which gives a 5∼10 times higher etch rate than in traditional capacitively coupled RIE systems while the chamber pressure is kept low to ensure the directionality of the ion bombardment. In the DANCHIP cleanroom, the STS Advanced Silicon Etch (ASE) utilizs an ICP for RIE process.

The sidewall angle can be well controlled using the Bosch process, where the etch and passivation chemistries can be separated in time by switching the process continuously between an etching and passivating chemistry in cycles of 2∼15 seconds. The gases used for silicon etching is

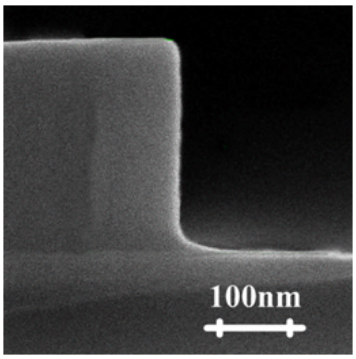

FIGURE 2.19: The SEM cross-sectional view picture of a silicon waveguide after the ICP-RIE process.

mainly SF_6 and C_4F_8 in the etch phase, and C_4F_8 in the passivation phase. During the passivation phase, CF_2 is formed from C_4F_8 which then adsorbs on the surfaces and forms a teflon-like polymer. During the etch phase, the CF_2 molecules are removed by combination of physical ion sputtering and chemical reactions. Due to the directional ion bombardment of the substrate, the removal rate of the deposited polymer layer is largest on the horizontal surfaces, and the sidewalls thus remain protected during the etch phase, if the ratio between the etch time and deposition time is well adjusted. In this way, a very vertical sidewall of the etching could be expected. A standard recipe for the silicon etching includes an etching cycle of 5 seconds and a 3-second passivating cycle. The chamber pressure is kept low at 10 $mTorr$ during the whole etching process. The silicon etch rate for this recipe is about 450 nm/min and typically, 9 cycles are needed to etch through a 340-nm thick silicon layer of the SOI wafer. Figure 2.19 shows the SEM cross-sectional view picture of a waveguide after the etching process.

2.4 Nonlinear optical signal processing

Due to the high index contrast of the SOI material, the silicon waveguide can be made in sub-micron dimension. The sub-micron waveguide is not only beneficial to high degree photonic integrated circuit, the

ultra-small silicon core waveguide also offers an enhanced nonlinearity. Since nonlinear optical processes are the basic mechanisms for many applications including all-optical modulators, switches, pulse delays, regenerators, amplifers, pulse compressors and wavelength converters, the optical nonlinearity of silicon waveguide has gained increasing research interest [16]. Among all the nonlinear optical processes, the FWM is one of important parametric processes which has broad applications in fast signal processing. Several research groups have already demonstrated the fast all-optical signal processing using the silicon waveguide such as 1 μs tunable delay, 10 $Gbit/s$ signal regeneration, 40 $Gbit/s$ wavelength conversion, 160 $Gbit/s$ demultiplexing based on FWM. In the sub-micron silicon ridge waveguide, the GVD, which is a critical parameter to determine FWM efficiency, is highly engineerable since the waveguide dispersion dominate over the material dispersion and can be tailored by changing the waveguide dimensions as mentioned in section. In this section, the characterization of silicon ridge waveguide is described first. And then, ultra-fast all-optical signal processing including the optical demultiplexing and optical waveform sampling based on the silicon ridge waveguide in an OTDM system (640 $Gbit/s$ and 1.2 $Tbit/s$) will be discussed.

2.4.1 Characterization of silicon waveguide in four-wave mixing

FWM is a phenomenon that photons from one or more waves are annihilated and new photons are created at different frequencies. If a signal wave together with a pump wave are launched into a silicon waveguide, FWM will transfer energy from the strong pump wave to a new wave upshifted or downshifted in frequency from the pump frequency. A typical FWM spectrum is shown in fig. 2.20. Two tunable laser sources (TLSs) are used to form the pump and signal waves at the wavelength 1550 nm and 1552 nm, respectively. The two waves are coupled into a silicon waveguide using tapered fibers and inverse taper couplers as mentioned before. PC before the tapered fiber is used to allow for selections of TE or TM polarization. Two clear idler waves are generated

with lower power at both sides of the signal and the pump wave. And the right idler is the signal converted wave.

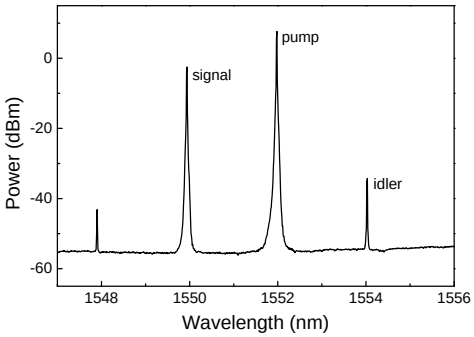

FIGURE 2.20: Measured FWM spectrum for a 5-mm silicon waveguide.

The power difference between the signal and idler wave is defined as the conversion efficiency, which is an important parameter in FWM. Normally, in the nonlinear process, the conversion efficiency is related to the nonlinear interaction length. Figure 2.21(a) shows the measured conversion efficiency in the silicon waveguides with different lengths. Although the longer waveguide provides higher conversion efficiency, it does not mean it will offer better performance in the signal processing. Since the propagation loss also largely increases as the waveguide length increases, with the same input pump power, the converted idler power exiting the waveguide may not increase. For instance, the propagation loss for the 2-cm long waveguide is 7 dB larger than that of the 5-mm long waveguide, however, the conversion efficiency for the 2-cm waveguide is only 5.2 dB higher which is not enough to overcome the increased loss. Therefore, the length 5 mm is used for the following characterization and the following system experiment.

The conversion efficiency can be also increased by the increasing the pumping power. As shown in fig. 2.21(b),the conversion efficiency increases linearly with the increasing pump power. However, two-photone absorption (TPA), an unavoidable detrimental nonlinear effect in silicon waveguide, limits the linearity if very large pump power is used. This TPA effect is investigated by measuring the variation of the insertion

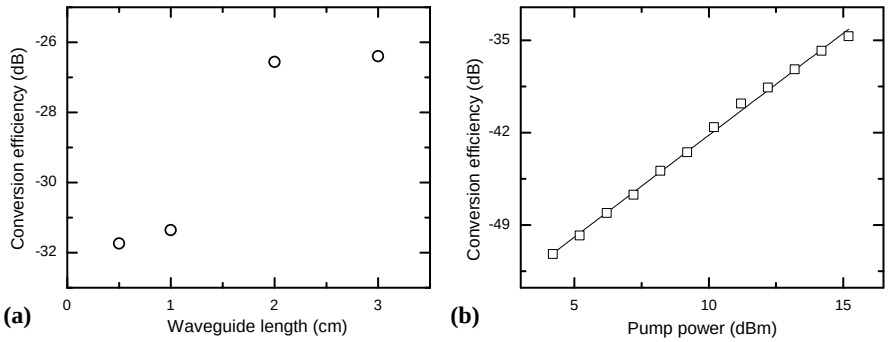

FIGURE 2.21: (a) Measured FWM conversion efficiencies of the silicon waveguide with different lengths. (b)Measured conversion efficiency as a function of CW pump power.

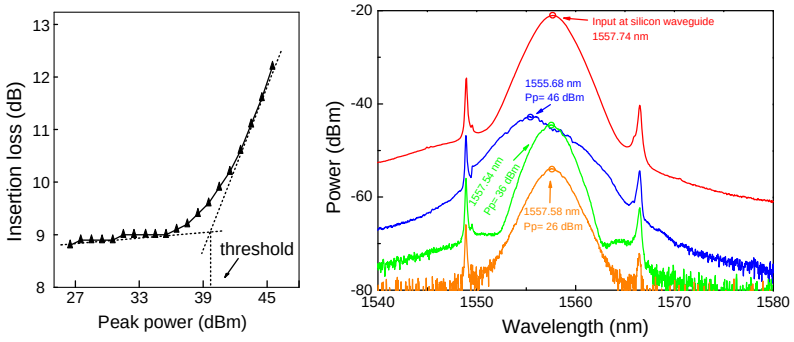

FIGURE 2.22: (Left) Measured insertion loss of the silicon waveguide with different input peak power. (Right) The input and output spectra for the silicon waveguide with different input power. Figure Courtesy of Hua Ji.

loss at different input peak powers. A pulse train with 16 MHz repetition rate is sent into the silicon waveguide and a tunable attenuator is used to adjust the input pump peak power. As shown in fig. 2.22, the insertion loss increases very slowly when the input peak power is relatively low but grows very rapidly at higher input peak powers. It indicates that there exists a threshold power ($\sim$37 dBm) at which the TPA induced free carrier absorption (FCA) increases significantly and costs more power. In addition, as shown in fig. if the input peak power

exceeds the threshold, the FCA and free carrier dispersion (FCD) effects will results in pulse spectrum broadening and blue shift which are all detrimental to the FWM process. Therefore, the input pump power need to be well controlled to avoid the TPA induced effects.

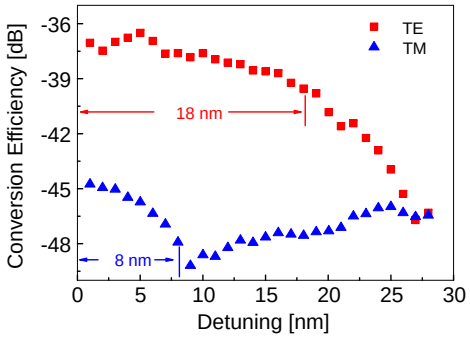

FIGURE 2.23: Measured FWM conversion efficiencies with different detuning.

The conversion bandwidth is another important parameter which is a measure about how far the idler wave can be away from the pump wave while keeping the conversion efficient. To measure the conversion bandwidth, the pump wave is fixed at 1560 nm and the signal wave is detuned up to 30 nm from the pump wavelength. Figure 2.23 shows the measured conversion efficiency as a function of detuning for both the TE and TM modes. The 3-dB FWM conversion bandwidths are 18 nm and 8 nm for the TE mode and TM mode, respectively. This difference is due to the different dispersion relations of TE and TM mode for the silicon waveguide. Large conversion bandwidth is desirable in the fast all-optical signal processing since the ultra short pulse has a relatively broad spectrum. Therefore, in the following system experiment, we always use the TE mode to get large conversion bandwidth.

2.4.2 Optical demultiplexing and sampling

Based on the FWM process, the silicon waveguide can be used for optical demultiplexing and waveform sampling in ultra-high speed OTDM

system. In an OTDM signal, bits from different channels are packed together such that the bits belonging to a specific channel are separated by $T_b = 1/B_{ch}$, where B_{ch} is the bit rate of each channel, whereas individual bits are spaced apart only $T_D = T_b/N_{ch}$ if N_{ch} channels are multiplexed together in the time domain. A specific channel can be demultiplexed if an optical pulse train at the repetition rate B_{ch} is used for pumping. During the FWM, the idler wave is generated only when the pump and signal pulses overlap in the time domain. And as a result, the idler will consist of a replica of the bit pattern associated with a single channel. If a low repetition rate sampling pluses with period T_s ($T_s \gg T_D$)[1] is used for pumping, the FWM occurs when the sampling pulses meet the data signal pulses. The new generated idler pulse train, including the amplitude information of the data signal, will reconstruct the waveform in a slow time scale realizing the waveform sampling.

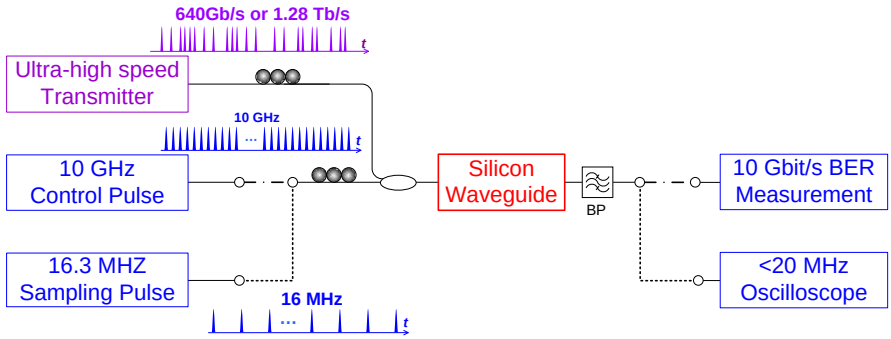

FIGURE 2.24: Experimental scheme: A 640 $Gbit/s$ or a 1.28 $Tbit/s$ serial data signal is injected into the silicon waveguide along with control pulses, either at 10 GHz for demultiplexing or at 16.8 MHz for optical sampling.Figure Courtesy of Hua Ji.

Figure 2.24 shows the full experimental scheme. The scheme allows for flexible switching between control pulse sources, to provide demultiplexing or optical sampling. For the demultiplexing, the OTDM serial data signal generated by the 640 Gbaud or the 1.28 Tbaud transmitter [89]

[1]There should exist a temporal offset ($\Delta t \neq 0$) between the date signal and the sampling source, where the temporal offset is defined as $\Delta t = (T_s/T_D - M) \cdot T_d$ and M is an integer.

is launched to the silicon waveguide, together with the 10 GHz control pulse train (dash dot line in fig. 2.24).

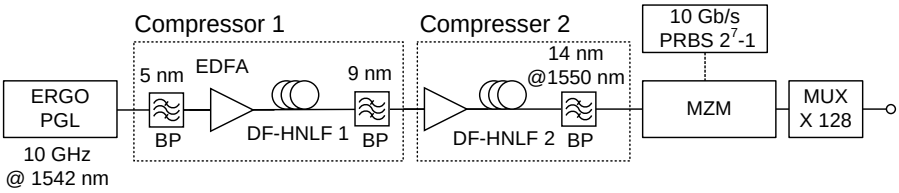

FIGURE 2.25: Schematic drawing of the 1.28 Tbaud transmitter used in the OTDM system. Figure Courtesy of Hua Ji.

Figure 2.25 shows how the 1.28 Tbaud transmitter generates a high speed OTDM serial data signal.An erbium glass oscillator (ERGO) optical pulse source generates a 10 GHz pulse train at 1550 nm with 1.5 ps full width half Maximum (FWHM). After amplification in an erbium-doped fiber amplifier (EDFA), the 10 GHz data pulses are sent into a dispersion flattened highly non-linear fiber (DF-HNLF) to broaden the optical spectrum. Then a band pass filter is used to filter out part of the spectrum compressing the pulses while at the same time shifting their wavelength. Then the pulses go through the second pulse compression stage and are compressed further using the same scheme of spectral broadening but without shifting the wavelength. A Mach-Zender modulator encodes a 10 $Gbit/s$ data sequence (PRBS 2^7-1) on the pulse train and the 10 $Gbit/s$ data signal is multiplexed by a passive fiber delay PRBS and polarization maintaining multiplexer (MUX). The number of multiplexing stages can be selected, so characterizations are conducted at both the moderate bit rate of 640 Gbaud, and at the record-high 1.28 Tbaud. The data signal is injected into the silicon waveguide together with control pulses. The 10 GHz control signal for demultiplexing is also generated from the 1.28 Tbaud transmitter, which comes out from compressor 1 and without data modulation.

For the waveform sampling, a 16.3 MHz sampling source is used (The dotted line in fig. 2.24). The sampling source is a fiber ring mode-locked laser, which uses 30 cm erbium fiber as gain medium and carbon nanotubes (CNT) as mode-locker [90]. The output pulses have squared hyperbolic secant shape with $\sim$750 fs FWHM. The central wavelength

of the pulses is 1558 nm and the 3 dB spectral bandwidth is 4 nm. In order to sample data signals at different wavelengths, the sampling pulses are shifted in wavelength. Here, self-phase modulation (SPM) creates spectral broadening, and the tunable filter can then pick out the desired wavelength. The FWM spectrum at the output of the silicon waveguide is shown in fig. 2.26 for the 640 $Gbit/s$ demultiplexing and sampling.

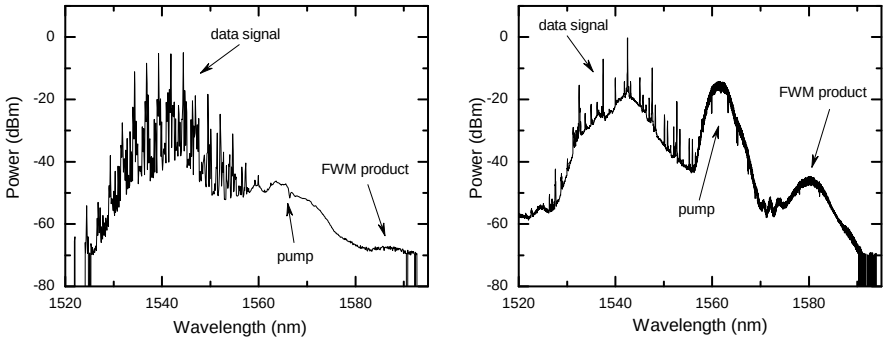

FIGURE 2.26: The output spectra from the silicon waveguide for OTDM 640 $Gbit/s$ waveform sampling (a) and demultiplexing from 640 $Gbit/s$ to 10$Gbit/s$(b). Figure Courtesy of Hua Ji.

In the sampling experiment, the data signal central wavelength for 640 $Gbit/s$ data signal is 1545 nm. To sample its waveform, the central wavelength of the sampling pulses is selected at 1565 nm. This gives an appropriate spectral distance which allows for separation of the FWM product from the sampling pulses while maintaining the high conversion efficiency. The pulse width of the sampling pulse is 750 fs. The average power of the data signal and sampling pulses sent into the nano-engineered silicon waveguide is 20 dBm and -9.7 dBm, respectively. The FWM product is filtered out at 1586 nm and directly detected. Figure 2.27(a) shows the waveforms for the 640 $Gbit/s$ sampling. Clear eye-diagrams is observed on the oscilloscope and the 500 fs pulses (measured by an autocorrelator) are seen in the 1.56 ps time slot without overlap between neighboring pulses and with minimal broadening to only 560 fs in the sampled trace.

For the 1.28 $Tbit/s$ sampling, the central wavelength of the signal is tuned to 1551 nm to fit the whole spectrum in the C-band since the optical spectrum of the 1.28 $Tbit/s$ signal is broader than at 640 $Gbit/s$. Accordingly, to sample the 1.28 $Tbit/s$ waveform, the sampling pulse wavelength is further compressed to 700 fs and shifted to 1574 nm. An open eye-diagram is shown in fig. 2.27(b). In this silicon waveguide-based sampling system, the ∼330 fs pulses, though broadened to 510 fs during the sampling process, are clearly distinguished in each of the 780 fs 1.28 $Tbit/s$ time slots. This is the first sampling demonstration result where the individual pulses of a Tbaud signal are clearly separated and the resolution of the silicon sampling system is the highest reported to date.

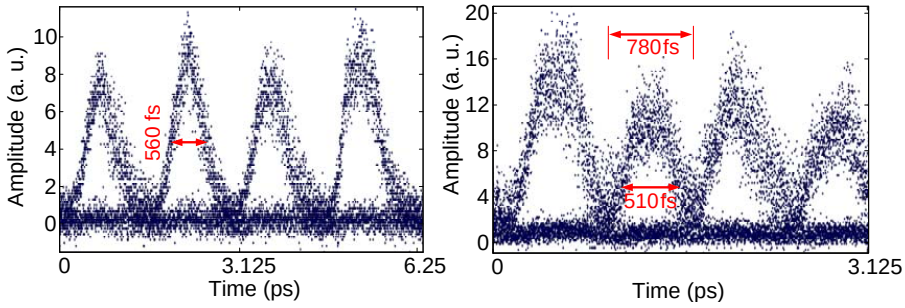

FIGURE 2.27: Eye-diagram of 640 Gbit/s (Left) and 1.28Tbit/s (Right) waveform for the optical sampling using the silicon waveguide. Figure Courtesy of Hua Ji.

In the 640 $Gbit/s$ to 10 $Gbit/s$ demultiplexing experiment, the data signal pulses are 500 fs FWHM pulse width with central wavelength at 1545 nm and the 10 GHz control pulse train with central wavelength at 1561 nm has 14 dBm average power and 1.2 ps pulse width. The FWM product is filtered out at 1584 nm and sent into the preamplified L-band receiver. While for 1.28 $Tbit/s$ to 10 $Gbit/s$ demultiplexing, the data signal pulses are compressed further to 330 fs FWHM and the control pulse width is 440 fs. This gives rise to a wider data spectrum at 1.28 $Tbit/s$, and so the wavelength separation between control and data must also be larger. The central wavelengths are selected at 1551 nm and 1574 nm for data signal and control pulses, respectively. The FWM product will be filtered out using a 5-nm band pass filter centered

at 1595 nm and then sent into a 10 $Gbit/s$ preamplified L- band receiver where the bit error rate (BER) performance is measured.

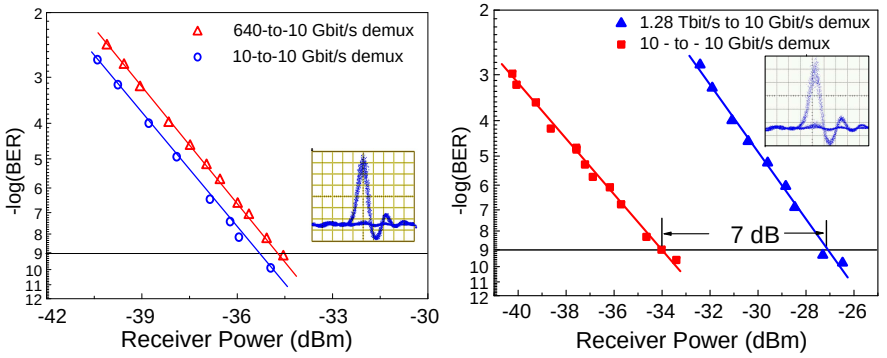

FIGURE 2.28: BER performance of demultiplexing for 640 $Gbit/s$-to-10 $Gbit/s$ (a), and 1.28 $Tbit/s$-to-10 $Gbit/s$ (b). The insets show clear eye-diagrams for the demultiplexed channels. Figure Courtesy of Hua Ji.

The bit-error-rate (BER) performance of the demultiplexing is measured and shown in fig. 2.28. For 640-to-10 $Gbit/s$ demultiplexing (see fig. 2.28(a)), an error-free operation with no error floor down to a BER of below 10^{-9} is achieved at -34.4 dBm. A reference 10-to-10 $Gbit/s$ demultiplexing, converting the 10 $Gbit/s$ signal from C-band to L-band, is also measured. Compared with this reference, the 640-to-10 $Gbit/s$ demultiplexing only has 0.6 dB penalty at error free operation and a clear eye-diagram of a 640-to-10 $Gbit/s$ demultiplexed channel can be found in the inset of fig. 2.28(a). For the 1.28 bit/s-to-10 $Gbit/s$ demultiplexing, an error free operation is achieved at -27.3 dBm receiver sensitivity as shown in fig. 2.28(b). with no sign of an error floor, thus clearly demonstrating the Tbit/s processing capabilities of the silicon waveguide platform. There is a 6.7 dB penalty compared to the L-band 10 $Gbit/s$ reference. This higher penalty compared to the 640 $Gbit/s$ demultiplexing is believed to be caused partly by pulse tail overlap in the $Tbit/s$ data signal, resulting in intersymbol interference, and partly by a limited FWM bandwidth of this device. This means that the silicon waveguide can handle the $Tbit/s$ speeds signal processing, and a more

careful design for GVD of the silicon waveguide may further improve its performance.

2.5 Summary

This chapter presented the basic theory of silicon waveguide. The single mode condition is described for ridge waveguides. For the 250-nm and 300-nm thick ridge waveguides, the waveguide widths should be controlled below 530 nm and 460 nm, respectively to avoid the multi-mode operation which normally result in the performance degradation of silicon waveguide devices. The dispersion property of the sub-micron silicon ridge waveguide is also discussed. Due to the tight light confinement in the ridge waveguide, the waveguide dispersion dominate over the material dispersion and make the GVD of the silicon waveguide highly engineerable. Since the dispersion properties of the waveguide is quite important in the nonlinear optical signal processes, the waveguide dimension can be altered to tailor the GVD to fit specific nonlinear processes.

The coupling problem between the sub-micron silicon ridge waveguide and the single mode fiber is addressed in this chapter. The inverse taper coupler embedded in a polymer waveguide is introduced. How the critical parameters of the inverse taper (taper tip width, taper height) influence the coupling efficiency is investigated. Normally, a very efficient coupling (coupling loss <1 dB) for TE mode can be achieved if the taper is fabricated with a tip width less than 120 nm. However, an extreme narrow tip width for the inverse taper is necessary to obtain the same coupling performance for the TM mode. The fabrication process of the silicon ridge waveguide integrated with the inverse taper couplers is also described here together with the basic introduction of electron-beam lithography and reactive-ion etching techniques. The dry thermal oxidation process is utilized to make the ultra narrow inverse taper tip. In the characterization of the inverse taper coupler, we measured the propagation loss of the ridge waveguides, the insertion loss of the tapered fibers, and the coupling loss of the inverse couplers. The propagation loss for the ridge waveguide with and without the thermal

oxidation are ∼4.7 dB and ∼4.2 dB, respectively. And the lowest coupling losses of the inverse taper couplers we obtained are 0.66 dB for the TE mode and 0.36 dB for the TM mode which is the smallest loss ever reported to date.

We also investigated the performance of the silicon waveguide including conversion efficiency, conversion bandwidth, TPA and FCA effects in the FWM which is an nonlinear parametric process that can be used for the fast optical signal processing like the optical demultiplexing and waveform sampling. In an ultra-fast OTDM system, we demonstrate that the silicon ridge waveguide enable successful optical waveform sampling and error-free demultiplexing both for 640 $Gbit/s$ and 1.28 $Tbit/s$ serial data signals. In the waveform sampling, the 330 fs pulses can be distinguished clearly in each of the 780 fs 1.28 $Tbit/s$ time slots. An error free operation is achieved at -27.3 dBm sensitivity with no sign of an error floor in the 1.28 $Tbit/s$-to-10 $Gbit/s$ demultiplexing. These experimental results, the high resolution sampling and the fastest silicon photonic optical signal processing, indicate a great potential of nano-engineered silicon waveguide based ultra-fast optical signal processing.

Chapter 3

Microring resonator

Microring resonators (MRRs), proposed by Miller and Marcatili in 1969 [91, 92], are versatile wavelength-selective elements that can be used to synthesize a wide class of functions. It has become the most prominent photonic structure in the recent investigations and has received increasing amounts of attention due to its compact size, low loss, transparency to off-resonance light, and no intrinsic reflection. MRR has been implemented in a variety of material systems. Silicon-on-insulator (SOI) technology offers waveguides with high-index-contrast between the core and cladding, thereby allowing bending radii on the order of micrometers and enabling high-density integration of photonic devices. In addition, the SOI MRR can also be implemented on the complementary metal-oxide-semiconductor (CMOS) platform which makes it an attractive solution for integration photonic signal processing with conventional electrical processing.

The silicon MRR can act as an optical filter [35, 38], and can be made in the electro-optical modulators [39–41], lasers [12] and detectors when carrier injection, optical gain or optical absorption mechanisms are incorporated. Since those devices covers almost all the optical devices required for the on-chip interconnect application, the silicon MRR is believed to be a building block for the on-chip photonic network. It can also find applications in areas such as optical processing of microwave signals in wireless communication systems [93–95].

Nowadays, all the microwave signal processing functionalities in wireless communication systems are realized using digital electronics. However, the speed and bandwidth of the electronic methods will be limited as the microwave carrier frequency is extended into the millimeter-wave regime in the future [96]. To satisfy the requirements for higher carrier frequencies and larger bandwidth, integrated photonic devices can be employed to realize various functions in microwave fields, some of which are very complex, or even impossible to do directly in the microwave domain. Silicon MRR, as one of the basic photonic components, can be utilized to realize microwave phase shifter due to its filter characteristics. Microwave phase shifter are key components in many microwave applications, such as phased-array antennas [51] and microwave filters [52]. In these applications, a full 2π tunability and small radio frequency (RF) power variation are highly desirable for the microwave phase shifter. In this chapter, how to use the MRR to achieve large microwave phase shift with minimum power variation is addressed.

There are two basic building blocks for any MRR-based devices. One is the all-pass type structure in which the microring is side coupled to a single waveguide while the other is the add-drop type structure in which the ring is side-coupled to two waveguides. This chapter begin with the theory for the all-pass type MRR. And then the microwave phase shifter based on this type resonator will be investigated. The microwave filter based on the same type MRR is also discussed. Following that, the add-drop type MRR will be introduced. As this type of MRR is widely used in optical communication systems, one of its applications in generating high repetition rate pulse is presented at last.

3.1 All-pass type microring resonator

3.1.1 Transfer characteristics

The all-pass type MRR consists of a single straight waveugide and a microring as shown in fig. 3.1. The microring supports circulating waves that resonate at a guide wavelength λ for which $N\lambda = L$, where N, an integer, is the mode number and L is the circumference of the microring.

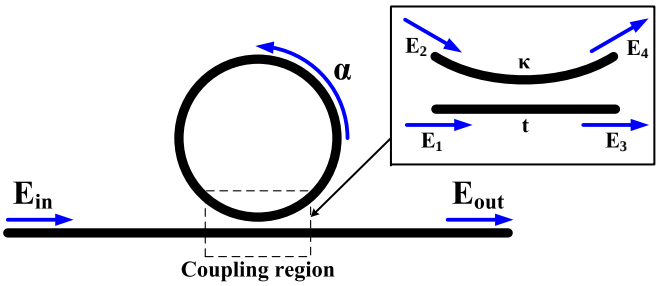

FIGURE 3.1: Schematic of an all-pass type MRR.

This relationship indicates that the resonances are spaced periodically on the frequency or wavelength scale, much like those of a comb filter. The separation between consecutive resonances, the so-called free spectral rang (FSR) is the inverse of the time delay of the signal in the microring and is therefore inversely proportional to the length of the perimeter. The FSR can be expressed in different forms as below:

$$FSR_\omega = \frac{2\pi c}{n_g L} \tag{3.1}$$

$$FSR_\lambda = \frac{\lambda^2}{n_g L} \tag{3.2}$$

In the MRR, as the light is propagating through the straight waveguide, the light power will be exchanged between the straight waveguide and the bending waveguide in the coupling region as denoted as the dashed square shown in the fig. 3.1. The power exchange can be described by an universal matrix relation [97]:

$$\begin{bmatrix} E_3 \\ E_4 \end{bmatrix} = \begin{bmatrix} t & \kappa \\ \kappa^* & -t^* \end{bmatrix} \begin{bmatrix} E_1 \\ E_2 \end{bmatrix} \tag{3.3}$$

where t is the amplitude transmission coefficient and κ the amplitude coupling coefficient. Here, the complex mode amplitudes E_i, is normalized such that its squared magnitude corresponds to the modal power. If we assume that the total powers entering and leaving the coupling

region are equal, then the coupling matrix is unitary:

$$|t|^2 + |\kappa|^2 = 1 \tag{3.4}$$

The transmission around the ring is given by

$$E_2 = E_4 \alpha e^{i\theta} \tag{3.5}$$

where, α and θ are the round-trip amplitude gain, and the round-trip phase shift. And from the eq. (3.3-3.5), we can obtain the expression for the transmittances of complex fields at the waveguide output and in the ring as shown below:

$$\frac{E_3}{E_1} = \frac{t - \alpha e^{i\theta}}{1 - \alpha t e^{i\theta}} \tag{3.6}$$

$$\frac{E_2}{E_1} = \frac{i\alpha\kappa e^{i\frac{\theta}{2}}}{1 - \alpha t e^{i\theta}} \tag{3.7}$$

The transmission past the resonator in the input waveguide and the transmission into the resonator can be written as:

$$|\frac{E_3}{E_1}|^2 = \frac{\alpha^2 + t^2 - 2\alpha t cos\theta}{1 + \alpha^2 t^2 - 2\alpha t cos\theta} \tag{3.8}$$

$$|\frac{E_3}{E_1}|^2 = \frac{\alpha^2(1 - t^2)}{1 + \alpha^2 t^2 - 2\alpha t cos\theta} \tag{3.9}$$

The phase shift of the transmitted light can be then de derived as:

$$\phi = \pi + \theta + tan^{-1}\frac{tsin\theta}{\alpha - tcos\theta} + tan^{-1}\frac{\alpha tsin\theta}{1 - \alpha tcos\theta} \tag{3.10}$$

Most of the interesting features of this resonator occur near resonance where $\theta = m2\pi$, where m is an integer. And when the circulating waves in the microring is far away from the resonance, $\theta = m2\pi \pm \pi$. Due to the periodicity of the resonance, we can just analyze an MRR within the round-trip phase shift range $-\pi < \theta < \pi$, and $\theta = 0$ corresponds to the resonance while $\theta = \pm\pi$ corresponds to the off-resonance. At resonance, we can get:

$$|\frac{E_3}{E_1}|^2 = \frac{(\alpha - t)^2}{(1 - \alpha t)^2} \tag{3.11}$$

It shows that when $\alpha = t$, i.e. when the internal losses (represented by $1 - \alpha^2$) are equal to the power coupling from the straight waveguide to the microring (represented by κ^2), the transmitted power vanishes. This condition, known as the critical coupling coupling [75, 98] is due to perfect destructive interference in the outgoing waveguide between the transmitted field tE_1 and the internal field coupled into the output waveguide κE_2.

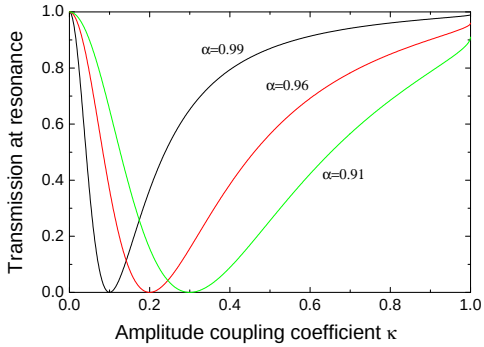

FIGURE 3.2: Transmission at resonance as a function of the coupling coefficient with different round-trip amplitude gains.

Figure 3.2 shows the calculated transmission at resonance as a function of the coupling coefficient (κ) with different internal gains (represented by α^2). To get the critical coupling, the power coupling need to be controlled to match the internal losses ($\kappa^2 = 1 - \alpha^2$). If the power coupling coefficient is smaller than the internal losses ($\kappa^2 < 1 - \alpha^2$), the MRR is in the under-coupling condition, while it is in the over-coupling condition if $\kappa^2 > 1 - \alpha^2$.

Normally, the coupling coefficient, which is related to the structure in the coupling region, can be controlled by altering the distance between the two waveguides. Different numerical methods could be used to calculate the coupling coefficient. Figure 3.3 shows an example relation between the power coupling coefficient κ^2 and the ring-to-waveguide gap (coupling gap). Here, we assume the radius of the microring is 250 μm and the cross section of the waveguide is 300×450 nm^2. It is clear that any power coupling coefficient between 0 and 1 is accessible by changing the

coupling gap. Therefore, the critical coupling can be easily obtained provided that the internal losses of the microring is known.

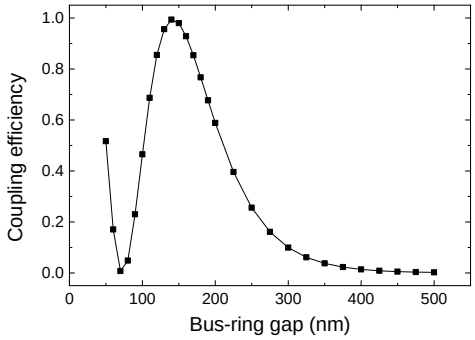

FIGURE 3.3: Power coupling coefficient as a function of the coupling gap between the microring and the straight waveguide. Here, we assume that the waveguide cross-sectional dimension is $300 \times 450\ nm^2$, the microring radius is 250 μm.

The quality (Q) factor is a measure of the frequency selectivity for an MRR and is given by the time averaged stored energy per optical cycle, divided by the power coupled or scattered out of the resonator. The Q-factor can be written as $Q = \frac{\omega_0}{\Delta\omega_{FWHM}} = NF$, where ω_0 is the center frequency of the resonance, $\Delta\omega_{FWHM}$ is the full width half maximum (FWHM) bandwidth, N is the mode number and $F = \frac{FSR}{\Delta\omega_{FWHM}}$ is the finesse. The $\Delta\omega_{FWHM}$ is defined as the width of the resonance half way between the maximum transmission and the minimum transmission for the all-pass type MRR. An approximation expression for $\Delta\omega_{FWHM}$ is

$$\Delta\omega_{FWHM} \cong \frac{2c(1-\alpha t)}{n_g L\sqrt{\alpha t}} \tag{3.12}$$

Figure 3.4 shows the finesse as a function of amplitude coupling coefficient for different round-trip gains (or internal losses). Critical coupling is marked on each curve with a small open circle. With the help of this plot the Q-factor of an MRR can be easily obtained providing the mode number is known. Although the critical coupling can be always obtained, the low internal loss for the MRR is desirable to get high finesse and thereby a high Q factor.

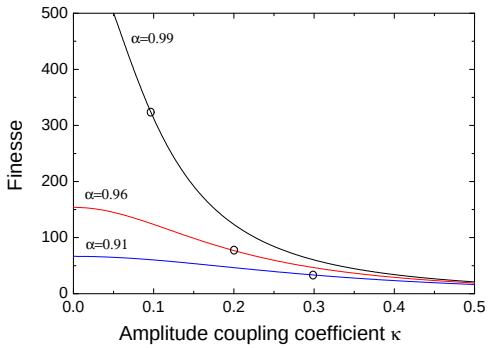

FIGURE 3.4: Finesse of the all-pass type MRR as a function of amplitude coupling coefficient κ with different round-trip amplitude gains. The small open circles indicate the locations of the critical coupling.

Figure 3.5 shows the transmission and phase at the through port with different power coupling coefficients κ^2. It is clear that as the coupling coefficient increases, the transmission notch depth first reach the maximum at the critical coupling condition and then decreases. While the transmission notch bandwidth continuously increases as the coupling coefficient increases which lead to a reduced Q-factor.

For the optical phase at the through port, when the coupling coefficient is low (under-coupling), the transmitted light exhibits a positive (negative) phase change at a negative (positive) detuning, and a graduate transition between these two regimes can be found around the resonance. As the coupling coefficient increases towards the critical coupling condition, this transition becomes sharper. The total phase change for the under- and critically-coupling condtions can not exceed π. However, as the coupling coefficient increased, a continuous and full phase change from $0-2\pi$ can be obtained at the over-coupling condition.

Normally, the all-pass type MRR can be used in the optical modulator [39–41], optical switch [42, 43], if it works near the critical coupling. And the special phase properties also make it suitable for optical delay and dispersive filters. In addition, the phase properties can also be used for the MRR to perform microwave signal processing. In the following subsection, the MRR-based microwave phase shifter is introduced.

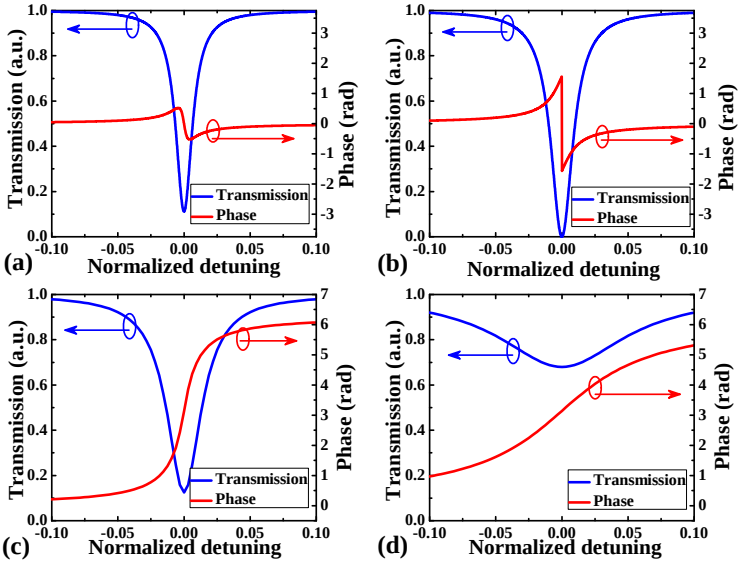

FIGURE 3.5: Transmission and phase shift of the through port for the MRR under different coupling conditions: (a) under-coupling $\kappa^2 = 0.005$, (b) critically-coupling $\kappa^2 = 1 - \alpha^2 = 0.01$, (c) over-coupling with $\kappa^2 = 0.02$ and (d) $\kappa^2 = 0.1$. Here, α^2 is always assumed to be 0.99.

3.1.2 Concept of photonic microwave phase shifter

The use of photonic elements to process microwave signals has attracted great interest since microwave systems can benefit from the characteristics of photonic components such as compact size, large bandwidth, fast tunability, immunity to electromagnetic interference and low weight. Microwave phase shifters are key components in many microwve applications such as phased-array antennas [51] and microwave filters [52].

Figure 3.6 shows the schematic layout of an RF phase shifter. The RF signal is imprinted on an optical signal via an external modulator generating an optical signal composed of a strong carrier at ω_0 and two major sidebands, red-shifted and blue-shifted by the RF frequency ω_{rf}. A notch filter is used to filter out one of the sidebands and then the optical signal with two frequency components is sent to the optical

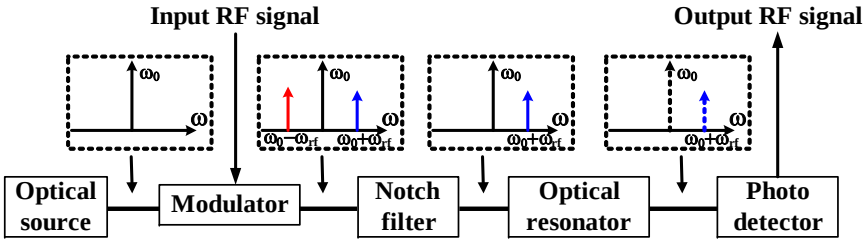

FIGURE 3.6: Schematic layout of an RF phase shifter.

resonator (here an MRR). The optical field input to the optical resonator can be expressed as

$$E(t) = A_0 exp(j\omega_0 t) + A_1 exp[j(\omega_o + \omega_{rf})t] \tag{3.13}$$

where A_0 and A_1 are the amplitudes of the two frequency components of the optical signal. The output field after the optical resonator can be therefore expressed as

$$E'(t) = A_0 A_0' exp(j\omega_0 t) \cdot exp(j\theta_0) + A_1 A_1' exp[j(\omega_o + \omega_{rf})t] \cdot exp(j\theta_1) \tag{3.14}$$

where A_0', A_1' and θ_0, θ_1 are the amplitude transmission gain and the induced optical phase shift at the corresponding frequencies for the MRR, respectively. Finally, the output optical signal is detected by a photo detector (PD) and the RF component of the output signal from PD is

$$i_{AC}(t) \propto \Re A_0 A_0' A_1 A_1' cos[\omega_{rf} t + (\theta_0 - \theta_1)] \tag{3.15}$$

where $\Re$ is the responsivity of the PD. The phase of the output RF signal is therefore determined by the optical phase difference $\theta_0 - \theta_1$. And if the resonance of the optical resonator can be tuned (between the two optical frequencies) to change the two optical phases, the phase difference can be varied and then realize the RF phase shift.

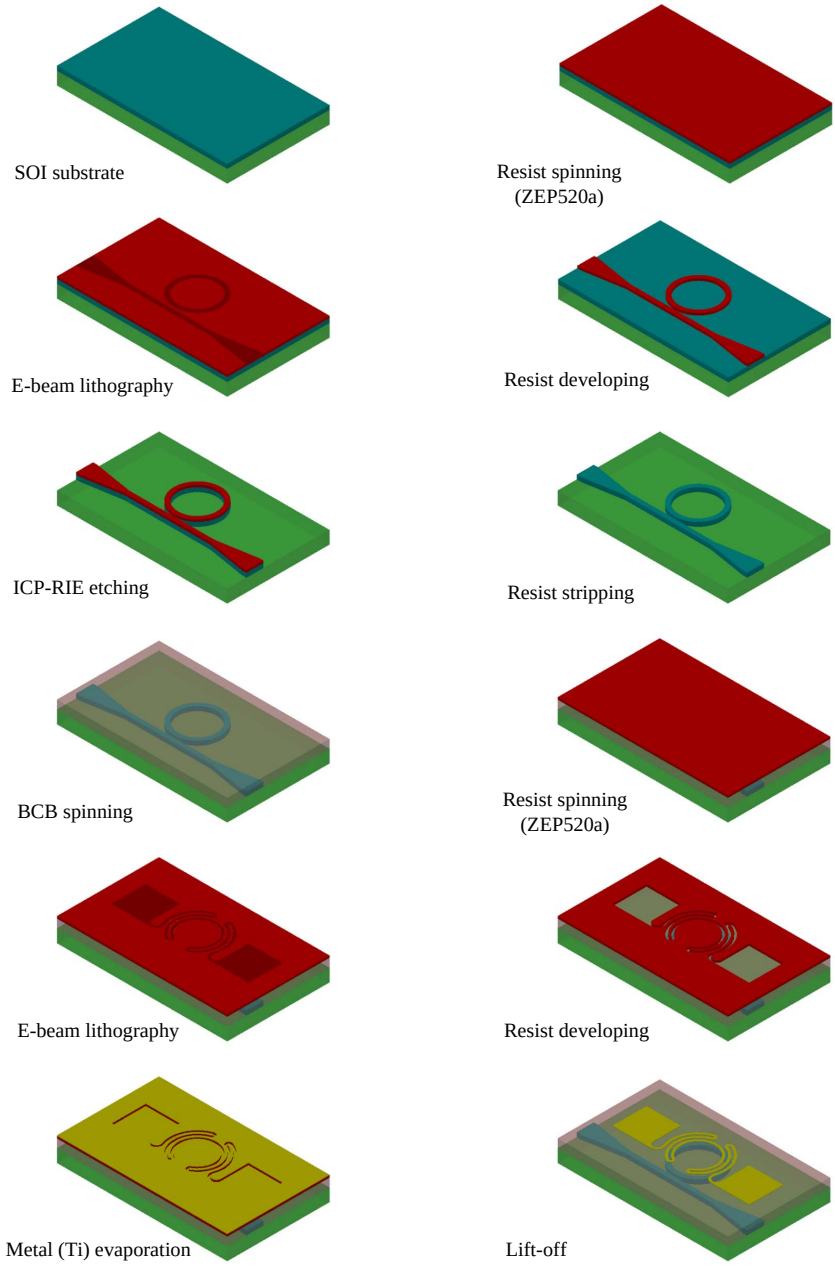

FIGURE 3.7: Fabrication process for the tunable MRR.

3.1.3 Tunable microring resonator

In the RF phase shifter, a tunable MRR is highly desirable since the RF phase shifting operation relies on the tuning of the resonance position for the MRR. The resonance position of an MRR can be controlled by altering the effective refractive index of the ring waveguide. And a simple expression relating the wavelength shift to the effective refractive index change can be derived from the resonant condition as below:

$$\frac{\Delta\lambda}{\lambda_0} = \frac{\Delta n_{eff}}{n_{eff}} \tag{3.16}$$

Thermo-optic (TO) tuning has been widely used for the silicon MRR since the TO coefficient (thermally induced index of refraction change) of the silicon material is as high as $2.4 \times 10^{-4}/^{\circ}C$. As the temperature increases, the refractive index of the silicon material become larger which results in a red-shift of the resonance wavelength. Typically, the resonance wavelength can be thermally tuned very efficiently with 0.11 $nm/^{\circ}C$ [38]. The response time for the TO effect is slow (normally in the order of microsecond) compared with the electro-optic effect (in the order of nanosecond) [99]. Although the tuning speed of the TO effect limits its application in ultra-fast devices like the optical modulator, optical switch [39], etc., it is not a vital factor for the RF phase shifting applications. Here we make the tunalbe MRR with micro heaters utilizing the TO tuning mechanism.

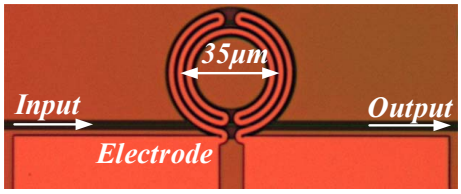

FIGURE 3.8: Optical microscope picture of the fabricated MRR with micro heater.

The fabrication process is shown in fig. 3.7. The tunable MRR was fabricated in an SOI wafer. Diluted (1:1 in anisole) electron-beam resist ZEP520A was spin-coated on the wafer to create a ∼110-nm thick

masking layer. The microring structure was defined in the ZEP520A layer with electron-beam lithography (JEOL JBX-9300FS). The patterns were subsequently transferred to the top silicon layer with inductively coupled plasma reactive ion etching (ICP-RIE). Then a 550-nm thick benzocyclobuten (BCB) top cladding was spin-coated and subsequently hard-cured. After that, 400 nm of ZEP520A resist and electron-beam lithography were employed again to define the pattern of the micro heater. Evaporation and lift-off techniques were used as the last steps to form 100-nm thick titanium heaters together with contact pads. At both ends of the device, the waveguide is tapered from 450 nm to 4 μm to expand the guided mode for more efficient fiber-to-chip coupling. The insertion loss of the device is 15 dB, where we estimate the fiber to waveguide coupling loss to account for 14 dB. This loss can be lowered down to 2 dB using suitable mode converters [32].

The micro heater is designed as shown in fig. 3.8 shows an optical microscope picture of the fabricated single MRR with micro heater. The electrical power dissipated at the heater can be explicitly expressed as

$$P = A\frac{V^2}{\rho L} \tag{3.17}$$

where V is the applied voltage, ρ is the metal resistivity, and A and L are the heater wire cross-section and length, respectively. This equation indicates that a larger cross-section leads to a smaller current density at the same power level.

To make an efficient thermal tunable MRR, we fabricated the tunable MRRs with different heater designs (different heater wire widths) and also with different SOI configurations (different silica buffer layer thicknesses). The tunabilities of the micro heaters are tested utilizing a single MRR with a coupling gap (ring-to-waveguide gap) of 200 nm between the ring and straight waveguide. The width of the waveguide is 450 nm and the diameter of the microring is 35 μm. Figure 3.9 shows the measured resonance shift as a function of the applied current on the micro heaters. From the fig. 3.9(a), it is found that the tunability for the micro heater with a 3-μm thick SiO_2 undercladding layer is about three times as that of the heater with 2-μm thick SiO_2 undercladding layer.

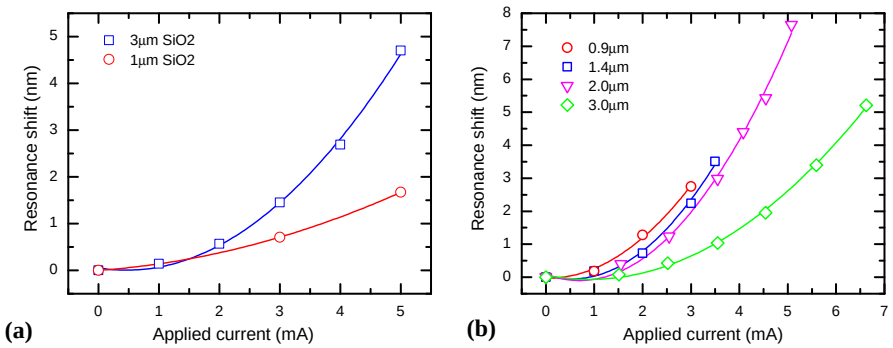

FIGURE 3.9: Measured resonance shifts as a function of applied current for tunable MRR with different designs: (a) different SiO_2 layer thickness, and (b) different heater wire widths.

A thick Silica (SiO_2) undercladding layer is desirable to enhance the efficiency of the heater since it can work as a thermal insulation layer. In addition, the efficiency is also dependent on the heater wire width, the heater with narrow wire width offers higher efficiency (larger resonance shift with the same applied current). However, as the narrow wire become narrow, the current density in the heater is largely increased which makes the allowed maximum current in the wire decreased thereby reduced the resonance shifting range in some cases. Therefore, a moderate wide micro heater with a large resonance shifting range is preferred to get a more stable tunability (e.g the heater with 2-μm wide wire).

Figure 3.10(a) shows the measured transmission spectrum for the MRR with 2-μm wide wire at different applied electrical powers. The 3-dB bandwidth of the resonant notch is 0.1 nm which corresponds to a Q-factor of 15,500. It is clear that the resonance red-shifts linearly as the applied power increases as shown in fig. 3.10(b). An electrical power of 40 mW is required for the resonance shifting range of a whole FSR, and the maximum achieved resonance shift is 8 nm with this design. In our devices, the BCB was chosen as the upcladding material for its excellent gap-filling and self-planarization capabilities. An SiO_2 uppercladding, however, can further enhanced the tuning efficiency due to the higher thermal conductivity of SiO_2 with respect to BCB if a specific application requires larger tuning range.

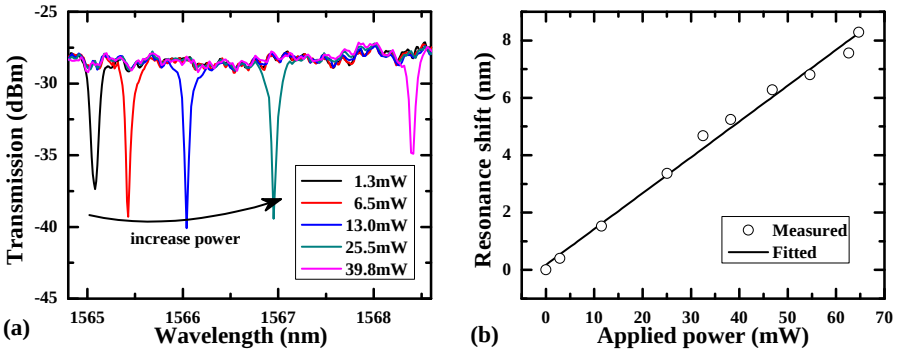

FIGURE 3.10: (a) Measured transmission spectra with different applied power on the micro heater for the MRR. (b) Measured resonance shift versus the applied power on the micro heater.

3.1.4 Microwave phase shifter based on single microring resonator

As mentioned previously in subsection 3.1.1, the optical phase experiences large phase change at the through port of an all-pass MRR. If the MRR is at the over-coupling condition, a maximum 2π phase change can be obtained in a small detuning range from the resonance which matches the requirement of the RF phase shifter.

Figures 3.11(a) and 3.11(b) show the optical intensity transmission and phase shift at the through port of the MRR with different amplitude coupling coefficients κ. Here, we assume the diameter of the SOI MRR is 35 μm and the effective group index of the SOI waveguide is 4.26 which correspond to a FSR of 640 GHz. The propagation loss of the SOI waveguide composing the ring is assumed to be 2 dB/cm. As shown in fig. 3.11(b), the phases experience monotonically a full 360° phase shift from negative to positive detuning with different curve shapes. Normally, smaller power coupling will result in a steeper phase change at the resonance.

If an optical signal carrying a microwave signal with two frequency components, i.e. a carrier frequency ω_0 and one sideband frequency $\omega_0+\omega_{rf}$,

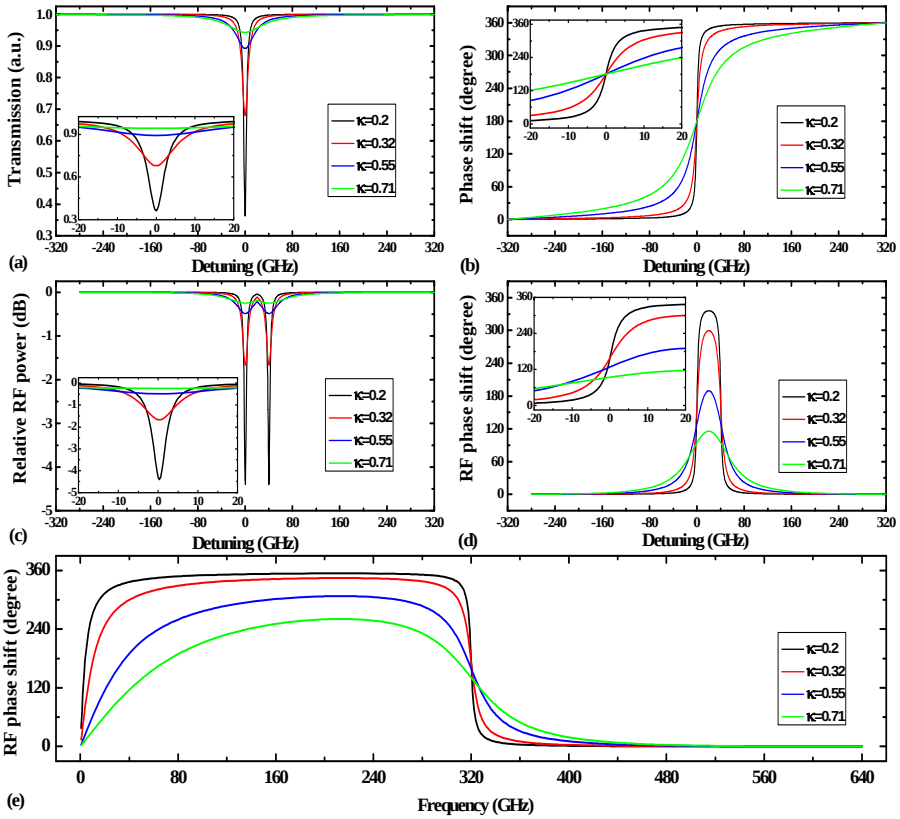

FIGURE 3.11: Optical intensity transmission (a) and phase shift (b) as a function of the detuning $(\omega - \omega_{MRR})$ at the through port for the MRRs with different coupling coefficients κ. RF power (c) and RF phase shift (d) for the MRRs as a function of the detuning $(\omega_{MRR} - \omega_0)$ at a RF frequency of 40 GHz with different coupling coefficients κ. All the insets are the zoomed view for a detuning range from -20 GHz to 20 GHz. (e) The maximum RF phase shift versus the RF frequency for the MRRs with different coupling coefficients κ.

is input to the MRR, the phase difference of the two frequency components can be changed in different ways depending on the value of the coupling coefficient κ of the MRR. In other words, the RF phase-shifting performance will be different for the MRRs with different coupling coefficients. Figures 3.11(c) and 3.11(d) show the RF power and RF phase shift, respectively, for the MRRs as a function of detuning of the resonance frequency (ω_{MRR}) from the carrier frequency (ω_0) over an FSR tuning range. Here, we assume the RF frequency (ω_{rf}) is 40 GHz. It is clear that the maximum RF phase-shifting range increases as the amplitude coupling coefficient decreases which results in Q-factor of the MRR (see fig. 3.11(d)). The RF power variation also increases with lower coupling coefficient (higher Q-factor) for the MRR as illustrated in fig. 3.11(c). The RF phase-shifting range can be further increased, though, for the larger amplitude coupling coefficients by increasing the RF frequency, as shown in fig. 3.11(e). The higher Q-factor MRR with lower coupling coefficient is always preferred if a large RF phase shifting range is expected. Note that the power coupling coefficient κ^2 should be always larger than the round-trip losses in the MRR $(1-\alpha^2)$ to keep over-coupling condition thereby ensure a 2π phase changing range.

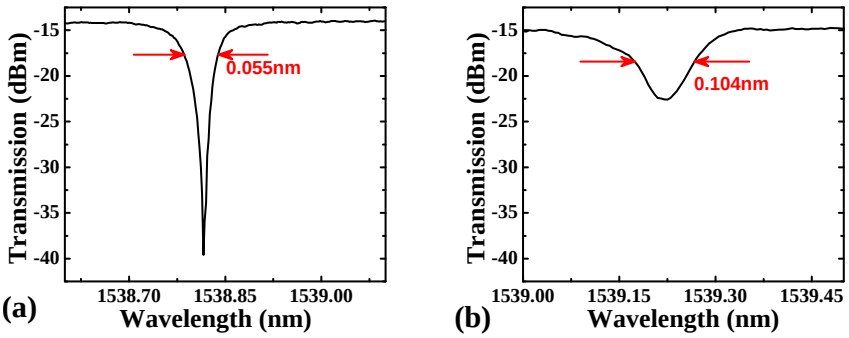

FIGURE 3.12: Transmission spectrum of the MRRs with a coupling gap of (a) 225 nm and (b) 100 nm for the TE mode.

MRRs with different ring-to-waveguide gaps (coupling gaps) are fabricated for the RF phase shifting experiment. The cross section of the waveguide is 250×450 nm^2 and the diameter of the MRR is 35 μm which corresponds to a FSR of 640 GHz. The transmission measurements are

performed using the setup mentioned in section 2.2.2. Figure 3.12(a) shows the transmission spectrum of an MRR with a coupling gap of 225 nm. The MRR has an extinction ratio of about 26 dB and 0.055-nm 3-dB bandwidth ($Q \sim 28,000$), slightly above the critical coupling condition. The spectrum for another MRR with a coupling gap of 100 nm is shown in fig. 3.12. Compared with the former MRR, the bandwidth of this MRR is largely increased and the extinction ratio is reduced to less than 3 dB. The smaller coupling gap in the latter MRR lead to an increased power coupling thereby decrease the Q-factor for the MRR.

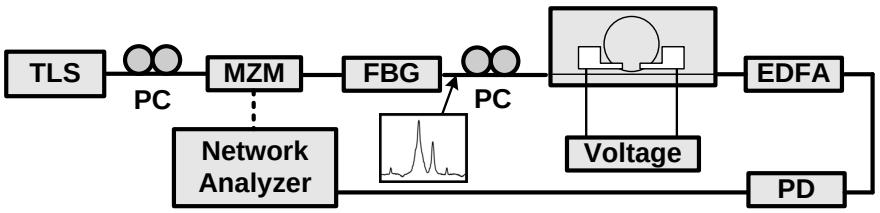

FIGURE 3.13: Experimental setup for RF phase-shift measurements. Inset shows the generated microwave signal after the FBG notch filter.

The experimental setup used to measure the fabricated device is shown in fig. 3.13. Light from a tunable laser source (TLS) was modulated through a Mach-Zehnder modulator (MZM) by a microwave signal from the network analyzer. A fiber Bragg grating (FBG) notch filter was used to filter out one sideband of the modulated signal [100]. After that, the optical signal, with the envelope modulated at the microwave frequency in the time domain (i.e., with two peaks of the desired frequency spacing in the spectral domain as shown in the inset of fig. 3.13) was generated and sent into the fabricated sample. The polarization of the input light was adjusted to the transverse electric (TE) mode with a fiber polarization controller (PC). By applying a voltage to the micro heater, the resonance frequency of the MRR can be tuned with respect to one of the peaks of the optical signal to change the phase difference between the two peaks. Amplified by an erbium doped fiber amplifier (EDFA), the output signal was detected by a PD, and converted to the microwave signal. Then the network analyser was used to extract the information of phase and power changes of the microwave signal.

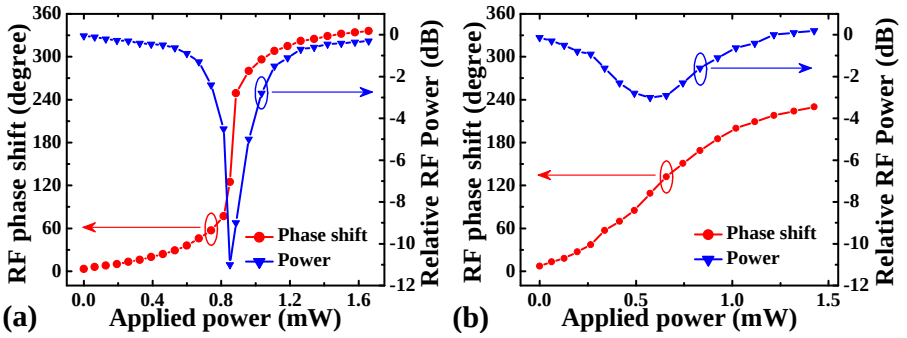

FIGURE 3.14: Measured RF phase shift and relative RF power versus the applied power to the micro heater on MRR with different coupling gaps: (a) 225 nm, and (b) 100 nm.

Figure 3.14(a) shows the measured RF phase shift and RF power variation as a function of applied electrical power to the micro heater. A continuously tunable RF phase shift is demonstrated, and the maximum RF phase shift of 336° is achieved. However, the large RF power variation (about 11 dB) due to the high extinction ratio of the MRR hampers the application as an RF phase shifter. This problem can be resolved by using a low-Q MRR with a higher coupling coefficient (narrower coupling gap), which will give a lower extinction ratio. The MRR with a coupling gap of 100 nm is also tested. The RF phase shift and RF power variation versus applied heating power are shown in Figs. 3.14(b). The RF power variation is about 1.3 dB, which is 9.7 dB smaller than that of the high-Q MRR. Although the maximum achievable RF phase shift ($\sim 204°$) is smaller due to the wide resonant bandwidth, the RF phase shift is more linear as compared to the high-Q MRR.

As mentioned previously, the maximum RF phase shift increases as the RF frequency increases, and then drops back to zero when the RF frequency approaches the FSR (640 GHz). The MRR with a lower coupling coefficient offers larger tuning range for the RF phase. The measured maximum RF phase shifts for different microwave frequencies modulated on the optical beam for the high-Q MRR are shown as the open circles in

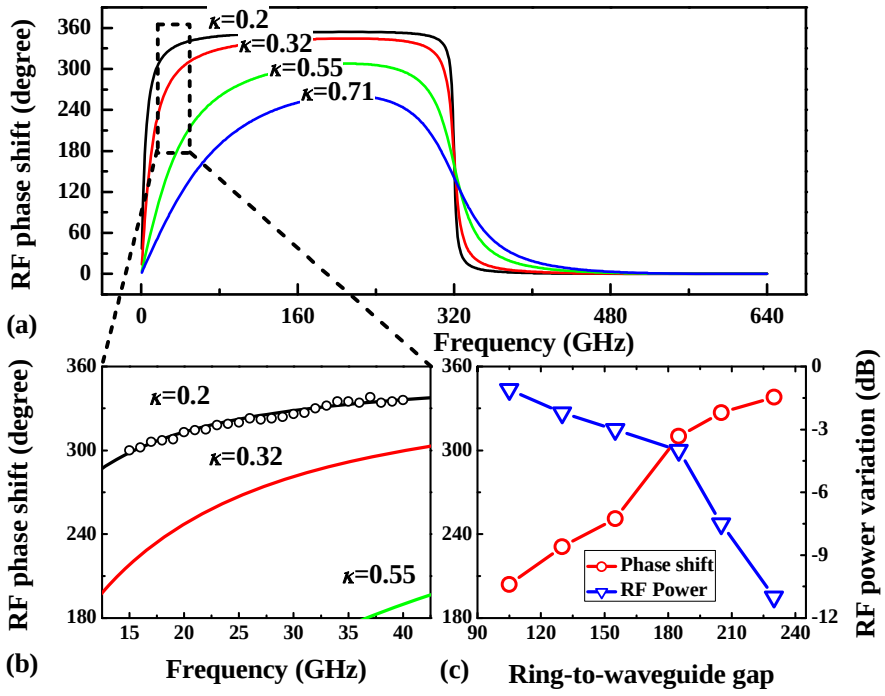

FIGURE 3.15: (a) Calculated maximum RF phase fhit versus the microwave frequencies for different coupling coefficients. (b) Zoomed view of (a) within the frequencies from 13 to 42 GHz. Open circles are the measured maximum RF phase shift versus the microwave frequencies with the MRR of 28,000 Q-factor. (c) Measured maximum RF phase shift and RF power variation for MRRs with diffeerent ring-to-waveguide gaps at a frequency of 40 GHz.

fig. 3.15(b), which shows a good agreement with the theoretical prediction. Figure 3.15(c) shows the measured RF power variation and maximum RF phase shift for the MRRs with different amplitude coupling coefficients (different coupling gaps). As the coupling gap increases, the coupling coefficient κ decreases which leads to a larger Q-factor and a higher extinction ratio. One finds that the MRR with higher Q (lower κ) provides a larger RF phase shift. However, the lower-Q MRR gives a smaller RF power variation at the expense of reduced maximum RF phase shift. Although a maximum phase shift of 336° can be achieved,

it is difficult to realize a full 360° phase shift by using a single MRR. This limits its practical applications in microwave systems since many applications, such as microwave photonic filters [101, 102] require phase shiters with a full 360° tuning range. In addition, the RF power varies dramatically during the phase shifting operation for the high-Q MRR which limits the applications. Therefore, the low-Q MRR with small RF power variation and good phase-shift linearity would be a more practical option for the real applications. In this case, two cascaded MRRs are necessary to achieve a full 360° RF phase shift.

3.1.5 Microwave phase shifter based on dual-microring resonator

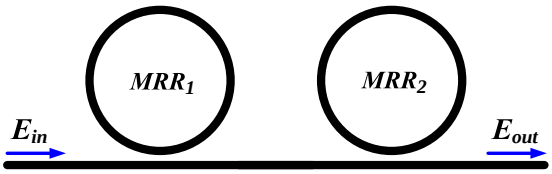

FIGURE 3.16: Schematic of an all-pass DMRR.

Figure 3.16 shows the schematic drawing of an all-pass dual-microring resonator (DMRR). The two cascaded rings are designed to have the same nominal geometries. Here, we also assume that an optical signal with two frequency components (ω_0 and $\omega_0 + \omega_{rf}$) is injected to the DMRR. The diameter of the two MRRs and the RF frequency are $35\mu m$ and 40 GHz, respectively.

Figure 3.17 illustrates the optical intensity transmission, the RF power, the optical phase shift and the RF phase shift for the DMRR at the through port with different resonance offsets ($\omega_{MRR2} - \omega_{MRR1}$) between the two MRRs. A total optical phase shift of 720° can be achieved for the DMRR. As shown in Figs. 3.17(a) and 3.17(c), the transmission spectrum and the phase curve can be altered by offsetting the resonances for the two MRRs. When the resonance offset increases from 0 to 3 GHz, the notch bandwidth increases, with a reduced notch depth, and

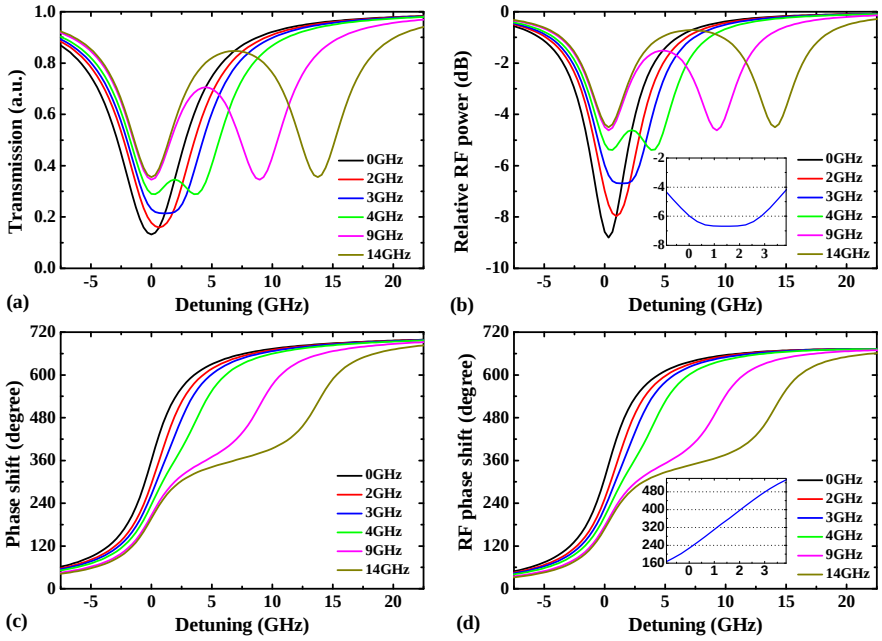

FIGURE 3.17: Optical intensity transmission (a) and phase shift (c) as a function of the detuning ($\omega_0 - \omega_{MRR1}$) for the DMRR with different resonance offsets ($\omega_{MRR2} - \omega_{MRR1}$). RF power (b) and RF phase shift (d) as a function of the detuning ($\omega_{MRR1} - \omega_0$) at an RF frequency of 40 GHz. Insets are zoomed views for the DMRR with 3-GHz resonance offset for a detuning range from -1 GHz to 4 GHz. Here, κ^2, α_2 are always assumed to be 0.04 and 0.995, respectively.

the bottom of the notch becomes flat. As the resonance offset increases further, the notch splits into two notches while the phase curve acquires a step-like shape. The RF power and RF phase shift behave in a similar way, as shown in figs. 3.17(b) and 3.17(d). Therefore, the resonance offset can be tuned to a desired value (e.g., 3 GHz in this case) to obtain a wide notch bandwidth, a decreased notch depth and a flattened notch bottom, and if the RF phase shifter is operated within this flat regime, one can realize an RF phase shift in a certain range with minimal RF power variation since the RF power follows the optical power. The insets in Figs. 3.17(b) and 3.17(d) show the zoomed views for the RF phase shift and RF power variation, respectively, in the detuning range

from -1 GHz to 4 GHz for the DMRR with a fixed resonance offset of 3 GHz. One can find that a quasi-linear phase-shifting range of 360° can be obtained with less than 2.4 dB RF power variation. A tuning range of 90° with negligible RF-power variation can also be found within the detuning regime from 0.95 GHz to 1.92 GHz. Compared with the phase shifter based on single MRRs (see insets in Figs. 3.11(c) and 3.17(d)), the DMRR-based phase shifter offers a larger phase shifting range, a more linear phase shift of 360° together with a much lower RF power variation. The bandwidth of the flat bottom regime can be further increased by a careful design of the Q-factor of each MRR and an optimal resonance offset between the MRRs, resulting in an increase of the tuning range with constant RF power.

In the above analysis, we fixed the resonance offset of the two MRRs. We can also suppress the RF power variation over a larger tuning range by varying the resonance offset during the phase-shifting operation since the two cascaded MRRs are designed to be tuned independently.

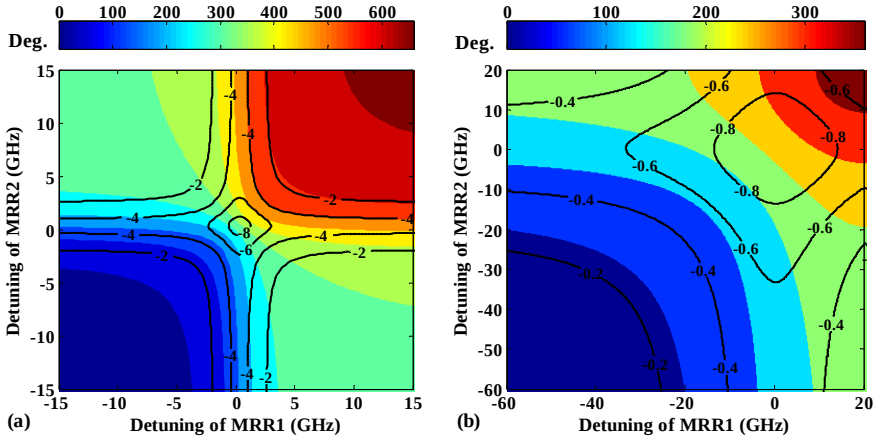

FIGURE 3.18: Contour plots of RF phase shift for a 40-GHz signal (in degrees, color-shaded contours) and RF power (in decibels, black-curve contours) as a function of the detuning of resonance frequencies (ω_{MRR1} and -ω_{MRR2}) from the optical carrier frequency (ω_0) for the DMRRs with power coupling coefficient κ_2 of 0.04 (a) and 0.3 (b), respectively.

Figure 3.18(a) shows the RF phase shift and the RF power as a function of detuning of resonance frequencies (ω_{MRR1} and ω_{MRR2}) from the optical carrier frequency (ω_0) for the DMRRs with power coupling coefficient $\kappa^2 = 0.04$. One can find that there are regions where the contour lines for RF phase shift (color-shaded contours) and RF power variation (black-curve contours) are not parallel. Therefore, the RF phase shift and the RF power can be tuned independently to some extent. If the tuning of the resonances of the two MRRs can be controlled in such a way that one of the contour lines for RF power is followed, there would be no RF power variation in the phase shifting process. For instance, if we follow the -6 dB power contour curve, a continuous phase shifting range of 280° can be obtained. The maximum continuous RF phase shifting range without power variation depends on the Q-factor of each MRR. The performance of a phase shifter based on a DMRR with a higher power coupling coefficient of 0.3 (lower Q-factor) is also illustrated in Fig. 3.18(b). Although the operating RF power level becomes higher and less sensitive to the detuning of the resonances, the maximum phase shifting range that can be achieved following one contour line is decreased to ∼190°.

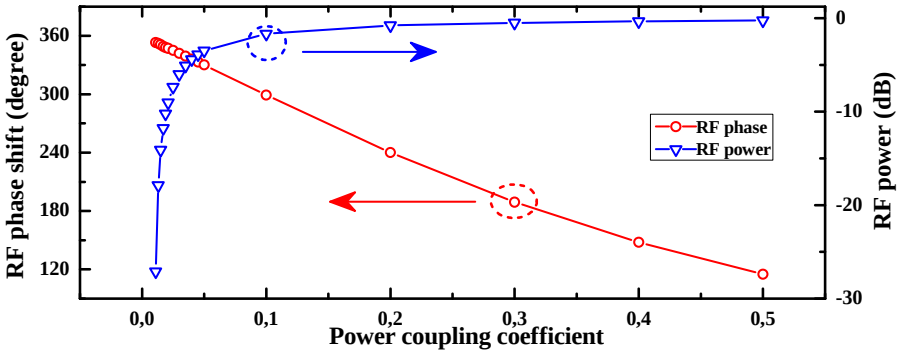

FIGURE 3.19: Maximum RF phase shift and RF power level for constant-power operation as a function of the power coupling coefficient κ_2.

Figure 3.19 shows the maximum RF phase-shifting range without power variation and the operating RF power level as a function of power coupling coefficient κ^2 of the DMRR. It is obvious that the phase shifter

based on higher Q-factor DMRR (lower coupling coefficient) offers larger tuning range without power variation at the expense of an increased overall RF-power loss. Since the absolute operating RF power is of less importance for such a microwave phase shifter, a DMRR with high Q-factor is more preferable in this case.

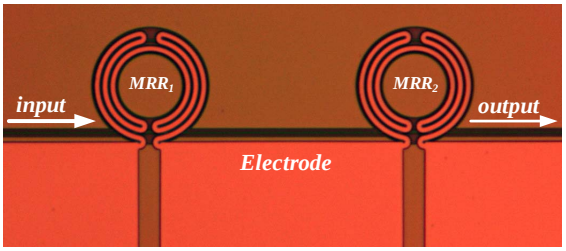

FIGURE 3.20: Optical microscope picture of the fabricated DMRR with micro heater.

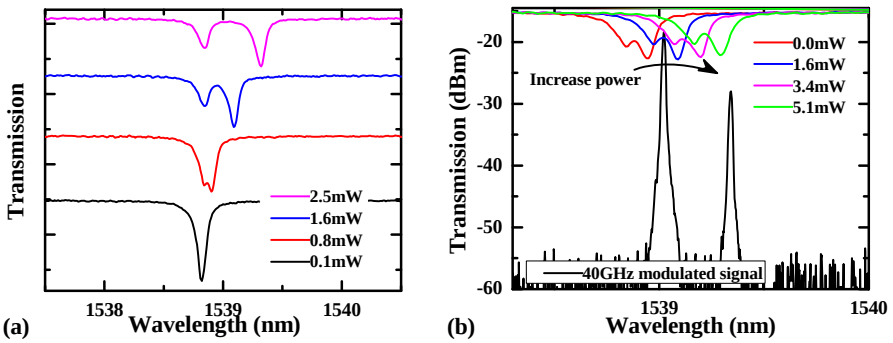

FIGURE 3.21: (a) Measured transmission spectrum of the DMRR with different applied power on the micro heater for MRR_1). (b) Measured transmission spectrum of the DMRR with additional applied power on both micro heaters (see the color curves) and the generated 40-GHz microwave signal with carrier wavelength of 1539 nm (see the black curve). Here, 0.8-mW power is initially applied on micro heater for MRR_1).

The setup for the RF phase shifting is the same as that in section 3.1.4. The DMRR used in the RF phase shifting experiment is shown in fig. 3.20. The micro heaters are integrated with both MRRs and make them

can be independently controlled. The coupling gap for the DMRR is about 150 nm. When applying current to one of the micro heaters (i.e., the micro heater for MRR_1), the transmission spectrum can be altered as shown in the fig. 3.21(a). In the RF phase shifting measurement, we applied 0.8 mW initially on MRR1 to get a suitable resonance offset between the two MRRs. By adding extra power equally to both micro heaters simultaneously, the resonance frequency of the DMRR can be tuned together with respect to one of the peaks of the optical signal, as illustrated in fig. 3.21(b), and then the phase difference between the two peaks is changed.

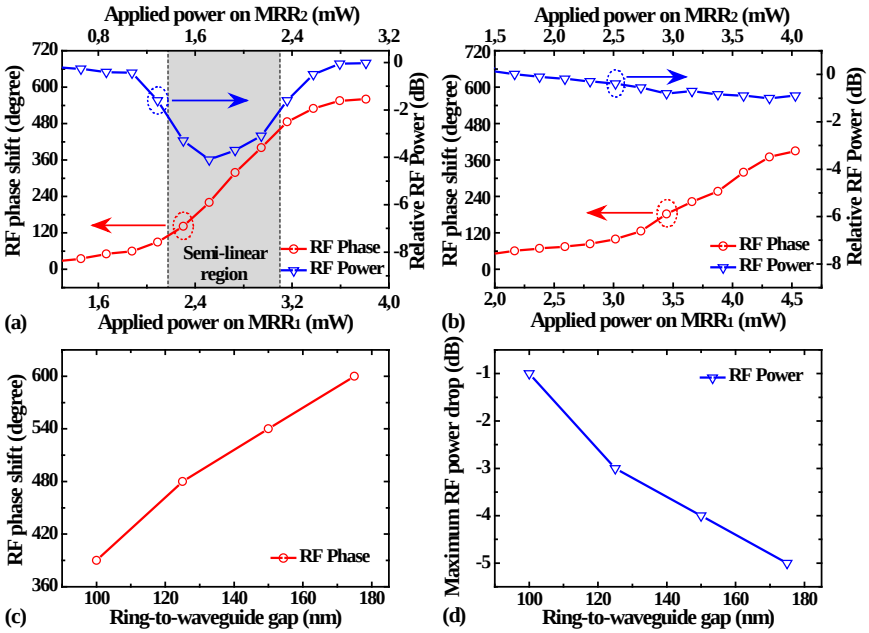

FIGURE 3.22: Measured RF phase shift and RF power versus the power applied to the two micro heaters for the DMRR with a coupling gap of 150 nm (a) and 100 nm (b). Measured maximum RF phase shift (c) and RF power drop (d) for the DMRRs with different power coupling coefficients.

The measured RF phase shift and RF power variation for a 40 GHz microwave carrier as a function of the applied electrical power on both

micro heaters are shown in fig. 3.22(a). A continuously tunable RF phase shift is demonstrated, and the maximum RF phase shift of 540° is achieved with the RF power variation of ∼4 dB. However, if the device is operated within the gray region shown in fig. 3.22(a), one can obtain not only a quasi-linear phase shift of 360°, but also an RF power variation of only 2 dB. In this case, the total required electrical power for phase tuning is ∼2 mW. As compared to the single-MRR based device mentioned previously, not only a larger and more linear RF phase shift is achieved, but also the RF power variation is largely suppressed. Figure 3.22(b) also shows the measured result for another DMRR with a smaller coupling gap of 100 nm (larger power coupling coefficient κ_2=0.33) which corresponds to a lower Q-factor. For this measurement, the reference power applied to the micro heater for the MRR_1 was set to 0.5 mW to get a suitable fixed resonance offset between the MRRs. A phase shift of 390° is still achieved as shown in fig. 3.22(b). Although the maximum phase shift is reduced from 540° to 390° and the total required heating power is increased to ∼8.5 mW, the total RF power variation in the whole tuning range is only 1 dB which is much smaller than that of the high-Q device. Figures 3.22(c) and 3.22(d) show the measured maximum RF phase shift and maximum RF power drop, respectively, for the DMRRs with different power coupling coefficients (different Q-factors). The DMRR with higher Q-factor (smaller power coupling coefficient) provides larger RF phase shifting range together with larger RF power variation as shown in figs. 3.22 and 3.22(d), which complies with the simulation results. The maximum phase shifting range of 0∼600° was achieved by using a DMRR with a coupling gap of 175 nm which corresponds to a power coupling coefficient of 0.11.

Figures 3.23(a) and 3.23(b) present the measured RF phase shift and RF power as a function of the applied power on the micro heaters for MRR_1 and MRR_2 of the DMRRs with a coupling gap of 150 nm and 100 nm, respectively. The dotted lines in both figures show the phase shifting operations in the previous measurements with fixed resonance-offsets. One can find that this is not the optimal way to suppress the RF power variation. The applied power on the micro heaters for MRR_1 and MRR_2 can be adjusted independently along a power contour line (i.e., the upper -2 dB solid contour line in fig. 3.23(a)) to realize the phase shifting. As shown in fig. 3.23(a), a phase-shifting range from 180° to 450° can

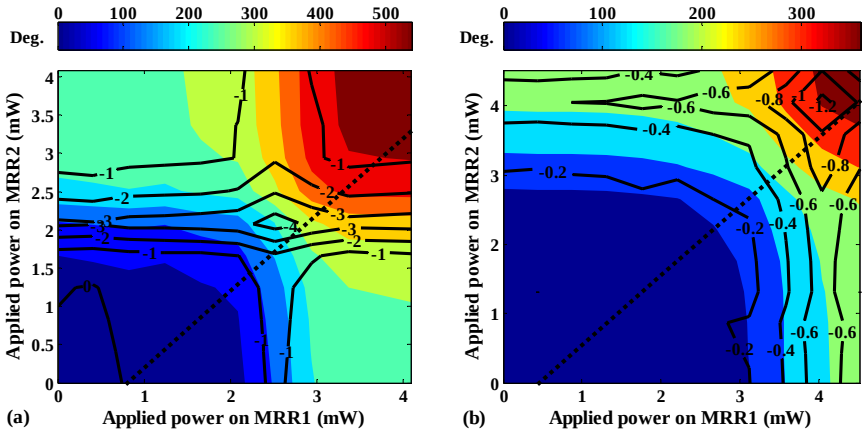

FIGURE 3.23: Contour plots of measured RF phase shift (in degrees, color-shaded contours) and RF power (in decibels, black-curve contours) as a function of the powers applied to the two micro heaters for the DMRR with a coupling gap of 150 *nm* (a) and 100 *nm* (b). The dotted lines represent the RF phase shifting operations in figs. 3.22(a) and 3.22(b), respectively.

be obtained in this way without noticeable RF power variation for the DMRR. And if we can tolerate 1 *dB* RF-power variation, we can obtain a continuous full 360° phase shift when operation is performed within the region defined by the two upper contour lines of -2 *dB* and -3 *dB* (fig. 3.23(a)). For the DMRR with lower Q-factor (narrower coupling gap), the maximum phase shifting range without power variation is smaller, just as the theoretical prediction mentioned previously.

Compared with the single-MRR device, the phase shifter based on a DMRR offers larger phase shifting range and more controllable RF power variation. These two advantages make the proposed device potentially useful in practical and versatile microwave applications such as microwave filter which will discussed in the following subsection.

3.1.6 Tunable microwave filter based on dual-microring resonator

Microwave filters are widely used, in all kinds of wireless communication systems, to combine or separate multi-frequency bands and to suppress noise or unwanted signals [103, 104]. Figure 3.24 shows the schematic layout of a tunable photonic microwave notch filter. It is a MZ configuration with an RF phase shifter in one arm and a time delay line in the other arm. Due to the time delay difference between the two arms, the RF signal will have a periodic notch spectral response at the output of the filter. The tunability of the filter can be realized by either adjusting the time delay difference [105–108] or changing the phase for the RF signal in one arm [101, 109, 110]. Since the former method also results in a change of the FSR, we choose the latter method to realize the tunability of the photonic microwave filter utilizing a DMRR-based RF phase shifter.

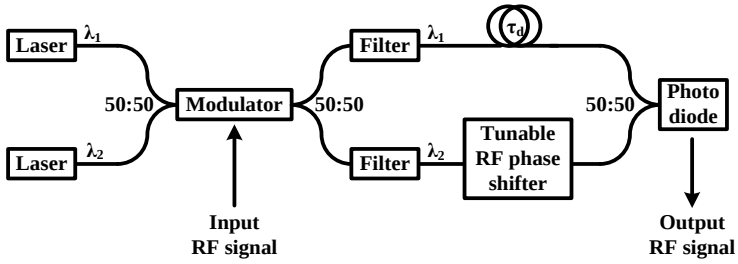

FIGURE 3.24: Schematic layout of a tunable photonic microwave notch filter.

The experimental setup to implement the microwave notch filter is shown in fig. 3.25. Two mutually incoherent light-waves from TLS_1 and TLS_2 were used to avoid the optical interference effects between the two arms. They are modulated through a MZM by a 40-GHz microwave signal from the network analyzer. The MZM was biased at quadrature for pure intensity modulation during the operation. The wavelengths for TLS_1 and TLS_2 were set to be 1538.8 nm and 1540.0 nm, respectively. After compensating the optical loss ($\sim$10 dB), induced by the MZM, using amplification in an EDFA, the light-waves were sent into a MZ structure.

In the upper (lower) arm of the MZ structure, an optical band-pass filter was used to filter out the optical signal with carrier wavelength of 1538.8 nm (1540.0 nm). After that, the light went through a long SMF and a DMRR-based RF phase shifter (shown in the dashed-line box) in the upper and lower arm, respectively. The optical signal from the DMRR was monitored through an OSA. Then two EDFAs were used to balance the optical powers from the two arms. The EDFA in the lower arm was also used to compensate the fiber-to-fiber coupling loss ($\sim$15 dB) of the tested sample. During the tuning operation, the output power of the EDFA in the lower arm was tuned slightly to compensate for the small RF power variation from the DMRR. The EDFAs can be replaced by simple tunable attenuators if the coupling loss is lowered down to less 2 dB using suitable mode converters [30–32]. Finally, a high-speed PD and the network analyzer were used to extract the response of the microwave signal carried by the optical beam.

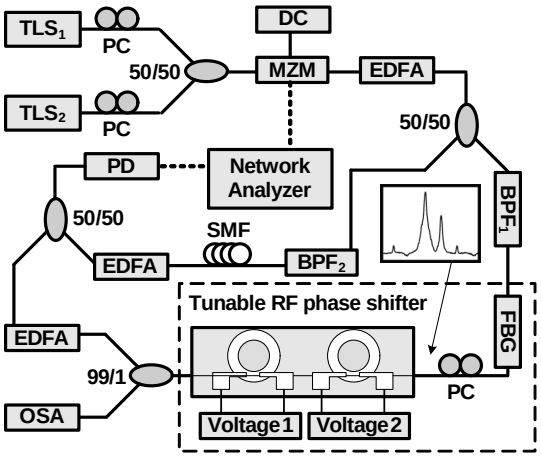

FIGURE 3.25: Experimental setup to implement a tunable microwave photonic notch filter.

In this experiment, we use an low-Q factor DMRR with the coupling gap of 75 nm. Figure 3.26 shows the transmission of the DMRR with different power applied on the micro heater for MRR_1. At the resonance frequency for each MRR, the notch width is $\sim$0.5 nm and the extinction ratio is $\sim$2 dB as shown in the lower black spectrum in fig. 3.26. The

small ripples (∼0.5 dB) are caused by the Fabry-Perot effect due to the reflections at both cleaved facets of the sample. By offsetting the resonances for the two MRRs, the notch for the DMRR can be altered to be broadened, sharpened or split, respectively, as illustrated in fig. 3.26. A notch with large bandwidth and a flat bottom is preferred to achieve a relatively linear phase shifting with low RF power variation for the DMRR as mentioned in the previous subsection. Therefore, we applied 0.5 mW initially on MRR_1 to get a square-like notch of the DMRR before the phase shifting operation.

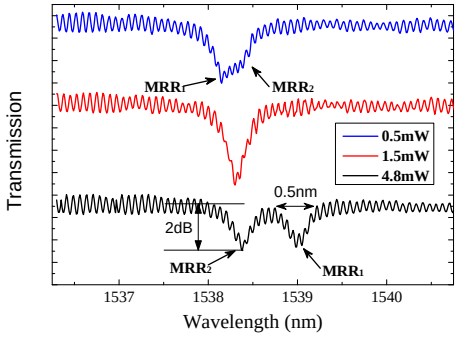

FIGURE 3.26: Transmission spectrum of the DMRR with different electrical power applied to the micro heater for MRR_1.

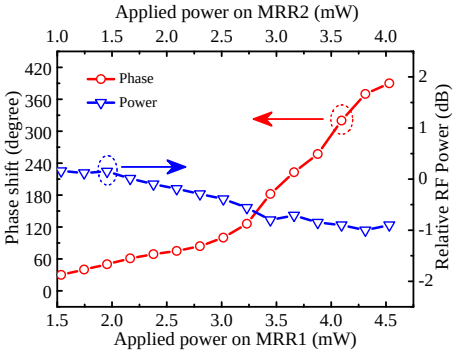

FIGURE 3.27: Measured RF phase shift and RF power variation for the DMRR versus applied power on both micro heaters.

Figure 3.27 shows the measured RF phase shift and the RF power variation as a function of applied power on both micro heaters for the DMRR. A continuous phase shifting range of 0∼380° is obtained while the RF power variation is kept less below 1 dB.

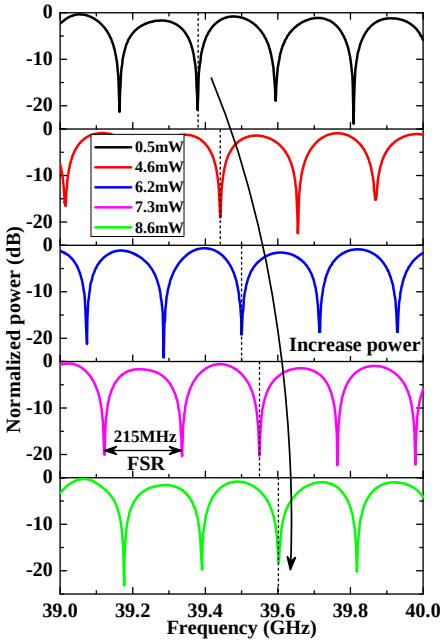

FIGURE 3.28: Tunable RF response of the notch filter achieved by changing the applied electrical power on the DMRR.

Figure 3.28 shows the measured frequency responses around 40 GHz of the proposed microwave notch filter with different electrical powers applied to the DMRR. The FSR of the notch filter is 215 MHz set by the time-delay difference between the two arms of the MZ structure, and the extinction ratio of the notch filter is around 20 dB. As the total electrical power applied on the DMRR increases from 0.5 mW to 8.8 mW, the filter notches shift towards higher frequencies over a full FSR as demonstrated in fig. 3.28. Note that during the tuning of the notch positions, the shape of the frequency response and the FSR was kept unchanged, which can not be realized by tuning the delay line in the other arm of the MZ structure.

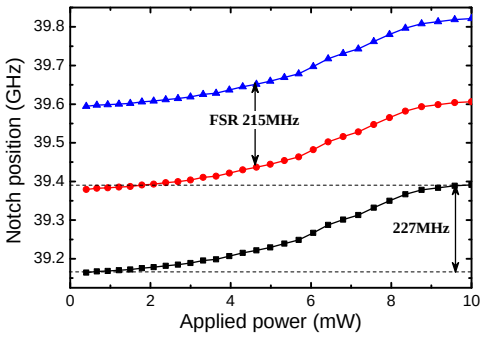

FIGURE 3.29: Measured notch frequency change with different applied power on the DMRR.

Figure 3.29 shows the measured positions of three notches around 39.4 GHz as a function of the total power applied on the DMRR. The notches shift quasi-linearly with the increased applied power and a maximum notch shift of 227 MHz can be obtained when an electrical power of 11mW was applied to the DMRR. The tuning range can be further improved by using a device with a higher Q-factor and thereby a larger phase-shifting range.

3.2 Add/drop type microring resonator

3.2.1 Transfer characteristics

Add/drop type MRR is the most simple ring structure that can be made to extract and reroute a specific wavelength. The schematic drawing of this MRR is illustrated in in fig. 3.30 where the resonator is also coupled to a second waveguide. There are two coupling regions for this type of MRR.

We assume that the amplitude transmission coefficients are t_1 and t_2, the amplitude coupling coefficients are κ_1 and κ_2 for the two coupling regions (the subscripts "1" and "2" refer to the lower and upper coupling regions, respectively). Applying the universal matrix relation to both

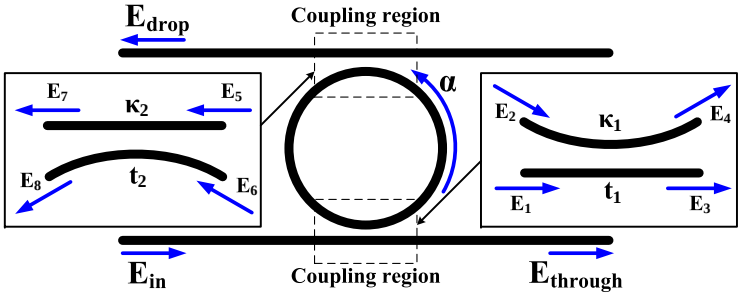

FIGURE 3.30: Schematic of an add/drop type MRR.

coupling regions, we can get the below equations:

$$\begin{bmatrix} E_3 \\ E_4 \end{bmatrix} = \begin{bmatrix} t_1 & \kappa_1 \\ \kappa_1^* & -t_1^* \end{bmatrix} \begin{bmatrix} E_1 \\ E_2 \end{bmatrix} \tag{3.18}$$

$$\begin{bmatrix} E_7 \\ E_8 \end{bmatrix} = \begin{bmatrix} t_2 & \kappa_2 \\ \kappa_2^* & -t_2^* \end{bmatrix} \begin{bmatrix} E_5 \\ E_6 \end{bmatrix} \tag{3.19}$$

Here, we also assume the coupling is lossless:

$$|t_1|^2 + |\kappa_1|^2 = 1 \tag{3.20}$$

$$|t_2|^2 + |\kappa_2|^2 = 1 \tag{3.21}$$

The above equations are supplemented by the circulation condition in the ring:

$$E_2 = E_8 \sqrt{\alpha} e^{i\frac{\theta}{2}} \tag{3.22}$$

$$E_6 = E_4 \sqrt{\alpha} e^{i\frac{\theta}{2}} \tag{3.23}$$

From the eqn 3.18-3.23, we can obtain the transmittance of the complex fields at the through port and the drop port as below:

$$\frac{E_3}{E_1} = \frac{t_1 - \alpha t_2 e^{i\theta}}{1 - \alpha t_1 t_2 e^{i\theta}} \tag{3.24}$$

$$\frac{E_7}{E_1} = \frac{-\alpha^{\frac{1}{2}} k_1 k_2 e^{i\frac{\theta}{2}}}{1 - \alpha t_1 t_2 e^{i\theta}} \tag{3.25}$$

$$\tag{3.26}$$

The transmission at the through port and at the drop port can be then written as:

$$|\frac{E_3}{E_1}|^2 = \frac{\alpha^2 t_2^2 + t_1^2 - 2\alpha t_1 t_2 cos\theta}{1 + \alpha^2 t_1^2 t_1^2 - 2\alpha t_1 t_2 cos\theta} \tag{3.27}$$

$$|\frac{E_7}{E_1}|^2 = \frac{\alpha(1 - t_1^2)(1 - t_2^2)}{1 + \alpha^2 t_1^2 t_2^2 - 2\alpha t_1 t_2 cos\theta} \tag{3.28}$$

The phase shift of the transmitted light can be then de derived as:

$$\phi_T = \pi + \theta + tan^{-1}\frac{t_1 sin\theta}{\alpha t_2 - t_1 cos\theta} + tan^{-1}\frac{\alpha t_1 t_2 sin\theta}{1 - \alpha t_1 t_2 cos\theta} \tag{3.29}$$

$$\phi_D = \pi + \frac{\theta}{2} + tan^{-1}\frac{\alpha t_1 t_2 sin\theta}{1 - \alpha t_1 t_2 cos\theta} \tag{3.30}$$

Figure 3.31 shows the transmission and phase shift at the through port and the drop port of the MRR with different coupling conditions. At the under-coupling condition (see fig. 3.31(a,b)), the effective phase for the through port behaves similar compared with the all-pass MRR and have a less than π phase change while the effective phase for the drop port experiences a monotonically π phase change. At the over-coupling condition (see fig. 3.31(c,d)), although the phase changing trends are the same for both through and drop ports, the effective phase change at the through port is always π larger than that at the drop port. From the point of view of the lower waveguide, the presence of the upper waveguide just modifies the internal gain parameter from α to αt_2 All the expressions given in the previous subsection apply, provided we put $t \to tl$ ($\kappa \to \kappa_1$) and $\alpha \to \alpha t_2$.

For the add/drop type MRR, the output power at the drop port is of

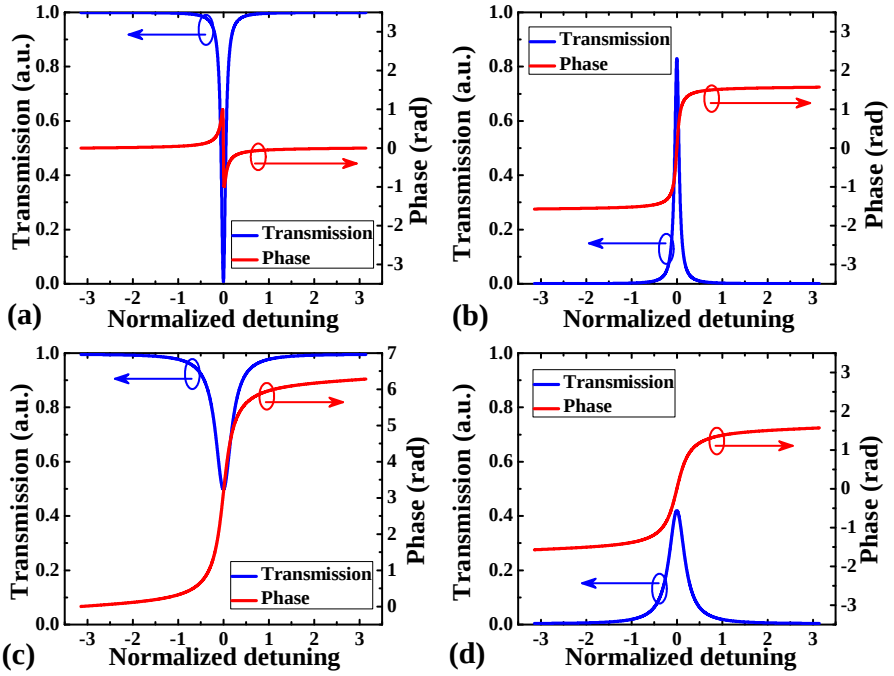

FIGURE 3.31: Transmission and phase shift of the through port (a,c) and drop port (b,d) for the add/drop type MRR under different coupling conditions: (a,b) under-coupling $\kappa^2 = 0.005$, (c,d) over-coupling $\kappa^2 = 0.3$. Here, α^2 and κ_2^2 are always assumed to be 0.99 and 0.005, respectively.

special interest. A full transfer of power from the input port to the drop port is highly desirable for the filtering functionality. At the resonance, the power at the through and drop ports are:

$$|\frac{E_3}{E_1}|^2 = \frac{(\alpha t_2 - t_1)^2}{(1 - \alpha t_1 t_2)^2} \tag{3.31}$$

$$|\frac{E_7}{E_1}|^2 = \frac{\alpha(1 - t_1^2)(1 - t_2^2)}{(1 - \alpha t_1 t_2)^2} \tag{3.32}$$

It is obviously from the eqn 3.32, the full power transfer from the input to the drop port only occurs when the two coupling are identical ($t_1 =$

t_2) and the internal losses can be negligible ($\alpha = 1$). However, it is difficult to be realized in the real world due to the inevitable losses in the microring. Normally, critical coupling condition at the lower coupling region is applied to maximize the output at the drop port which can be easily derived as $\kappa_1^2 = 1 - \alpha^2 + (\alpha\kappa)^2$ from the eqn. 3.31. Therefore, to achieve the critical coupling for the add/drop type MRR, κ_1 should be larger than κ_2.

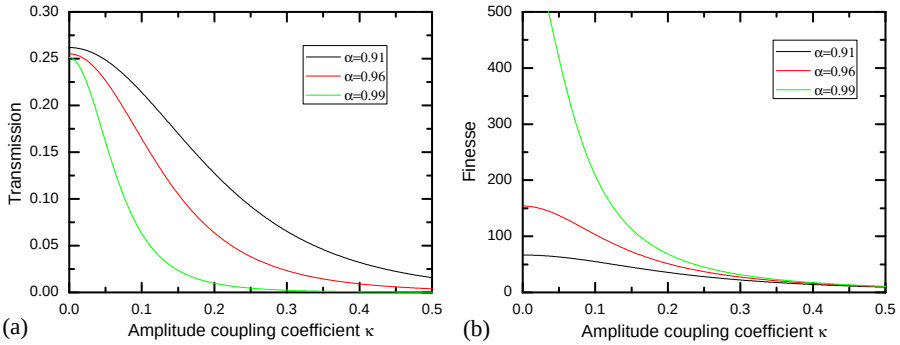

FIGURE 3.32: Transmission at resonance (a) and the finesse (b) as a function of the amplitude coupling coefficient with different round-trip amplitude gains. Here, we assume $\kappa_1 = \kappa_2$.

Figure 3.32 shows the transmission at the resonance (see fig. 3.32(a)) and finesse (see fig. 3.32(b)) as a function of the amplitude coupling coefficient. Here, we assume that the MRR is always in the symmetrical coupling ($\kappa_1 = \kappa_2$). It is seen that as the coupling coefficient increases, the transmission is approaching to zero but do not reach zero. It indicates that a relatively large coupling coefficient is preferred in the symmetrical coupling condition since the precise control the relation between κ_1 and κ_2 to get critical coupling is difficult due to inevitable small geometric variation during the fabrication processes. However, the larger coupling coefficient will always result in an decreased finesse.

Figure 3.33 shows the transmission spectra for two example add/drop-type MRRs both working at the symmetrical coupling condition with different coupling gaps. For the MRR with higher coupling coefficient (260-nm coupling gaps), most of the power can transfer from the input to the drop port which indicates the MRR is close to the critical coupling

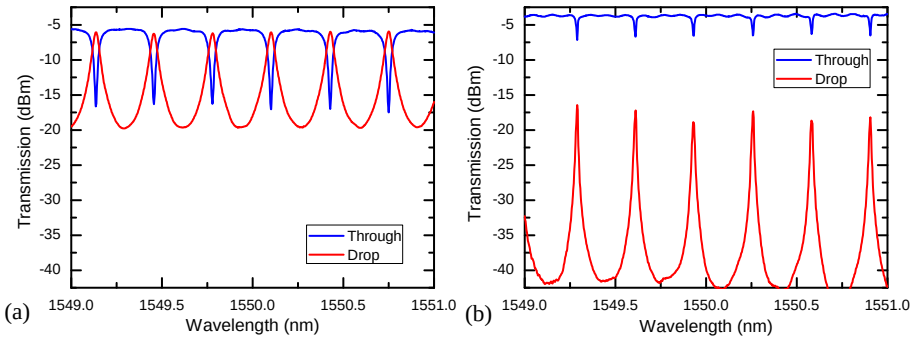

FIGURE 3.33: Measured transmission spectrum of the MRR with different coupling gaps (a) 260 nm and (b) 440 nm. The cross section of the waveguide in the MRR is 420×340 nm^2, the radius of the microring is 250 μm.

condition. While for the MRR with a small coupling coefficient (440-nm coupling gaps), the transmission is much lower than the former one since it is far away from the critical coupling. However, the weak coupling give rise to a high finesse of the MRR which is quite desirable in some applications requiring a high wavelength selectivity (e.g., the pulse repetition rate multiplication (PRRM) that will be discussed in the following subsection).

3.2.2 Pulse repetition rate multiplication

Techniques for generating and processing ultrahigh repetition rate pulse trains have attracted considerable interest for numerous applications including optical time division multiplexing (OTDM) transmission, photonic signal processing, and optical sampling [111, 112]. The generation of periodic pulse trains at repetition rates beyond those achievable by mode locking or direct modulation is very attractive for future ultra high-speed optical communication systems. One alternative is PRRM. The principle of PRRM using spectrally periodic amplitude filters is commonly explained with mode-selection theory: a pulse train with a repetition rate R comprises a series of modes in the frequency domain

which are also periodic with a mode spacing equal to R. If the amplitude of a spectrally periodic filter has a larger mode spacing that is a multiple of R, then the output will have the same increased mode spacing, thereby resulting in an increased repetition rate of the input train. The PRRM has already been realized using other optical filters such as Fabry-Perot filters [113] and fiber Bragg gratings [114]. However, compared with the MRR fabricated in silicon-on-insulator material, these devices are bulky, sensitive to ambient conditions and not suitable for on-chip integration.

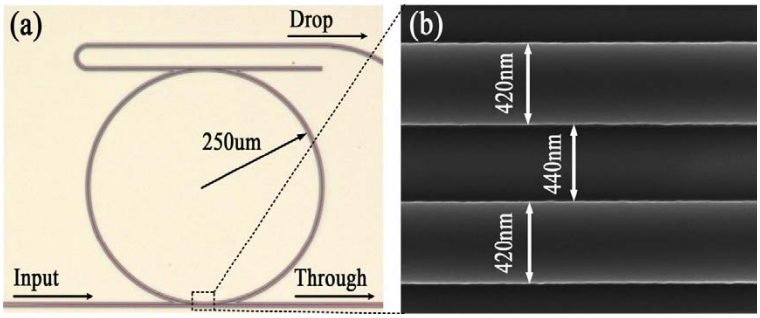

FIGURE 3.34: (a) Optical microscope picture of the fabricated add/-drop type MRR. (b) The SEM picture of the coupling region between the through port and the microring.

In order to obtain PRRM from an optical 10 GHz pulse train to 40 GHz, the MRR is designed to have a FSR of 40 GHz which corresponding to the radius of 250 μm for the MRR as the effective group index of silicon waveguide is ∼4.5. The cross section of the waveguides in the MRR is 420×340 nm^2. The coupling gap for the MRR is designed to be relatively large (440 nm) in order to get high finesse due to the weak coupling. Figure 3.34(b) shows a scanning electron micrograph (SEM) image of the coupling region between the microring and the through port. The fabrication process is mentioned in subsection 3.1.3 but without adding the micro heater.

Figure 3.35 shows the transmission spectrum at the drop port of the MRR. The average FSR of the fabricated MRR is 41.2 GHz. The extinction ratio is ∼27 dB and the 3-dB bandwidth is ∼0.011 nm which corresponds to a quality factor of ∼140,900 at 1550 nm. At resonances,

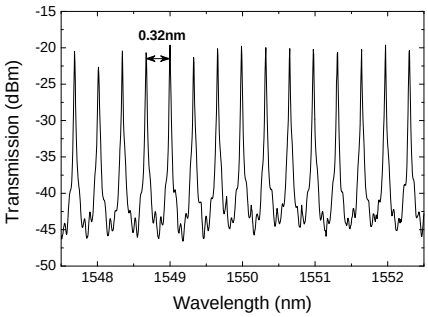

FIGURE 3.35: Transmission spectrum of the MRR used in the PRRM.

the insertion loss of the microring is ∼22.5 dB for the drop port. This includes the loss from the filter and the fiber-to-waveguide coupling losses, which are estimated to ∼7 dB/facet in the setup used. The coupling from fiber-to-chip can be improved by using e.g. nanotapered couplers. The filter loss includes the coupling losses between the waveguides and the ring and the propagation loss ∼0.32 dB/mm for the transverse magnetic (TM) mode. In this way, the round-trip loss of the ring is estimated to be 0.5 dB.

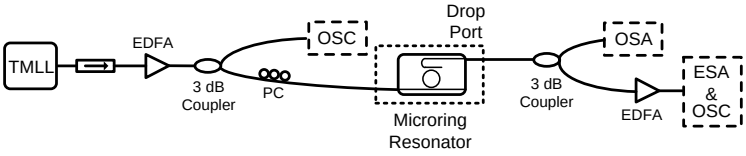

FIGURE 3.36: Experimental setup for PRRM.

The characterization setup is schematically shown in fig. 3.36. The tunable mode-locked laser (TMLL) is used to generate a pulse train at a desired central wavelength from 1480 nm to 1580 nm with a repetition-rate corresponding to one quarter of the FSR of the microring. The output pulse train from the microring is monitored using an optical spectrum analyzer (OSA), an electrical spectrum analyzer (ESA), and an optical sampling oscilloscope (OSC).

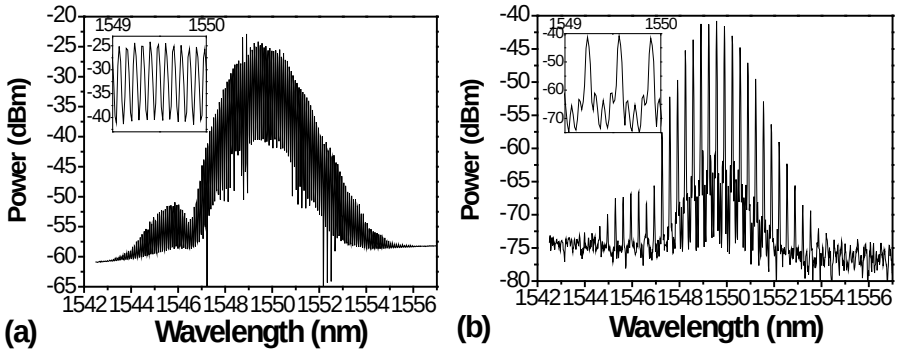

FIGURE 3.37: Optical spectrum of the (a) 10 GHz, and (b) 40 GHz pulse train.

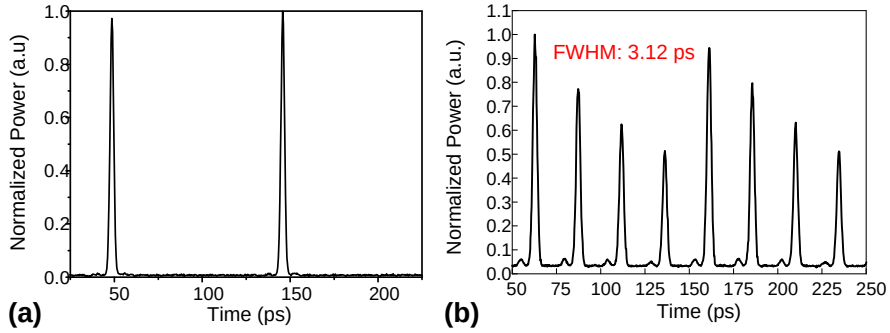

FIGURE 3.38: Temporal traces of the (a) 10 GHz, and (b) 40 GHz pulse train.

Figures 3.37 and 3.38 show the optical spectra and temporal traces of the pulse train before input to and after output from the MRR. A 10.31 GHz pulse train (see fig. 3.38(a)) with central wavelength 1549.6 nm (see fig. 3.37(a)) is sent through the MRR and as shown in fig. 3.38(b) a 41.2 GHz pulse train is obtained. From figs. 3.37(a) and 3.37(b), we can see that most of the phase-locked 40 GHz components in the 10 GHz comb corresponding to the input pulse train are transmitted to the drop port by the MRR. By measuring the electrical power spectrum, it is found that the 40 GHz component is 21.4 dB stronger in amplitude

than the 10 GHz component. The original 10 GHz pulses are 2.27 ps (FWHM). After PRRM to 40 GHz, the pulse width is 2.45 ps which is a broadening of less than 10%. The temporal trace (see fig. 3.38(b)) shows that the 40 GHz pulse train has an amplitude envelope and that the pulses suffer $\sim$1 dB loss per round-trip in the ring. The propagation loss of the ring contributes with a loss of 0.5 dB and the coupling between the ring and waveguides contributes with another 0.5 dB. The variation in pulse amplitudes can be reduced by decreasing the propagation loss by e.g. using a post thermal oxidation in the fabrication process or it can be improved by reducing the coupling between ring and waveguides, but at the expense of increased insertion loss of the filter. We have measured that the microring can tolerate up to 10 MHz mismatch between the input repetition rate and the FSR of the filter. Clean pulse trains are obtained but the pulse width increases to 3.28 ps by detuning the input repetition rate 10 MHz from the optimum match to the FSR. The pulses are broadened due to suboptimum filtering of the 10 GHz modes resulting in a narrowing of the optical spectrum of the pulses.

3.3 Summary

In this chapter, all-pass type MRR structure is introduced and its transfer characteristics are analyzed with different coupling conditions. At the over-coupling condition, the phase properties exhibited in the all-pass type MRR enable its applications in microwave system as a RF phase shifter. As the RF phase shifting operation relies on the resonance tuning, we fabricated MRRs with integrated micro heaters. We first tested the RF phase shifter based on a single MRR, a phase shifting range of $0^\circ \sim 336^\circ$ has been achieved at a microwave frequency of 40 GHz with a high quality (28000) MRR. A smooth phase shift up to $\sim$204° has also been demonstrated with less than 1.3-dB RF power variation using a lower-Q MRR.

However, it is difficult to realize a full 2π phase shift by a single MRR. Moreover, the large power variation during the phase shifting operation in the single MRR scheme hampers its application. To increase the phase tuning range and minimize the power variation, microwave phase

shifter based on DMRR is proposed and demonstrated with excellent performance. A maximum phase-shifting rang of 0∼600° is achieved by utilizing the DMRR. A quasi-linear phase shift of 360° with RF-power variation lower than 2 dB is also demonstrated. An even smaller RF-power variation is also possible if the two MRR are independently tuned carefully. We also implemented the DMRR-based RF phase shifter in a microwave notch filter and demonstrated a full FSR tunability. All the experimental demonstrations shows that the MRR will be potentially utilized in more complicated microwave photonic filter structures and integrated with current optical and electrical communication systems.

In the last part of the chapter, we analyzed another type structure for MRR (add/drop type). Due to its good filtering characteristics, it has been widely used in the optical communication applications. One of these applications, PRRM, has been demonstrated here. A add/drop type MRR which has a 0.32-nm FSR, a Q factor of 140,900 and an extinction ratio of 27 dB, is utilized to generate a 40 GHz pulse train from a 10 GHz input using the spectral selection technique. This make the generation of periodic pulse trains at repetition rates beyond those achievable by mode locking or direct modulation possible.

Chapter 4

Photonic Crystal Components

Photonic Crystals (PhC) are periodic dielectric structures which can forbid the propagation of light within a certain frequency range (known as a photonic bandgap (PBG)). This property provides a new method to control light, and could be incorporated in the design of novel optoelectronic devices. The PhCs can be realized in different ways, one, two, and three dimensions. The 1-D (one-dimensional) PhCs are normally realized in conventional waveguides e.g. fibers or ridge waveguides, and have been already widely used in industry as optical filters. However, complicated functionalities require the periodic structure in two or three dimensions. In this thesis, we will focus on 2-D PhCs since they can be easily fabricated using existing technology and integrated with other optical or optoelectronic devices compared with the 3-D PhCs.

Due to the PBG effect, waveguiding and confinement of light can be realized by introducing line and point defects in the PhC structures, respectively. The line-defect PhC waveguides, bends, and splitters, working as basic elements for routing light in photonic circuit have been well studied and demonstrated. While more efforts have been put into the study of the PhC point-defect cavities since the high nonlinearity induced by the extreme confinement of the optical field in the cavity

makes all-optical signal processing possible in the PhC components. An all-optical tunable dual-mode PhC-based cavity will be introduced in this chapter which has potential for future all-optical switching memory and fundamental logic functions.

Normally, the standard 2-D PhC components are fabricated in silicon material and consist of a triangular or square lattice of circular air holes. In this chapter, we will also investigate a special type of PhCs: ring-shaped photonic crystals (RPhC) which consist of a triangular lattice of ring-shaped holes instead of circular holes. This novel RPhC structure offers some superior properties compared with the standard PhC structures such as a complete bandgap for different polarizations, higher refractive index sensitivity, and large freedom for dispersion engineering. In this chapter, we will discuss the RPhC mainly concerning the latter two properties.

This chapter will begin with some fabrication issues (e.g. the proximity effect, reactive ion etching (RIE) lag effect etc.) related to the patterning of PhC- and RPhC-based components. and then describe the basic theory for PhCs. After that, the modelling and experimental results of the PhC- and RPhC-based components will be discussed, respectively.

4.1 Fabrication of Photonic Crystal Components

Fabrication of all the PhC- and RPhC-based components is performed in the Danchip involving high-resolution lithography and highly anisotropic etching processes. In this section, the fabrication process of PhC components will be presented at first. Then the proximity effect on the defining PhC structures in e-beam lithography and the lag effect on the patterning RPhC structures in reactive-ion etching (RIE) will be discussed.

4.1.1 Process Overview

All the PhC and RPhC components were fabricated in silicon-on-insulator (SOI) materials with a top silicon thickness of 340 nm and a 1-μm buried

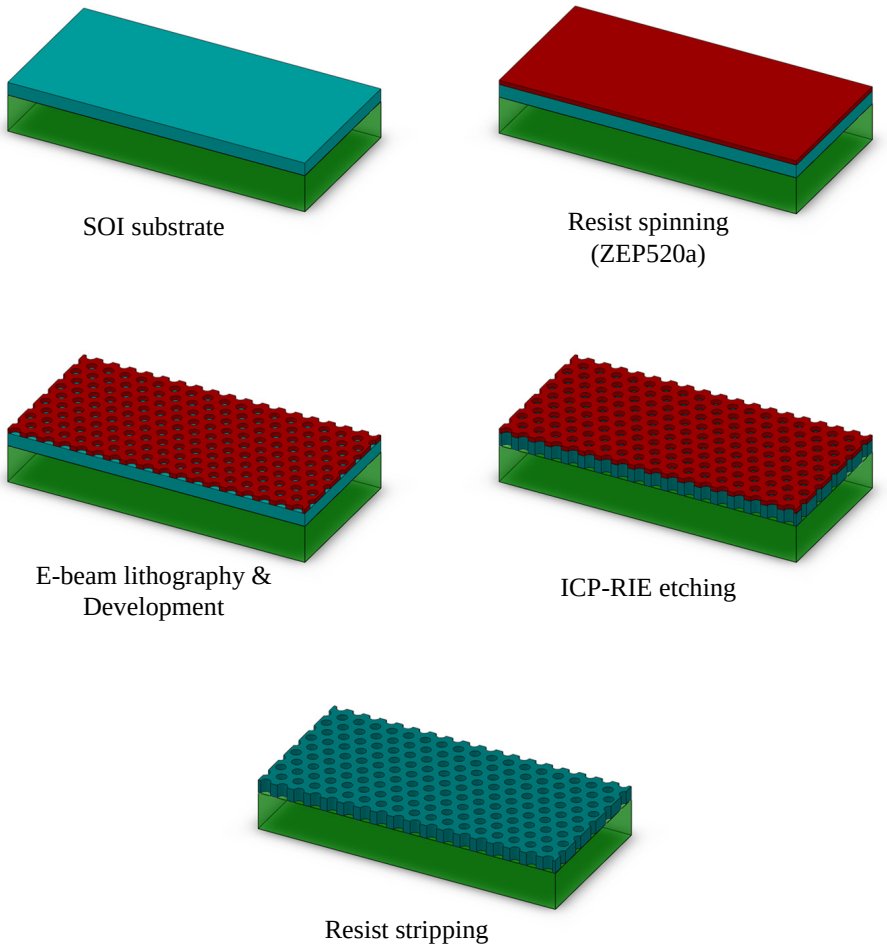

FIGURE 4.1: Schematic overview of the fabrication processes for PhC.

silicon dioxide layer. Figure 4.1 shows the process step by step for a perfect PhC structure patterning. Diluted (1:1 in anisole) electron-beam resist ZEP520A is first spun onto the wafer to create a 110-nm thick masking layer. The PhC pattern is defined in the ZEP520A layer by utilizing electron-beam lithography (JEOL JBX-9300FS). Since ZEP520A is a positive resist, the exposed resist will be removed in developing. After that, the silicon can be etched away utilizing an inductively coupled plasma reactive ion etching (ICP-RIE) process. Finally, the remaining resist is removed by a oxygen sputtering process.

4.1.2 Electron-Beam Parameters

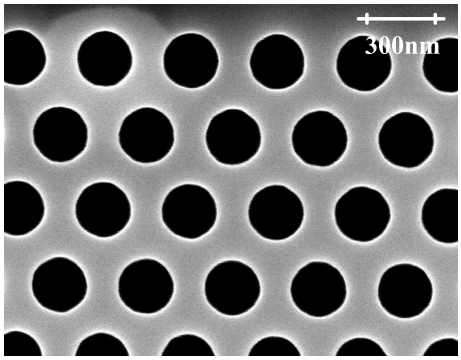

FIGURE 4.2: The SEM picture of the fabricated PhC holes with the electron-beam parameters: 250 μC/cm^2 and 1.36 nA.

For the standard PhC components, a clearance dose of 250 $\mu C/cm^2$ and a current of 1.36 nA were always used in the electron-beam lithography [115]. The fabricated PhC are in a good shape with little side-wall roughness as shown in the scanning electron microscope (SEM) picture in fig. 4.2. However, we will face some problems when patterning the RPhC components using the same parameters, especially for the RPhC with the ring-gap width smaller than 100 nm. Figure 4.3(Left) shows the fabricated ring-shaped holes by using the same parameters in e-beam lithography. It is obvious that the ring-shaped patterns did not receive enough exposure due to the relatively large electron-beam size and the low dose. Therefore, an increased dose together with a decreased current

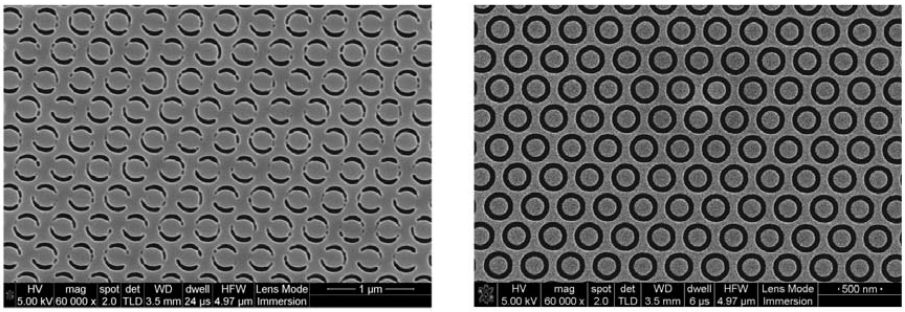

FIGURE 4.3: The SEM pictures of the ring-shaped holes fabricated with different parameters in e-beam: (a) 250 $\mu C/cm^2$ and 1.36 nA, (b)350 $\mu C/cm^2$ and 0.6 nA.

(smaller electron-beam size) is neccessary in patterning the ring-shaped holes. Figure 4.3(Right) shows the fabricated ring-shaped holes with the optimized parameters for the e-beam lithography: current and dose are the 0.6 nA and 350 $\mu C/cm^2$, respectively.

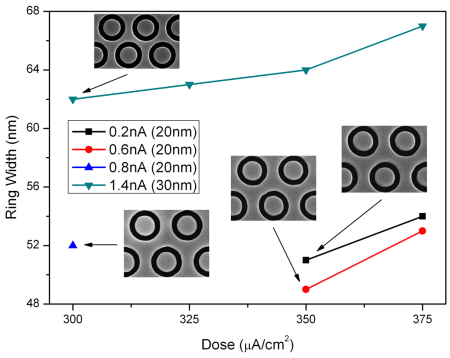

FIGURE 4.4: Smallest ring-gap widths realized in e-beam lithography with different parameters.

However, using such a small current will make the exposure extremely time-consuming which has been proved not necessary after all. Several combination of current and dose were tested then in the e-beam lithography for patterning the RPhC structures as shown in fig. 4.4. It is clear that by using the large current 1.4 nA, the smallest ring gap we

can fabricated is only 60 nm while ∼50 nm ring gap can be fabricated utilizing 0.8 nA and 300 $\mu C/cm^2$.

4.1.3 Proximity Correction

The proximity effect in electron beam lithography is a phenomenon that a uniform exposure by the incident beam can result in a nonuniform distribution of actual received exposure intensity in the resist [116]. Typically, the pattern with low exposure density receives less exposure than the pattern with higher exposure density.

In defining PhC structures, the size of the holes will be different if the surrounding exposure density is different. This is due to the forward-scattering effect and backward-scattering effect. The forward-scattering is introduced when the electrons scatter down into the resist while the backward-scattering is introduced when the electrons bounce back and forth in the resist and the substrate. The total exposure intensity distribution in the resist caused by the two scatterings is approximated by the sum of two Gaussian-functions [117]:

$$f(r) = \frac{1}{\pi(1+\eta)}\left(\frac{1}{\alpha^2}exp(-\frac{r^2}{\alpha^2}) + \frac{\eta}{\beta^2}exp(-\frac{r^2}{\beta^2})\right) \tag{4.1}$$

where r denotes the radial distance and α, β, and η are the width of the broadened exposure beam, the radius of the backward-scattering range, and the ratio between the exposure coming from the forward and backward scattering electrons. These proximity parameters are related to the electron beam energy and diameter, the resist material and thickness. The proximity parameters can be calculated by using e.g. a Monte Carlo simulator for specific writing conditions. In the Danchip cleanroom, the parameters α=0.0125 μm, β=34.12 μm, and η=0.521 were used for the SOI slab configuration [115]. In a high accelerating voltage system like the 100 kV e-beam system in Danchip, the backward scattering effect is much more serious than the forward scattering and the backward scattering radial range is 34 μm from the incident point.

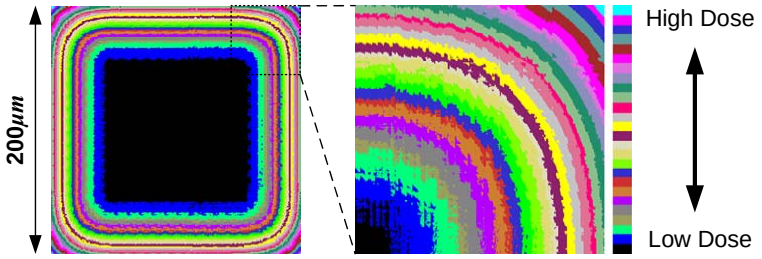

FIGURE 4.5: (Left)Proximity corrected dose distribution for a square area exposure PhC structure. (Right) Zoomed view of the dose distribution of the pattern.

For patterning a large exposure area such as a 200×200 μm^2 of PhC as shown in fig. 4.5, the center part will be over exposed compared to the edge parts which causes the hole size to be different in these areas. As the PhC properties depend on the hole size uniformity, a high accuracy and homogeneity has to be achieved regarding size, shape and position of the holes [118]. These requirements make proximity correction important for electron-beam patterning of PhC structures. In order to make uniform exposure over the whole pattern, different electron exposure doses could be applied in different areas according to the energy distribution as shown in fig. 4.5. After the proximity correction, the electron exposure dose for edge parts of the pattern will increase accordingly while the dose for center part decreases.

To test the influence of proximity effects in electron-beam lithography for defining the PhC components, a series of standard PhC waveguides with different surrounding pattern densities were fabricated. Figures 4.6(a) and (b) show the design patterns for two of those waveguides. The surrounding density difference is realized by defining the different trench widths for the access waveguides. For the PhC waveguides with larger exposure density, the holes in the PhC waveguide will be over exposed to some extent compared with those with small exposure density due to the electron backward-scattering from the trench area. And this will make the diameter of the holes of the PhC increase. Figures 4.6(c) and (d) show the SEM pictures of the fabricated PhC waveguides with 2-μm and 10-μm width trench, respectively. Figures 4.6(e) and (f) show the

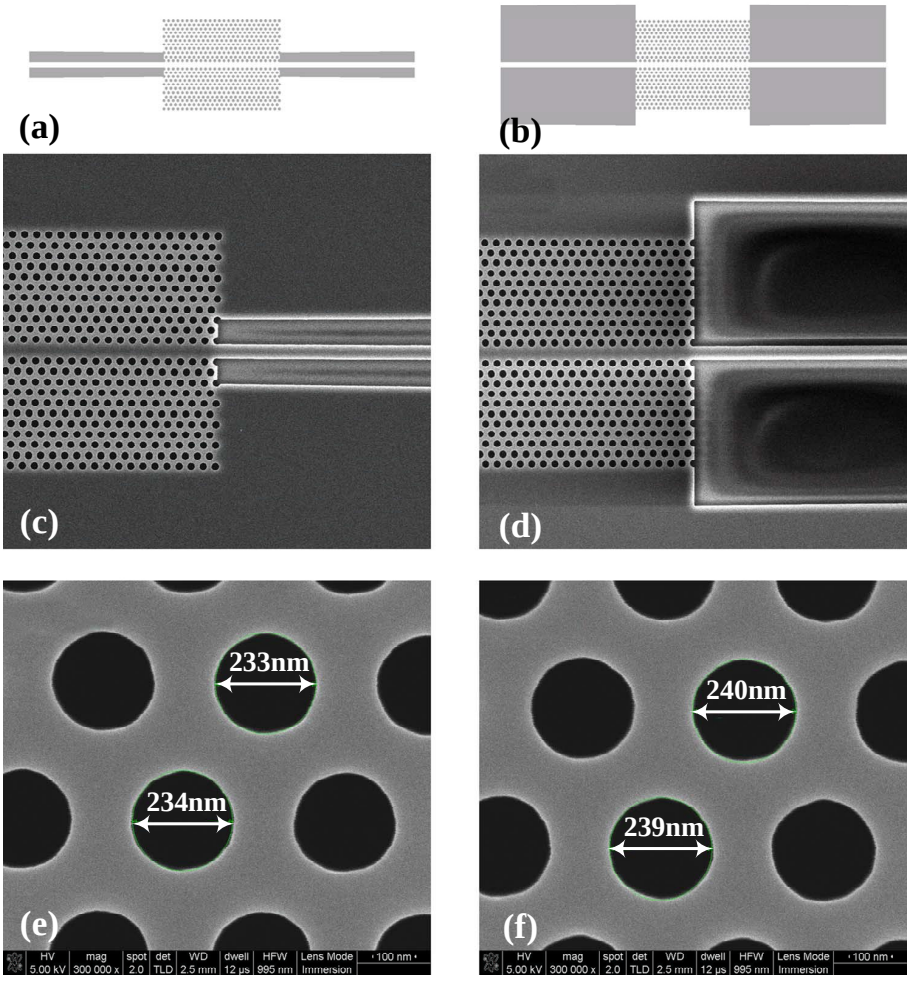

FIGURE 4.6: (a,b)Design patterns for PhC waveguides with different trench widths. (c,d) The SEM pictures of fabricated PhC waveguides. (e,f) Zoomed SEM pictures for the holes in PhC waveguides.

zoomed SEM pictures for the holes in these structures. It is found that the hole diameter of the PhC waveguide with 10-μm trench width is ~240 nm (see fig. 4.6(f)) which is around 6 nm larger than that of PhC waveguide with 2-μm trench width. And this hole diameter difference will also lead to different performances for the PhC waveguide. The detail transmission measurement results for these proximity test PhC waveguides will be discussed in section 4.3.2.

Above all, it is always necessary to taking proper consideration of the proximity effect in electron-beam lithography when defining the PhC structures. The proximity correction should be employed to reduce the effect especially for defining large photonic circuits with different exposure density.

4.1.4 Reactive-Ion Etching Lag Effect

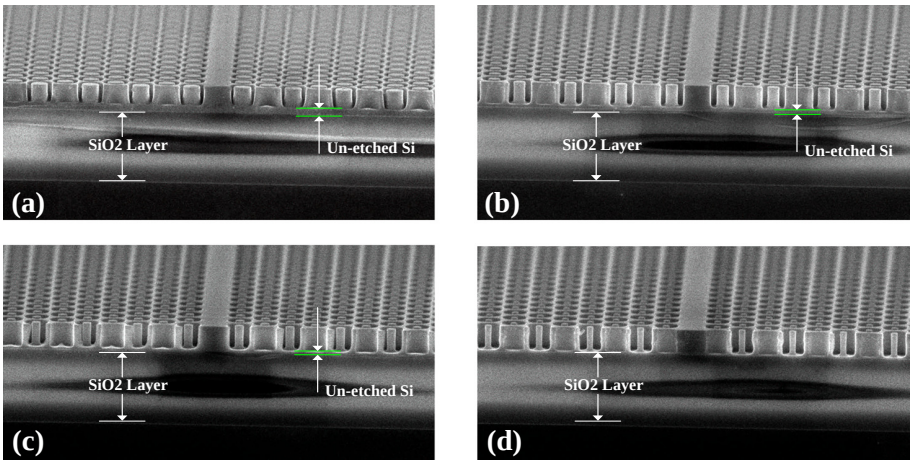

FIGURE 4.7: The SEM side-view pictures for the fabricated RPhC waveguides with different ring gap widths after the same etching process. Ring-gap width: (a) 52 nm. (b) 82 nm. (c) 110 nm. (d) 120 nm.

The RIE lag effect is a phenomenon that the etching rate is dependent on the pattern openings [119]. According to different aspect ratio of the structure, the etching rate will appear differently. For the standard

PhC etching in SOI wafer, the typical aspect ratio is around 1.5. The lag effect is not clear and no special attention is necessary to be paid. However, the lag effect become severe when the aspect ratio is larger than 3 e.g. for the RPhC structures.

Figure 4.7 shows the SEM side-view pictures of the fabricated RPhC structures with different ring gap widths at the same etching process. In this process, we use the standard etching recipe which includes 8 etch cycles. However, not all the ring-shaped holes in the structure were etched with the same depth. It is obvious that the etch depth of the ring-shaped holes with 52-*nm* ring-gap width is much smaller than those with larger ring-gap widths.

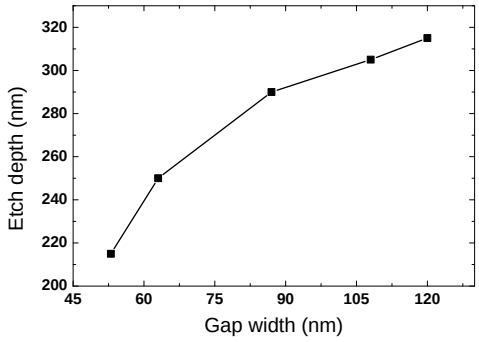

FIGURE 4.8: Measured etch depth with different ring-gap widths for the fabricated RPhC structure. (b) The simulated sensitivity for the RPhC with different etch depthes.

Figure 4.8 shows the measured etch depths of the ring-shaped hole with different ring-gap widths. There is a ∼100-*nm* depth difference between the narrow gap structure and the wide gap structure. The depth difference will result in severe problems concerning the components' performances.

For those structures without etching through the silicon layer, the effective index of PhC will increase and make the cut-off wavelength red-shift. In addition, for the RPhC waveguide, the light field will concentrate more in the un-etched silicon which leads to a degraded performance for

some application such as index sensing which will be discussed more in the section 4.4.2.

The lag effect can be reduced to some extent by using such as increase the passivation material or changing the recipe parameters. However, those methods can only be applied to one specific patterning. And etch development of the recipe is time-consuming. No optimization of the recipe concerning about lag effect is performed.

Over-etching could be one simple way to make sure that all the silicon be etched through. However, the over-etching also gives rise to another problem. As the etching time increases, the sidewall etching will also make the ring gap width increases. Typically, each extra etching cycle will give a extra 5-nm width increment for the ring-gap width. Since the RPhC component is always sensitive to the hole size and the ring-gap width, the unexpected size increment will have severe influence on the components' performance. Therefore, it is necessary to take into account the size increment when performing the over-etching to solve the lag effect-induced problem.

4.2 Theory of Photonic Crystals

The light propagation in PhCs can also be described by macroscopic Maxwell equations as described in section 2.1. By solving the eqs. (2.9),(2.10), we can find how the electromagnetic waves behave in the medium providing the dielectric constant $\varepsilon{=}\varepsilon(\mathbf{r})$ of the structure of interest is given. There are several numerical techniques that can be utilized to solve the equation such as plane-wave expansion method [120], and the finite-difference time-domain (FDTD) methods [121].

In the plane-wave expansion method, $\mathbf{E}$ and $\mathbf{H}$ are assumed to be harmonically varying in time t at an angular frequency ω. The electric and magnetic fields then can be expressed as the product of a spatial- and time-varying function as below [122]:

$$\mathbf{H}(\mathbf{r},t) = \mathbf{H}(\mathbf{r})e^{i\omega t} \tag{4.2}$$

$$\mathbf{E}(\mathbf{r},t) = \mathbf{E}(\mathbf{r})e^{i\omega t} \tag{4.3}$$

where $e^{i\omega t}$ describes the harmonic variation of the fields in time t. Using the eq. (4.2-4.3), the propagation of electromagnetic waves can be described in a single wave equation, the master equation, expressed by the magnetic field alone:

$$\nabla \times [\frac{1}{\varepsilon(\mathbf{r})} \nabla \times \mathbf{H}(\mathbf{r})] = (\frac{\omega}{c})^2 \mathbf{H}(\mathbf{r}) \tag{4.4}$$

where $c=\frac{1}{\sqrt{\varepsilon_0 \mu_0}}$ is the speed of light in vacuum. Due to the discrete translational symmetry of the PhC, $\varepsilon_r(\mathbf{r})=\varepsilon_r(\mathbf{r}+\mathbf{R})$ ($\mathbf{R}$ is the lattice vector), Bloch's theorem [122], which states that a solution to the master equation may be expressed as a plane wave modulated by a function having the same periodicity as the PhC, can be applied to solve the master equation for a PhC with a spatially varying dielectric function $\varepsilon_r(\mathbf{r})$. Then all the calculation can be performed in the frequency domain in the so-called reciprocal space (k-space), which is a Fourier transform of the real space, whereby solutions formed by combinations of plane-waves can be described as Fourier expansion series, which make calculations less cumbersome. In this way, solutions ω to the master equation (eq. (4.4)) will be functions of the wavevector k.

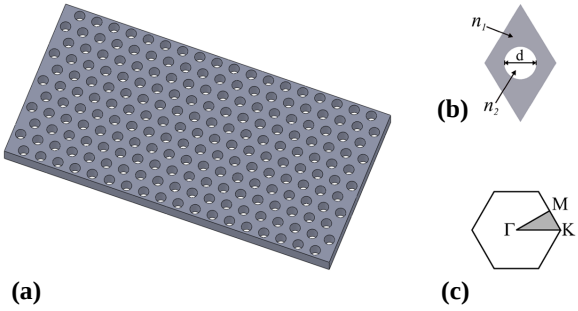

FIGURE 4.9: (a) Schematic of a typical perfect PhC. (b) Unit cell in real space with a hole with refractive index n_2 placed in a dielectric material with refractive index n_1. (c) The unit cell in k-space and the irreducible Brillouin-zone.

Figure 4.9(a) shows a typical perfect PhC which consists of a triangular

lattice of circular holes. In the calculation, the structure can be described using just a single unit cell as shown in fig. 4.9(b), which can be repeated infinitely to create an infinite periodic structure of circular holes with refractive index n_2 placed in a triangular lattice in the material with refractive index n_1. The modal field distribution and the dispersion relation $\omega(\mathrm{k})$ of the optical modes supported by the structure can easily be analyzed by applying the plane-wave expansion method to the single unit cell. Normally, the solutions are calculated along the high-symmetry directions spanning the points Γ,**M**, and **K** in k-space of the irreducible Brillouin-zone as shown in gray region in fig. 4.9(c).

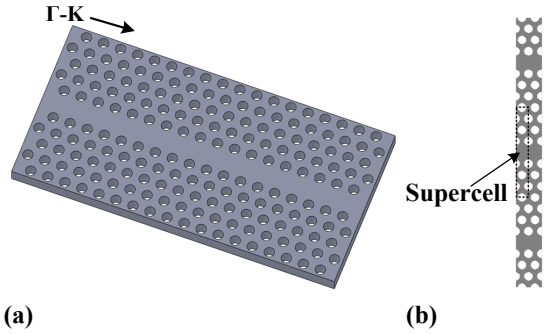

FIGURE 4.10: (a) Schematic drawing of a line-defect PhC waveguide. (b) The schematic structure produced by repeating the supercell in two orthogonal directions for band diagram calculation.

By just analyzing the single unit cell, however, we can not get the information for the guided modes in a line-defect PhC waveguide which is formed by omitting one row of the holes as shown in fig. 4.10(a). A so-called super-cell approximation can be adopted to find the solutions for the PhC with defects. In this approximation, a supercell is defined by **M**×**N** repeated unit cells with the defect. The supercell is repeated infinitely in two orthogonal directions as shown in fig. 4.10(b) and the solutions to the master equation are calculated along the line-defect direction (Γ-**K** direction of the supercell in k-space as shown in fig. 4.10(a). In this way, the line-defect PhC waveguide is approximated by the structure with repeated line-defect waveguides. To get the accurate and converged results in the calculation, the supercell should be large enough to avoid the coupling between the repeated waveguides,

whereby the solutions do not affect each other. Typically, a supercell of size 1×11 is used for calculating the guided modes in PhC waveguide [115].

The software used for dispersion relation calculation for PhCs is the free software "MIT Photonic-Bands" (MPB) [120]. MPB is a full-vectorial eigenmode solver of Maxwell's equations and computes the eigenmodes with periodic boundary conditions by utilizing a preconditioned conjugate-gradient minimization of the block Rayleigh quotient in a plane wave basis. All the band diagrams shown in the following subsection are calculated by MPB.

To study the electromagnetic waves in PhCs, only knowing which frequencies that are allowed in the PhC structures is not enough, knowing how the electromagnetic waves propagate is also very important. The FDTD method then can be used to study the electromagnetic wave propagation in time domain. The details about the FDTD methods will not be covered here but can be found in ref. [121]. The software used in this thesis for FDTD calculation is a commercial software tool CrystalWave, which was developed by the company Photon Design. The software is based on the ONYX2 version of the FDTD algorithm by A. Ward and J. Pendry [123] as the basic FORTRAN code. Improvements have been made to the code by employing newly developed perfect matching layer (PML) boundary conditions by A. Lavrinenko [124]. All the transmission simulation presented in the following subsection were performed using this software.

4.3 Standard Photonic Crystal Structures

The two-dimensional PhC structures studied in this thesis are all fabricated in silicon material at the top layer of SOI wafers as shown in fig. 4.11. The SOI wafer have a top silicon layer of 340-nm thickness with the refractive index of 3.476, a 1-μm thick silicon dioxide buffer layer with refractive index of 1.528, and a thick silicon substrate which is always larger than 500 μm. Typically, the radius of the holes R is around 120 nm and the lattice constant Λ is around 400 nm. The two

parameters can be adjusted according to the needed functionality or the operational wavelength range of the PhC components. In the MPB and Crystalwave calculation, unless otherwise stated, all the parameters are chosen according to the above SOI configuration and dimensions.

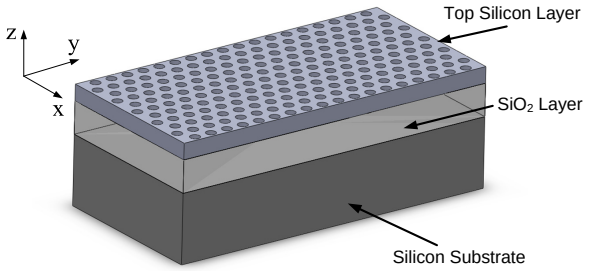

FIGURE 4.11: (a) Schematic drawing of PhC in a typical SOI slab configuration.

In the calculations, all the solutions to the master equation (eq. 4.4) can be separated into two distinct polarizations. One is transverse-electric (TE) modes which have the magnetic field perpendicular to the xy-plane and the electric filed **E** in the xy-plane. Another is transverse-magnetic (TM) modes which have the electric field perpendicular to the xy-plane and magnetic field **H** in the plane. The dispersion relation (band structures) for TE and TM modes are always different.

4.3.1 Perfect Infinite Photonic Crystal

Figure 4.12 shows the dispersion relation calculated for the TE (red) and TM (blue) polarizations along the symmetry directions Γ-, M-, K for a perfect infinite 2-D structure with a hole radius R=0.4Λ. One can find that a large band gap exists in the normalized frequency from 0.25-0.41 for the TE-polarization wherein no optical modes exist. However, there is no such a band gap for the TM polarization. This PhC does not have a complete omnidirectional band gap in any frequencey range. Nevertheless, a PhC structure with a PBG for TM mode is possible to make by using dielectric columns in air instead of the air holes in the dielectric material [122]. In this thesis, we focus our study on the PhC

structures with air holes since the fabrication and the confinement of light in the line-defect waveguide for the hole-type PhC is much easier than the column-type PhC. Therefore, all the calculations and measurements in the remaining of this thesis are, if nothing else is mentioned, for the TE-polarization light due to its PBG in hole-type PhC structures.

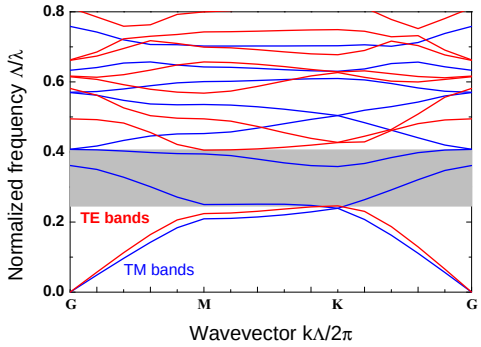

FIGURE 4.12: 2D band diagram for both TE (red) and TM (blue) polarizations for a perfect PhC with $\boldsymbol{R}/\Lambda$=0.4. The gray region is the PBG for the TE mode.

4.3.2 Line-Defect Photonic Crystal Waveguide

For a standard line-defect PhC waveguide as shown in fig. 4.10, the light could be confined in-plane due to the mentioned PBG effect and confined out-of-plane due to the total internal reflection (TIR) caused by the high refractive index contrast between silicon and air or silica.

Figure 4.13 shows a 2-D calculated band diagram and transmission of the PhC waveguide by using MPB (Left) and CrystalWave (Right), respectively. The gray regions in the band diagram represent the slab modes which can also exist in a perfect PhC structure. Other bands are due to the introduction of the line-defect. The blue and red bands stand for the odd and even modes[1], respectively. The waveguide modes are denoted by the solid curves located in band gap which is between the two gray

[1]Even (odd) modes have the symmetrical (asymmetrical) field distribution through a plane parallel to the Γ-M direction at the center of waveguide core.

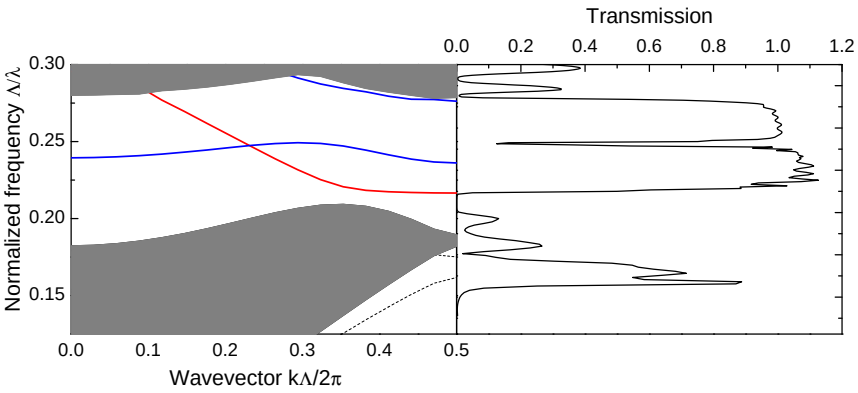

FIGURE 4.13: (Left) 2D band diagram for the TE-polarization for a line-defect PhC waveguide. ε=13 and R/Λ=0.3 were used in the calculation. The gray regions are slab bands. (Right) 2D FDTD simulated transmission for the PhC waveguide with 10 μm length.

regions. Among those waveguide modes, the most interesting one could be the lowest even mode (known as the fundamental waveguide mode denoted by the red curve in fig. 4.13) which has the largest bandwidth within the PBG. In addition, this mode is sometimes the only one that locate below the silica light line[2] and then can be guided with no loss theoretically. For the SOI configuration, those modes located above the silica light line can easily penetrate into the silica cladding and then introduce large loss. Therefore, we will mainly focus on this waveguide even mode in the the following calculated band diagram. Due to the waveguide modes, the light within the PBG can be transmitted along the line-defect direction in the PhC waveguide. From the CrystalWave simulation, we can find that the waveguide has a cut-off frequency at Λ/λ=0.22 which is determined by the bottom position of the waveguide mode shown in the band diagram.

Fig. 4.14 shows the SEM pictures of a typical PhC waveguide. The waveguide is fabricated on the SOI wafer with 340-nm silicon layer as mentioned before. Proximity correction is applied to the sample in order to get a uniform hole size. The diameter of holes and the lattice constant

[2]Silica light line is defined by $\frac{\omega}{c}=\frac{k}{n_{SiO_2}}$.

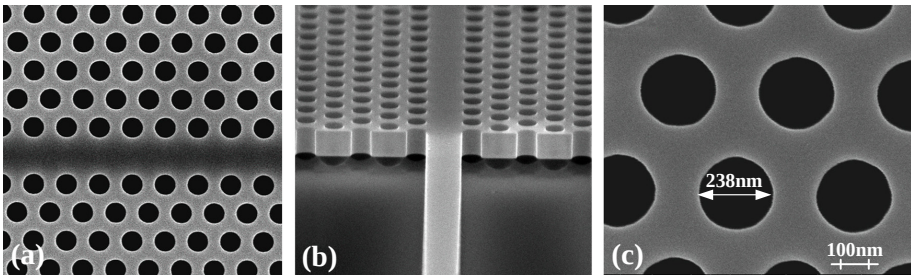

FIGURE 4.14: Scanning electron micrograph pictures of (a) the standard PhC waveguide (R/Λ=0.3105, and Λ=380 *nm*),(b)the connection region between ridge waveguide and the PhC waveguide and (c) the zoomed-in holes of the PhC waveguide.

are 238 *nm* and 380 *nm*, respectively as illustrated in fig. 4.28(c) and the waveguide length is 20 μm. All the fabricated PhC components are butt-coupled to the silicon ridge waveguides with around 500-*nm* widths. The ridge waveguides are tapered to 4 μm at both ends of the samples to enhance the coupling efficiency. In this way, the waveguides can be characterized using the experimental setup mentioned previously in Chapter 2.

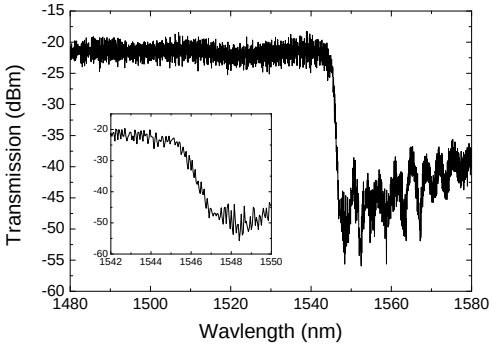

FIGURE 4.15: Measured transmission spectrum of the standard PhC waveguide. (Proximity correction is applied in the electron-beam lithography.)

Figure 4.15 shows the measured transmission of the PhC waveguide. There is a large coupling loss between the tapered fiber and the ridge

waveguide of about 20 dB. In the measurement, the tunable laser source (TLS) was sweeping from 1480 nm to 1580 nm which is just in the PBG for the PhC structure in interest. It is seen that the light with the wavelength smaller than 1556 nm can be transmitted through the waveguide. But the transmission drops 30 dB within 2 nm (1545∼1547 nm), as shown in the inset of the fig. 4.29. This steep drop in the transmission is due to the cut-off of the waveguide mode frequency at around 0.245 which is corresponding to the wavelength 1546 nm.

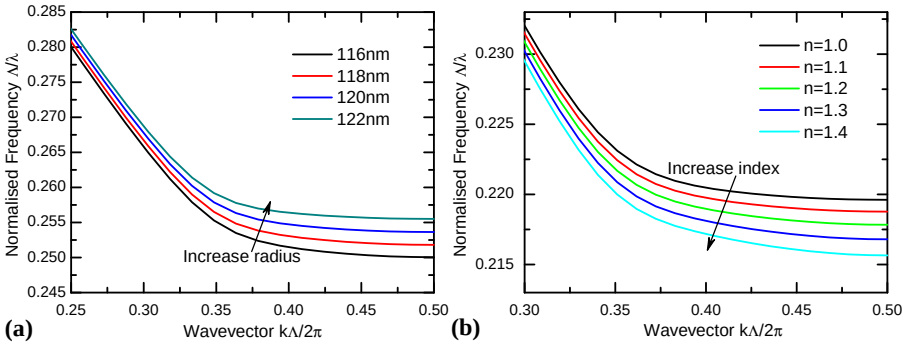

FIGURE 4.16: The fundamental waveguide mode change with different hole radius (a) and refractive index (b).

The fundamental waveguide mode may be influenced by many factors such as hole radius, waveguide width[3], and ambient index[4]. Fig. 4.16(a) shows the fundamental waveguide mode for the PhC waveguide with different hole radii. It is shown that the fundamental waveguide mode moves to higher frequencies as the radius of the hole increases. The waveguide mode is so sensitive that only 2-nm increment of the hole radius results in a cut-off frequency shift from 0.25 to 0.2555 which corresponds to a 12-nm cut-off wavelength shift providing the lattice constant is 380 nm. Therefore, it is important that the fabricated hole diameters are well controlled to insure the cut-off frequency of the waveguide is in the right position. Normally, the fabricated holes will become a little

[3]The width of the PhC waveguide is defined as the center-to-center distance between the holes adjacent to the waveguide core.

[4]The ambient index: the refractive index of the medium at the surrounding of the PhC structure including the medium in the holes.

larger than the design pattern in the e-beam lithography which make the cut-off frequencies move to the higher frequencies. It is necessary to take this into account in the design for PhC structures.

Besides, the radius of holes will also be changed due to the pattern density in the fabrication process induced by the proximity effect in the e-beam lithography. Figure 4.17(a) shows the measured transmission of the proximity test PhC waveguides as mentioned in the previous section 4.1.3 with different exposure density without any proximity correction. It is seen that the cut-off wavelength for the PhC waveguide with high exposure density (10-μm wide trench) is 1548 nm while the cut-off wavelength for the PhC waveguide with low exposure density (2-μm wide trench) is 1560 nm. There is a 12-nm cut-off wavelength variation for the fabricated waveguides which agrees well with the simulation.

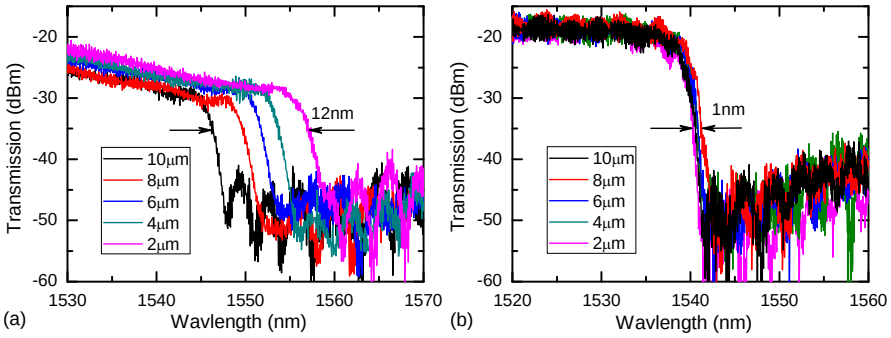

FIGURE 4.17: Measured transmission for the PhC waveguides with different trench width for the access ridge waveguide without (a) and with (b) performing proximity correction in e-beam lithography.

Since the PhC waveguide performance is very sensitive to the surrounding exposure density, proximity correction is necessary to make the PhC waveguides with the same characteristics. We also tested the same structures by performing proximity correction. Figure 4.17(b) shows the measured transmission results for the PhC waveguide with different trench widths after proximity correction. The cut-off wavelength variation is reduced from 12 nm to 1 nm for different waveguides. Besides, it is clear that the transmissions for the proximity corrected waveguide have

a much steeper intensity drop at the cut-off wavelength than those without the correction due to the uniform holes size.

Ambient index is also a factor that influences the fundamental waveguide mode. Figure 4.16(b) shows the movement of the waveguide mode with different ambient index which indicate the mode is also sensitive to change of the background refractive index. Therefore, we could monitor the change of the cut-off wavelength shift in order to know the refractive index change of the surroundings and then realize an index sensing application. This sensing application has already been demonstrated in [125] However, the sensitivity of the PhC waveguide components can be further increased by using RPhC waveguide which will be discussed in the section 4.4.2.

From the analysis of the fundamental modes in the band diagram, we do not only get the information about the cut-off frequency, we can also find the group velocity V_g in which the light propagate through the waveguide at different frequencies. The group velocity V_g and the group index n_g can be calculated by the below equations:

$$V_g = \frac{\partial \omega}{\partial k} \tag{4.5}$$

$$n_g = \frac{c}{V_g} \tag{4.6}$$

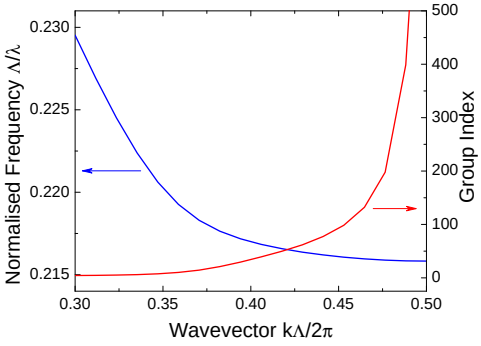

FIGURE 4.18: The fundamental PBG band (red) and the group index (blue) as a function of wavevector

Figure 4.18 shows the calculated fundamental mode and the group index for a PhC waveguide with R/Λ=0.3. It is clear that the group index of the light will increase significantly as the light frequency is approaching the cut-off frequency. Therefore, the light at a frequency close to the cut-off frequency can only propagate through the waveguide within a extremely slow speed or even close to zero. This is so-called slow-light phenomenon. Since the light-matter interaction can be increased with the decreasing group velocity [126–129], the slow light can be used for enhancing various nonlinear effects in the optical waveguide [130]. The slow-light phenomenon also could be used for other relevant applications including e.g. optical buffering [131], switching [132], lasing [133] and dispersion control [134, 135] in nanophotonic circuits. However, there are two major fundamental limitations for use of the slow light in PhC waveguides. Firstly, the slow light in PhC waveguide has a very limited bandwidth. Since the group velocity is proportional to the slope of the waveguide fundamental mode, the slow light phenomenon only appears in a very narrow frequency range. It is by nature difficult to get a large group index over large frequency range. However, we could get a moderately large group index over a relative large frequency range if the fundamental band curve could be somehow tailored. Various techniques have been demonstrated [136–138] for the dispersion engineering to make the slow-light more practical in applications. Some similar dispersion engineering could be also realized by using perturbed RPhC waveguide which will be discussed in section 4.4.4. Another limitation for the slow-light application is the coupling between the PhC waveguide and the ridge waveguide due to the large mode mismatch [139–142]. However, the interface between these two waveguides can be tailored to optimize the coupling efficiency. In section 4.4.3, the topology optimization method [143, 144] will be used to make the slow-light coupler for RPhC waveguide.

4.3.3 Dual-Mode L3 Photonic Crystal Cavity

The PhC waveguide is one of the important elements in the photonic circuit. The PhC cavity is another important element in the photonic circuit due to its many applications in ultra-small filters [66, 145–147], sensors [67], low-threshold lasers [68], single-photon emitters [69], optical-buffer memories [70], optical switching [71, 72], and optical transistors [73]. Instead of removing a row of the holes, the cavity can be formed by removing one or a few holes in the PhC structure.

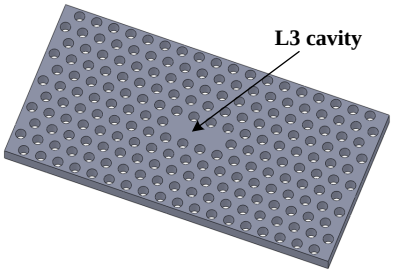

FIGURE 4.19: The schematic drawing of a L3 PhC cavity.

Figure 4.19 shows a typical L3 cavity which is formed by removing three holes in the triangular lattice. A high-Q cavity can be achieved by shifting the positions of the holes adjacent to the cavity [148]. Since the lattice constant for PhCs is in the sub-wavelength scale, an ultra-small PhC cavity with high Q factor can be realized in this way. This ultra-small cavity is highly desirable in the applications for all-optical switching, memories, flip-flop and opitcal transistors. For those applications, photonic devices always face a problem that the operation energy or switching energy is very large. However, the operation energy can be largely decreased by using ultra-small volume cavity with ultra-high Q factor (e.g. the PhC L3 cavities) due to the strong light confinement and the enhanced light-matter interaction.

In 2005, a transistor operation in optical domain has been demonstrated in [73] using a PhC cavity with two resonant modes. For a typical

L3 cavity as mentioned before, the free-spectral range, the frequency spacing between two resonant modes, is around 50 nm which makes only one resonant mode locate in the telecommunication frequency band in the PBG [71]. Therefore, a L4 cavity was used in [73] to get two resonant modes for the control light and the signal light. Although, the PhC L4 cavity was tailored to get a high quality factor, the cavity volume V is enlarged compared with the L3 cavity which results in a decreased Q/V and then a increased switching energy. Since how to increase the quality factor of the PhC cavity have already been heavily studied [149], here we investigate the possibility to further decrease the cavity size while maintaining the cavity with two resonant modes working in the telecommunication band in the PBG.

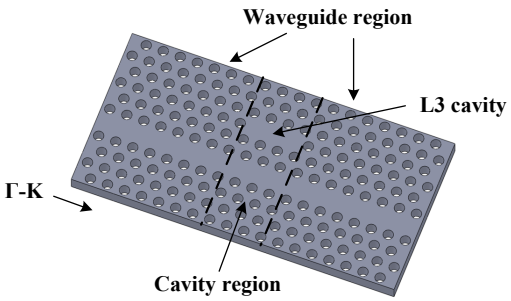

FIGURE 4.20: The schematic drawing of a dual-mode L3 PhC cavity.

Figure 4.20 shows the schematic drawing of the dual-mode L3 cavity structure which is composed by a L3 PhC cavity and a line-defect PhC waveguide. Though it is a typical basic PhC filter structure, we discovered that two resonant modes working in the desired frequency range can be obtained by this PhC structure.

Figure 4.21 (Left) shows the dispersion diagram for the structure. Here we investigate the waveguide mode in two spatial regions (waveguide region and cavity region as shown in fig. 4.20). The solid lines are the modes for the W1 waveguide region and the upper blue one shows the waveguide mode within the band-gap. Since the L3 cavity is of the size of the light wavelength, only one resonant mode is supported

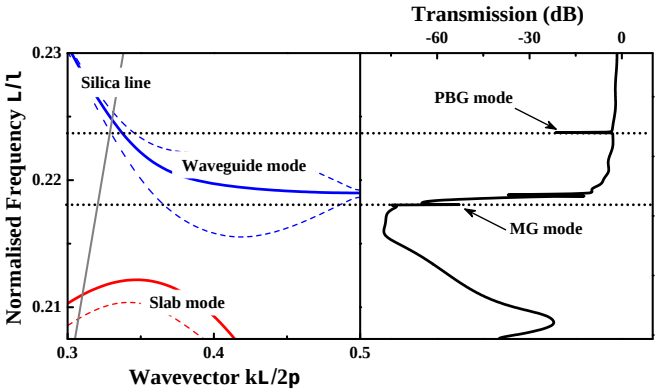

FIGURE 4.21: (Left) Dispersion diagram for the PhC structures in waveguide region (solid line) and the cavity region (dashed lines). (Right) Simulated transmission for the proposed structure calculated by CrystalWave.

within the pass band of the W1 waveguide. This mode can be seen as a dip in the transmission spectrum (see the upper dotted line in fig. 4.21(Right)). On the other hand, the cavity region can also be considered as two coupled W1 waveguides. The modes of such a coupled waveguide structure is plotted as the two blue dashed lines illustrated in the dispersion diagram (see fig. 4.21). One can see that the waveguide modes are different from those of a single W1 waveguide. In this case, photons with the specific frequency below the cut-off frequency for the waveguide region (blue solid line in fig. 4.21) can only exist in the cavity region due to the mode-gap (MG) effect [65]. Thus, the frequencies that photons can take in this cavity region become quantized due to the short length of the cavity region in the Γ-K direction. Therefore, another resonant mode is formed below the cut-off frequency of the W1 PhC waveguide as the lower dotted line shown in fig. 4.21. In this way, the dual-mode cavity with only 3 holes removing is realized and will be potential for further decreasing the switching operation energy in the relevant applications.

Figure 4.22 shows the SEM picture of the fabricated dual-mode L3 PhC cavity. The lattice constant of the structure is 380 nm and the diameter

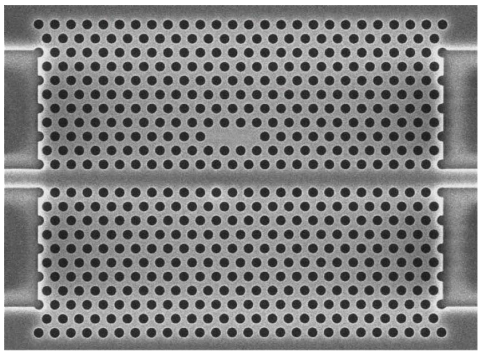

FIGURE 4.22: The SEM picture of the fabricated dual-mode L3 PhC cavity.

of the holes is 220 nm. The length of the whole PhC structure is 10 μm. Figure 4.23 shows the measured transmission spectrum of the fabricated structure. As we expected in the section 4.3.3, there is one notch above the cutoff frequency due to the PBG effect of the L3 cavity, which is denoted as PBG mode in fig. 4.23. One can also find that there is one peak below the cutoff frequency. This is the resonant mode (MG mode) due to the mode gap effect. The loaded Q factors for the two modes are 11,000 and 8,800, respectively. The Q factors are comparable to the cavity used for all-optical switching in [71, 72], but V is smaller in our L3 cavity, which makes it possible to further reduce the operation power in the all-optical switch and memory applications since the operation energy scales as V/Q^2 in the device.

For a high-Q resonator, any temperature change of the sample will lead to the variation of refractive index of the silicon material and then cause the resonance shift. Figure 4.24(a) shows this thermo-optic (TO) effect induced by changing the substrate temperatures of the sample. It is found that the PBG resonance mode is red-shifted from 1572 nm to 1576.8 nm as the temperature increased from 20^oC to 60^oC which shows that the TO effect will have a strong influence on a high-Q cavity.

In the all above measurement, the optical power was kept low during the wavelength sweeping of a TLS to avoid any nonlinear effect in the cavity. When the light intensity in the cavity increases, the enhanced

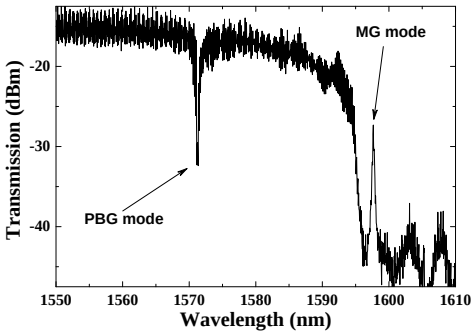

FIGURE 4.23: Measured transmission spectrum of the dual-mode L3 PhC cavity.

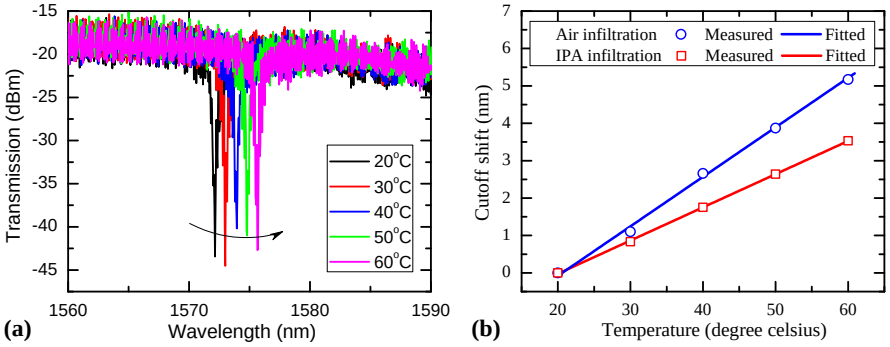

FIGURE 4.24: (a) The measured resonance red-shift of the PBG mode for the dual-mode L3 PhC cavity with different temperatures. (b) Measured resonance shift with different temperature under different holes infiltrations.

light-matter interaction will result in two-photon absorption (TPA). The free carriers generated by TPA induce a decrease of the refractive index. However, TPA also introduces heat which induce the TO effect. Normally, the strong TO effect dominates over the plasma effect. Thus, in order to observe the carrier effect, an ultra-short pulsed light source is needed to avoid the slow (in the order of a microsecond) thermal effect [99]. The carrier effect can induce optical bistability in the cavities which has been demonstrated for many applications including optical

switching, memory and fundamental logic functions, such as a flip-flop. However, the TO effect prevents the carrier-induced bistability from operating at steady state. Typically, the holding time for the steady state is less than 10 ns [99]. This hampers the applications mentioned above. Since the TO coefficient of Si material is positive, infiltration for the air holes of the PhC cavity with a liquid of a negative TO coefficient can be used to reduce the temperature dependence of the PhC cavity [150]. In our experiment, the PhC holes were infiltrated with isopropanol (IPA). Figure 4.24(b) shows the resonance (PBG mode) shift with temperature before and after the IPA infiltration. It is seen that the temperature dependency of the resonance has been decreased after the infiltration, which would make the carrier effect dominate as shown below in the measurement results.

To achieve all-optical tuning, we choose the PBG mode for the control wavelength and MG mode for the signal wavelength. As the light intensity at the PBG mode increases in the cavity, the TPA-induced free-carrier effect will change the refractive index of cavity which also affects the resonance wavelength of the MG mode.

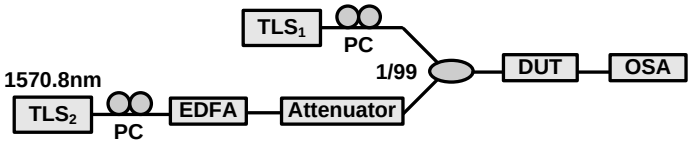

FIGURE 4.25: Experimental setup for the all-optical tuning of the dual-mode L3 PhC cavity.

Figure 4.25 shows the experimental setup. One TLS with fixed wavelength at 1570.8 nm was used as the control light. The intensity of the light was controlled by a combination of an erbium-doped fiber amplifier (EDFA) and an attenuator. Another TLS with a low power was used to sweep wavelength around the MG mode. Figure 4.26 shows the measured resonance shift for the MG mode. A clear blue-shift of 1 nm is observed by applying 13-dBm input power, which is an evidence of the dominant carrier effect induced by TPA in the proposed device since the TO effect results in a resonance red-shift. This is the first experimental

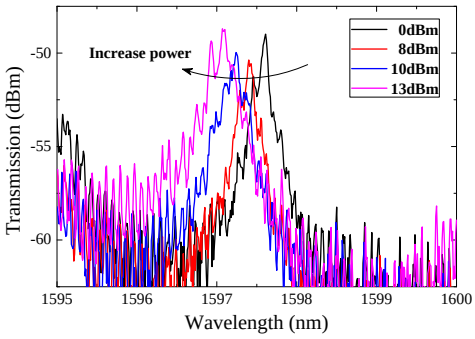

FIGURE 4.26: Measured resonance blue-shift of the mode-gap mode for the dual-mode L3 PhC cavity with different input power for the PBG mode.

demonstration of all-optical tuning by carrier effect for a silicon PhC cavity using a continuous wave (CW) laser source which will make it more practical to utilize the carrier-based bistability in some applications.

4.4 Ring-Shaped Photonic Crystal Structures

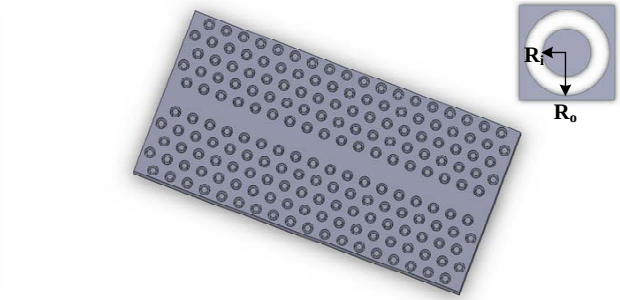

FIGURE 4.27: Schematic diagram of the RPhC waveguide.

The RPhC was proposed by H. Kurt to obtain a complete band-gap for both TE and TM modes [151, 152]. Figure 4.27 shows a RPhC

waveguide. In this type of PhC, the ring-shaped holes, which are defined by their ourter (R_o) and inner (R_i) radii, are used as the unit cell instead of circular holes in the standard PhC structures. Apart from complete bandgap characteristics, this special PhC also offers some other superior properties [153, 154] such as high refractive index sensitivity and large freedom in the dispersion engineering. Since we focus our study on the TE mode for the PhCs, we only investigate the refractive index sensitivity and dispersion engineering capability of the RPhC waveguide.

4.4.1 Transmission of Ring-Shaped Photonic Crystal Waveguide

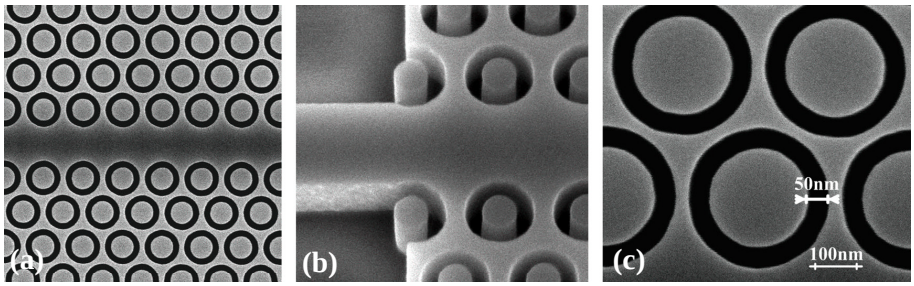

FIGURE 4.28: The SEM pictures of (a) the RPhC waveguide (R_o/Λ=0.3951, R_i/Λ=0.2222, and Λ=405 nm),(b)the connection region between ridge waveguide and the RPhC waveguide and (c) the zoomed-in ring-shaped holes of the PhC waveguide with a 50-nm ring-gap width.

Compared with the standard PhC waveguide, the ring-shaped photonic cyrstal waveguide behaves differently in the transmission measurement. Figure 4.28 shows the SEM pictures of some fabricated RPhC waveguides. Figure 4.28(a) shows the tested structure with R_o/Λ=0.3951, R_i/Λ=0.2222, and Λ=405 nm and fig. 4.28(c) shows the smallest ring-gap that can be fabricated with our technology.

Figure 4.29 shows the measured transmission of the RPhC waveguide. The cut-off wavelength of the structure is designed to be at 1546 nm which is the same as that of the previously measured standard PhC

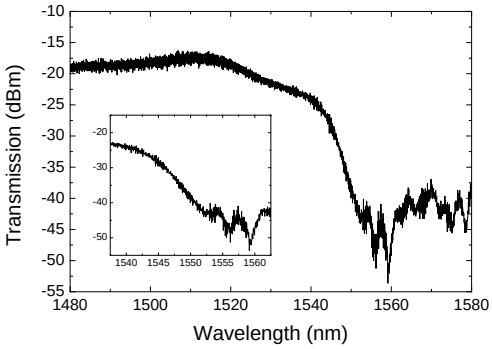

FIGURE 4.29: Measured transmission spectra of the RPhC waveguide.

waveguide. A clear intensity drop is found at the designed cut-off wavelength. However, the intensity begins decrease gradually from 1515 nm to 1540 nm and then decrease 20 dB from 1542 nm to 1550 nm. This is probably due to the different field distributions between the PhC waveguide and the RPhC waveguide. As we mentioned previously, the mode field for the RPhC waveguide penetrates much deeper into the cladding RPhC structure which make it more sensitive to the sidewall roughness of the ring-shaped holes and probably result in an increased propagation loss within a certain wavelength range. Therefore, the RPhC waveguide is not suitable for guiding light due to the large loss. Still, it could be suitable for many applications such as index sensing and slow-light engineering when the propagation loss is not the major concern.

4.4.2 Refractive Index Sensing

As mentioned in the previous section, the cut-off frequency of the waveguide mode is sensitive to the ambient refractive index for the standard PhC waveguide. Here, we compared the sensitivity between the PhC and the RPhC waveguides. The 3D simulation was performed using the MIT Photonic Bands software for both waveguides. In the simulation, R=0.324Λ was used for the PhC waveguide and R_o=0.384Λ and R_i=0.21Λ were used for the RPhC waveguide. All the geometrical parameters were chosen to ensure both waveguides have the same air filling

factor which is defined as the percentage of the air area in the silicon slab for the PhC.

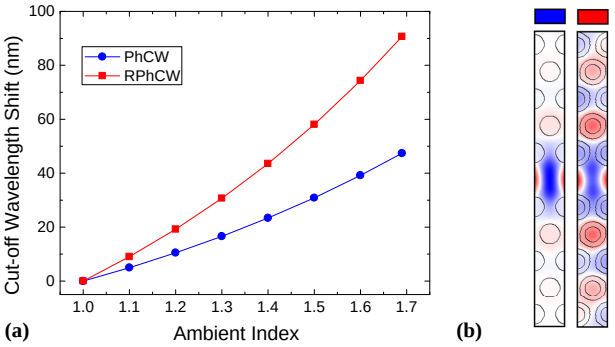

FIGURE 4.30: (a) Simulated cut-off wavelength shift as a function of the ambient refractive index for standard PhC waveguide (R=0.324Λ) and RPhC waveguide (R_o=0.384Λ and R_i=0.21Λ. (b) The mode field distribution for RPhC waveguide (right) and standard PhC waveguide (left).

Figure 4.30(a) shows the calculated cut-off wavelength shift against ambient RI change for two different waveguides. From the simulation, we find that the sensitivities of the PhC waveguide and the RPhC waveguide are 63 nm/RIU and 128 nm/RIU, respectively. The sensitivity of the RPhC waveguide is twice as large as that of the standard PhC waveguide. Since the sensitivity is determined by the overlap between the optical field of the waveguide and the ambient, we also compared the mode field distribution of the two waveguide structures at the same wavevector of 0.3 ($k\Lambda/2\pi$). From fig 4.30(b), one can find that the mode in the standard PhC waveguide mainly penetrates into the two rows of holes adjacent to the waveguide core while the mode in the RPhC waveguide penetrates highly into the cladding of the waveguide. Besides, the intensity of the mode field tends to be more localized in the ring-shaped holes than the circular holes. Therefore, a larger overlap between the optical field and the ambient in RPhC waveguide can be expected, which results in a higher index sensitivity.

Furthermore, we have also investigated the RPhC waveguides with different ring-gap widths (R_o-R_i). As fig. 4.31(a) shows, the ring-gap

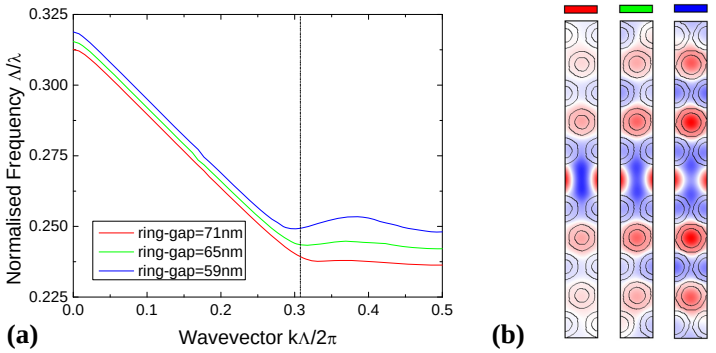

FIGURE 4.31: Simulated waveguide bands (a) and the mode filed distributions (b) for the RPhC waveguides with different ring-gap widths. by using CrystalWave (R_o=0.407Λ).

width will influence the shape and the position of the waveguide mode. These changes for the waveguide mode also make the mode field distribution different for the waveguides with different ring-gap widths as shown in fig. 4.31(b). The mode field located in the cladding RPhC became stronger for the narrower ring-gap widths which indicates that more overlap between the ambient and the field can be expected for the waveguide with small ring-gap width. Figure 4.32 shows the calculated cut-off wavelength shift for the RPhC waveguide with different ring-gap width under the water infiltration. The cut-off wavelength shift increases from 30 *nm* to 50 *nm* by decreasing the ring-gap width from 77 *nm* to 58 *nm*. It is clear that the sensitivity is very related to the dimension of the ring-shaped holes and can be further increased by using the narrower ring-gap widths.

Figure 4.33 shows the transmission spectra calculated by 3-D FDTD modelling. Spectra were calculated for four ambient refractive indices, i.e., air (n=1), water (n=1.315), ethanol (n=1.344) and isopropanol (IPA) (n=1.363) [155]. It is seen that the cut-off wavelength shifts to longer wavelength with increasing ambient refractive index as we predicted. However, the transmission curves do not show a steep drop at the cut-off wavelength. This is probably partly due to the coupling problem for the light with the special field distribution in the RPhC waveguide.

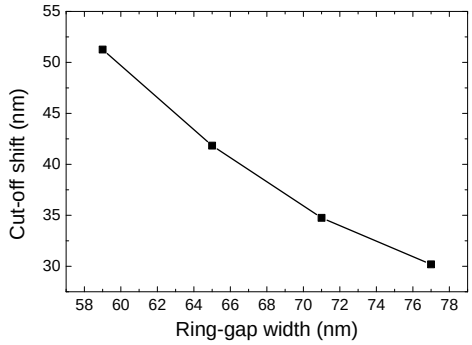

FIGURE 4.32: Simulated cut-off wavelength shift for the RPhC waveguide with different ring-gap widths with the infiltration of water. (R_o=165nm, and Λ=405 nm)

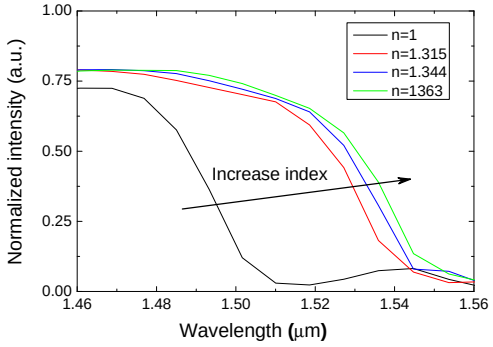

FIGURE 4.33: Simulated transmission for the RPhC waveguide by using CrystalWave. (R_o=165nm, R_i=76 nm and Λ=405 nm)

In the refractive index sensing, the RPhC waveguide offers two times larger sensitivity than the standard PhC waveguide according to the calculated result shown in fig. 4.33 in section 4.4.2. Here, we tested the RPhC waveguide with infiltrations of air, de-ionized (DI) water, ethanol and IPA.

Figure 4.34 shows the recorded transmission spectra for a fabricated RPhC waveguide with R_o=160 nm and R_i=90 nm. The measured curves in air, DI water, ethanol and IPA are shown with the black, red, blue and green solid lines, respectively. The cut-off wavelength was

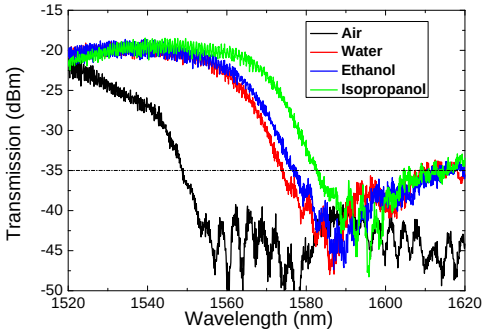

FIGURE 4.34: Measured transmission spectra of the RPhC waveguide with different infiltrations. (R_o/Λ=0.3951, R_i/Λ=0.2222, and Λ=405 nm)

read out at the transmission of -35 dB as shown with the dashed line in fig. 4.34. This cut-off wavelength of the RPhC waveguide shifted by 25.2 nm, 28.3 nm and 33.8 nm relative to that with air infiltration. As a comparison, we repeated the measurement for a standard PhC waveguide with the same air filling factor (R=123 nm, Λ=380 nm). With infiltration of the same liquids, the cut-off wavelength of the PhC waveguide shifted by 17.8 nm (water), 20.3 nm (ethanol) and 21.9 nm (IPA). It is obvious that the RPhC waveguide offers higher sensitivity.

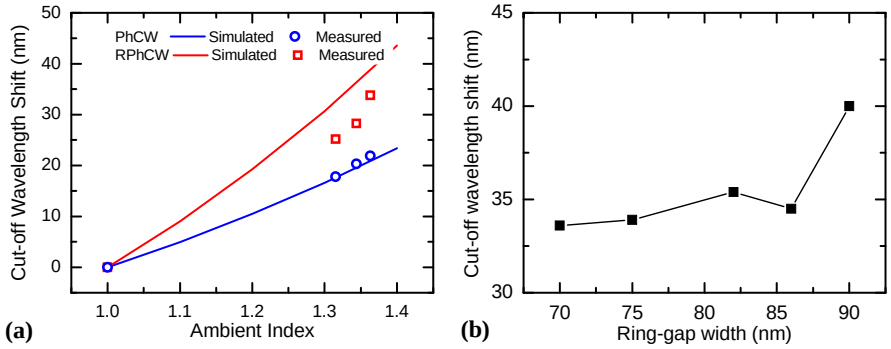

FIGURE 4.35: Measured cut-off wavelength shift with different ambient refractive index (a) (open circles and open squares) and different ring-gap width with infiltration of isopropanal.

Figure 4.35(a) shows the change of the cut-off wavelength with different ambient refractive indices. It is seen that the measured and simulated results are consistent for the PhCW, but there exists a small discrepancy for the RPhC waveguide. This is probably because the RPhC waveguide was only partially infiltrated by the liquids due to the narrow gaps of the rings and the liquid surface tension. Furthermore, the sensitivity of the RPhC waveguide with different ring-gap widths with IPA infiltration was measured, as shown in fig. 4.35(b). We observed the largest cut-off wavelength shift of 40 nm for the RPhC waveguide with 90-nm ring gap. This corresponds to a sensitivity of $\Delta\Lambda/\Delta$n=110 nm/RIU. However, contrary to the numerical prediction, the sensitivity does not increase when decreasing the ring-gap width. One possible reason is that the infiltration becomes more difficult for a narrower gap.

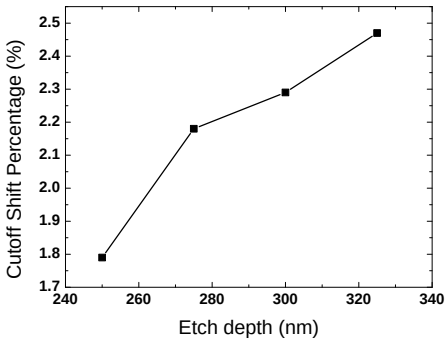

FIGURE 4.36: The simulated sensitivity for the RPhC with different etch depthes.

Additionally, the silicon material in the narrower ring-shaped holes (<90 nm) may only have been partially etched due to the RIE lag effect. Figure 4.36 shows the simulated index sensitivity for the RPhC waveguide with the same planar geometry parameters but with different etch depths. It shows that only the structure with all the silicon etched away has the highest sensitivity while the others have the degraded performances for the index sensing applications. It is obvious that the incomplete etching for the RPhC waveguide is detrimental for the sensing application. This also makes infiltration of liquid more difficult which will result in a reduced sensitivity. To further improve the sensitivity,

slight over etching for RPhC waveguides with narrow ring-gap width is necessary, and a flow-injection system [156] could be used to facilitate the liquid infiltration.

4.4.3 Topology Optimization for Slow-Light Coupling

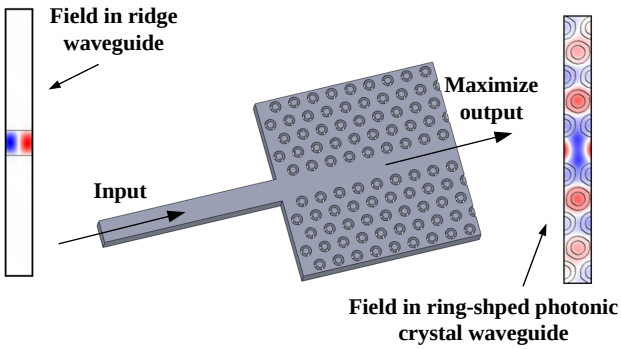

FIGURE 4.37: Schematic diagram of a RPhC waveguide butt-coupled to a ridge waveguide.

Normally, the RPhC waveguide is butt-coupled to a ridge waveguide as shown in fig. 4.37. The optical mode field distribution for the waveguide mode in the RPhC waveguie(right) and in the ridge waveguide (left) are also illustrated in fig. 4.37. The waveguide modes of the RPhC waveguide penetrate highly into the cladding of the RPhC while the modes of the ridge waveguide are highly confined in the waveguide core. Therefore, the large mode mismatch between the RPhC waveguide and the ridge waveguide makes the butt-coupling inefficient and reduces the transmission in a certain frequency range (known as the slow-light regime) close to the cut-off frequency. This so-called slow-light coupling problem was mentioned previously for the standard PhC waveguide in section 4.3.2. However, the problem for the RPhC waveguide become more severe than that of the PhC waveguide due to the deeper penetration of the mode into the cladding PhC. We applied the topology optimization (TO) technique to optimize the interface between the RPhC waveguide and the ridge waveguide to improve the coupling efficiency.

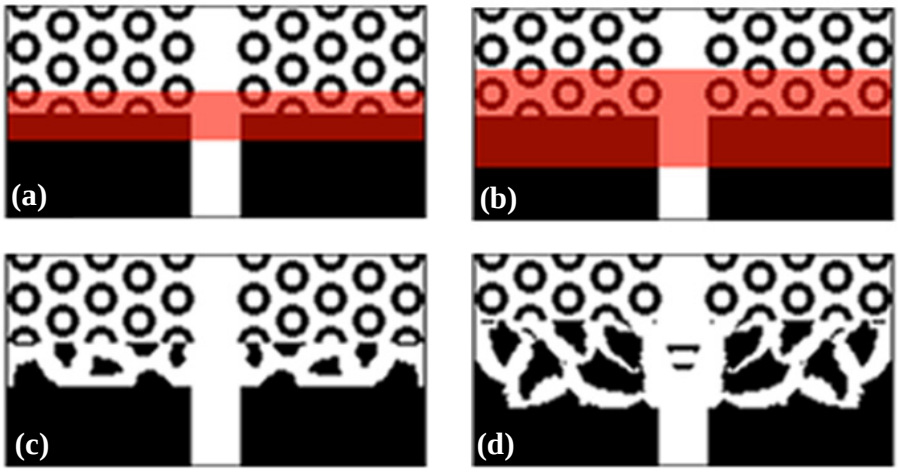

FIGURE 4.38: (a,b)Un-optimized coupling region with different design domains (red shadows) for topology optimization. (c,d) Optimized slow-light couplers for the different design domains, respectively.

The TO modelling of the waveguide is done by solving 2-D Helmholtz equations using the finite-element method. Transmission of light at two frequencies within the slow light regime were solved in each iteration and analytical sensitivities were obtained. The Method of Moving Asymptotes (MMA) [157] is used iteratively to generate a new design by modifying the refractive index in each element to maximize the wave output (see fig. 4.37). The optimization converges when the change in design is sufficiently small. The optimization is performed within the chosen design domain (see figs. 4.38(a) and (b)), which is the vicinity of the interface between the ridge waveguide and the RPhC waveguide. The resulting optimized structures for the two chosen design domains are shown in figs. 4.38(c) and (d).

To verify the performance of the TO method, 2D FDTD calculations were used to analyze the fields propagating in the RPhC waveguide in two regimes: At a wavelength far from the cut-off wavelength (in the fast-light regime, figs. 4.39(c) and (d)), and close to the cut-off wavelength (in the slow-light regime, 4.39(e) and (f)). It is seen that for

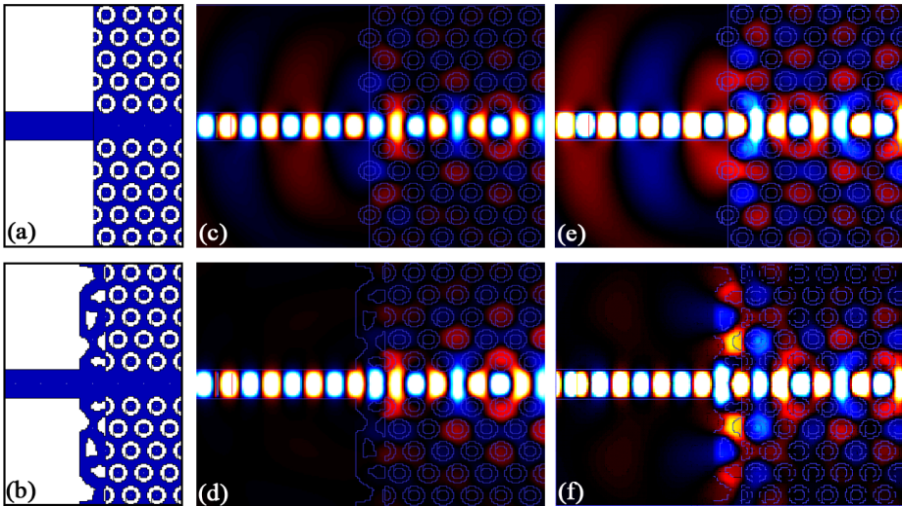

FIGURE 4.39: The un-optimized (a) and Optimized (b) coupling structures for the RPhC waveguide, and the corresponding 2D FDTD-calculated field propagations in the fast light regime (c,d) and slow light regime (e,f).

the un-optimized structure, there is a significant reflection from the edge of the RPhC waveguide (see fig. 4.39(e)) while the reflection is smaller for the short-wavelength light in the fast-light regime (see fig. 4.39(c)). Obviously, the slow light suffers more coupling loss. However, there is only little reflection both for fast light and slow light in the optimized structure (see figs. 4.39(d) and (f)). Thus, an efficient coupling can be achieved by optimizing the structure.

Figure 4.40(a) shows the simulated transmission spectra for the two structures in figs. 4.38(a) and (b) by using 3-D FDTD calculations. It is noticed that the transmittance of the RPhC waveguide is dramatically improved within a $\sim$50-nm band width by applying topology optimization to the design. Figure 4.40(b) illustrates the extracted coupling improvement in this band width and a maximum coupling enhancement of 2.3 dB is found in the vicinity of the band edge (the slow light regime).

Two slow-light couplers, shown in figs. 4.41(b) and (c), were fabricated and characterized in order to verify the efficiency of the TO method for

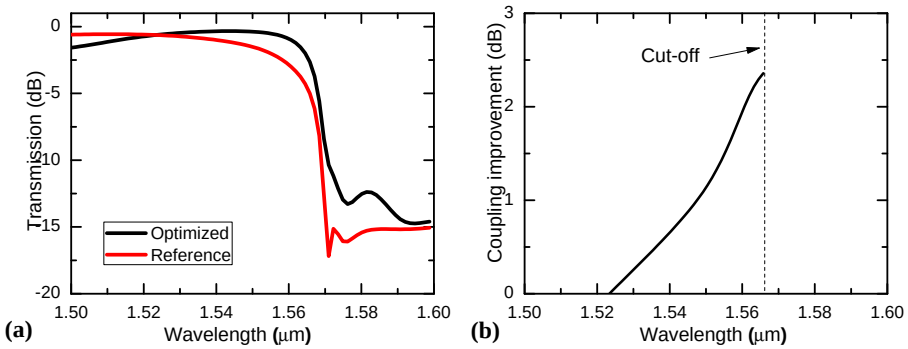

FIGURE 4.40: 3D simulated transmission spectra for the RPhC waveguide with (blue) and without (red) optimization.

design the slow-light coupler for RPhC waveguide. The fabricated RPhC waveguides are ∼5-μm long and connected to tapered ridge waveguides to route light to and from the sample facets. An RPhC waveguide with standard coupling region was also fabricated as a reference (see Fig. 4.41(a)). For each of the structures, the in- and out-coupling regions are designed and fabricated identically.

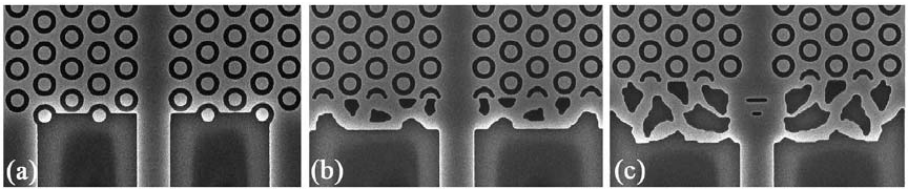

FIGURE 4.41: Scanning electron micrographs of the un-optimized (a) and two optimized (b,c) structures.

The measured transmission spectra are shown in figs. 4.42(a) and (b) for the two optimized (blue) coupling interfaces. It is clear that both optimized structures have higher coupling efficiencies near the band cut-off than the reference structures as we expected. Also shown in the figs. 4.42(c) and (d) are the extracted coupling improvements for the two couplers. An enhancement in the combined in- and out-coupling of up to 5 dB is observed in the slow-light regime close to the cut-off wavelength at ∼1600 nm for both designs. Thus, the experimental results confirmed

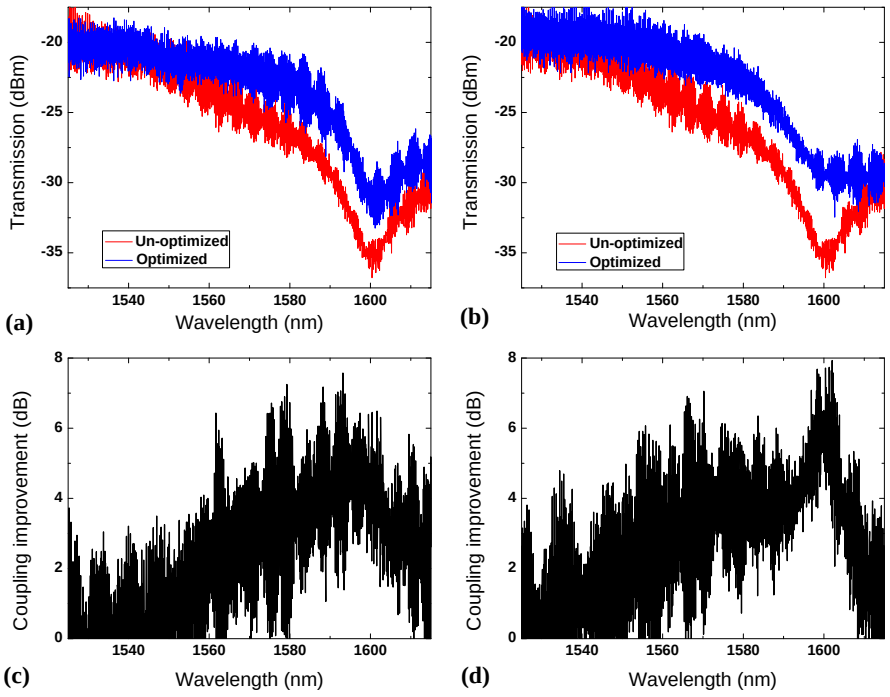

FIGURE 4.42: (a,b) Measured transmission spectra for two optimized couplers. (c,d) the extracted coupling improvement for the two couplers. ((a,c) is for fig. 4.41(b) and (b,d) is for fig. 4.41(c).

the predicted improved coupling performance of $\sim$2.5 dB per coupling of the topology-optimized slow-light interfaces.

4.4.4 Dispersion Engineering

The slow light in PhC waveguides is an interesting phenomenon which can be used in many nonlinear applications. Although a very large group index can be obtained in the standard PhC waveguide near the cut-off frequency as mentioned previously, the extremely narrow bandwidth of the large group index limits its practical applications. Thus, dispersion engineering is always necessary. For the standard PhC waveguides,

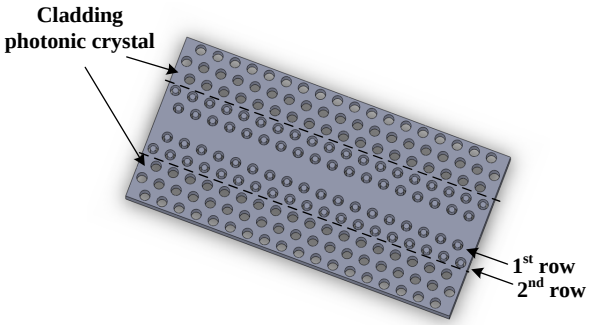

FIGURE 4.43: Schematic diagram of the ring-shaped hole perturbed PhC waveguide.

the dispersion engineering is always realized by adjusting the PhC geometries, including changing the hole sizes [136] or the hole positions [137, 138] of the first two rows of holes adjacent to the waveguide core. In these methods, there are two and one parameter, respectively, to adjust for the dispersion engineering. Here, we investigate the dispersion engineering by using a special PhC waveguide which is perturbed by introducing ring-shaped holes at the first two rows adjacent to the waveguide core as shown in fig. 4.43. This novel structure offers more freedom for the dispersion engineering and is potentially useful to further increase the delay-bandwidth product for PhC waveguide.

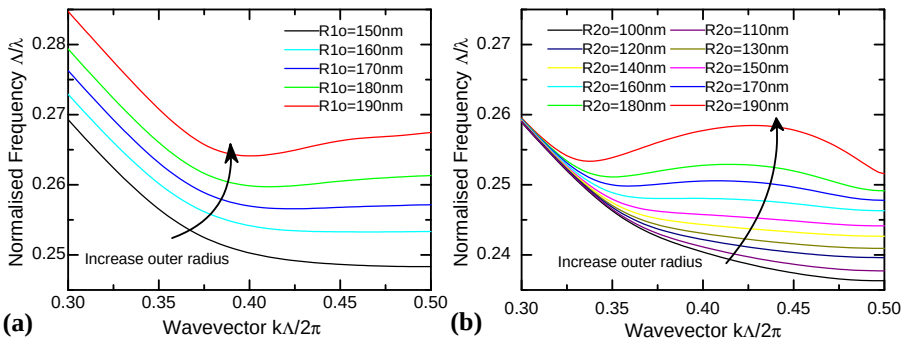

FIGURE 4.44: The simulated waveguide bands with different outer radii for the 1st (a) and 2nd (b) ring-shaped holes.

Figure 4.44 shows the waveguide modes calculated for the different radii of the ring-shaped holes at the first rows and the second rows for the perturbed RPhC waveguide. It is clear that by increasing the radius of the ring-shaped holes at the first rows, the position of the waveguide mode moves up and the tail of the mode will be bent up to some extent as shown in fig. 4.44(a). While increasing the outer radius of the ring-shaped holes at the second rows will result in another type of change: the center part of the waveguide mode will be pushed up while the left part remain almost unchanged as shown in fig. 4.44(b). In this way, the slope of the waveguide band which determines the group index can be tailored. These two engineering methods are quite similar to the methods proposed in [136].

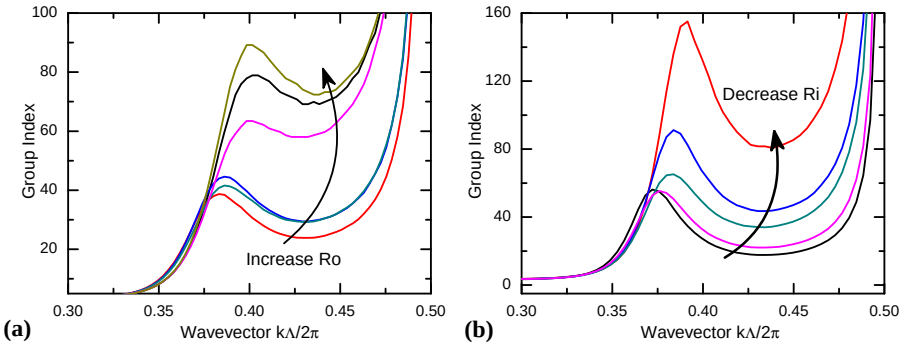

FIGURE 4.45: The calculated group index as a function of wave vector with different outer (a) and inner (b) radii of the ring-shaped holes at the first rows for the ring-shaped hole perturbed PhC waveguide.

In addition, the waveguide mode can also be tailored by changing the inner radii of the ring-shaped holes. Through the adjustment for the inner and outer radii of the ring-shaped holes, the group index at different wavevector for the waveguide could be changed. Figure 4.45 shows the calculated group index as a function of wave vector when the outer radius (a) and the inner radius (b) of the ring-shaped holes are changed only in the first rows. It is seen that the group index could reach 80 at the wave vector 0.4 by increasing the outer radius and the group index can be further increased to 160 by decreasing the inner radius. However, the group index curves are somehow in the "U" shape and do not have a uniform group index over a certain wave vector range (or wavelength

range). In order to get the broad bandwidth large group index, the diameter of the circular holes in the cladding PhC could be also adjusted. Figure 4.46 shows the group index curves with the different hole diameter for the cladding PhC structure. By decreasing the hole radius, the bottom part of the "U" shaped group index curve will be pushed up and become flat and then achieve a relatively broad bandwidth with a moderate large group index as shown in fig. 4.46.

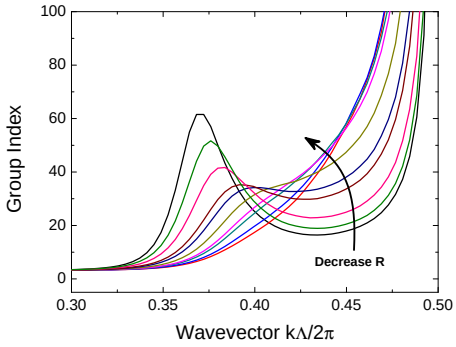

FIGURE 4.46: The calculated group index as a function of wave vector with different hole radius for the cladding PhC for the ring-shaped hole perturbed PhC waveguide.

4.5 Summary

This chapter presented the basic theory of the PhCs. The plane-wave expansion method and FDTD methods are used to calculate the dispersion relation and the transmission, respectively, for both PhC- and RPhC-based components. Since the optical performance of PhC components is very sensitive to the nano-scale dimension, the fabrication process and the relevant critical issues such as proximity effect and lag effect we discussed.

For the PhC-based components, a dual-mode L3 cavity is investigated and has been demonstrated experimentally with its carrier-based all-optical tuning operation by using a CW laser source. This special cavity is of potential use for many all-optical processing applications. For

the RPhC-based components, the perturbed RPhC waveguide provide a large freedom in the dispersion engineering. The dispersion of the waveguide band could be tailored by adjusting the outer and inner radii for ring-shaped holes and also the radius for the circular holes to obtain a relatively broadband slow-light waveguiding which make it very important in the nonlinear applications. In addition, the refractive index sensitivity of the RPhC waveguide has also been evaluated theoretically and experimentally. An index sensitivity of 110 nm/RIU for the RPhC waveguide is achieved. In order to solve the coupling problem for the light within the slow-light regime, the topology optimization method is used to design the interface between the RPhC and ridge waveguides. The optimized structures proved efficient and show an enhancement of coupling about 2.5 dB from the measurement. Above all, PhC- and RPhC-based components could play an important role in many applications for optical communication, computing, and bio-sensing.

Chapter 5

Summary and outlook

5.1 Summary

Silicon photonics, mainly based on silicon-on-insulator (SOI) has recently drew a great deal of attention. Silicon (Si) is very promising to become the mainstream host material for future photonic integrated circuits, since it is complementary metal-oxide-semiconductor (CMOS)-compatible which makes it easy to be integrated with electronic circuits. This thesis has dealt with three key silicon nano-photonic components including ridge waveguide components, microring resonators (MRRs), photonic crystal (PhC) components, and demonstrated their different applications ranging from optical communication to microwave systems and biosensing devices.

For ridge waveguide components, an inverse taper coupler for interfacing silicon ridge waveguides and optical fibers is optimized for both transverse-electric (TE) and transverse-magnetic (TM) polarizations. The inverse tapers with tip width less than 15 nm have been successfully fabricated with the help of thermal oxidation process. The insertion loss of the inverse taper coupler is measured to be $\sim$0.36 dB and $\sim$0.66 dB for TM and TE modes, respectively. To our knowledge, this is the smallest coupler loss reported so far. Due to the strong light confinement in the silicon ridge waveguide, the enhanced effective nonlinearity make

it efficient in the parametric nonlinear processes. Integrated with the inverse taper couplers, silicon ridge waveguide has been utilized in optical nonlinear signal processing based on four-wave mixing (FWM). The characterization of the ridge waveguide shows a conversion bandwidth of 18 nm and a maximum conversion efficiency of -26 dB. Ultra-high speed signal processing including error-free optical demultiplexing (1.28 $Tbit/s$-to-10 $Gbit/s$) and waveform sampling have been realized in silicon ridge waveguide for the first time.

For MRRs, microwave phase shifters based on MRR and dual-microring resonator (DMRR) are proposed. Tunable MRRs have been fabricated for the phase shifting use. In experiment, a maximum 336° radio frequency (RF) phase shifting is obtained by using a single MRR. However, the power varies dramatically during the operation. DMRR with two independently tunable resonators is then used to solve the power variation problem and increase the phase shifting range. A full 2π RF phase shift with less than 2 dB power variation has been achieved based on this scheme. Up to 270° phase shifting operation with no power variation is also achievable. The DMRR-based RF phase shifter has also been utilized to realize full tunability over a whole free spectral range (FSR) for a microwave notch filter working at 40 GHz. Other than the microwave applications, we also have employed the MRR in pulse repetition rate multiplication (PRRM) process to generate high repetition rate pulse train (40 GHz from 10 GHz) for optical communications applications.

For PhC components, an ultra-small dual-mode PhC cavity has been demonstrated. An all-optical tuning operation based on the free-carrier plasma effect is realized in this cavity utilizing a continuous wave (CW) light which shows its potentials in ultra-fast optical switch, memory and logic function. In addition, a special ring-shaped photonic crystal (RPhC) structure was studied. Compared with the standard PhC structure, superior properties are found including the high sensitivity to ambient index, highly engineerable dispersion. An index sensor based on the RPhC waveguide has been demonstrated with a sensitivity of 110 nm/RIU. The dispersion engineering for the RPhC waveguide has also been analyzed theoretically. Besides, to enhance the coupling efficiency

between the RPhC waveguide and ridge waveguide, an topology optimized coupler has been presented with 2.5 dB efficiency enhancement per connection.

5.2 Outlook

5.2.1 Nonlinear optical signal process

Nonlinear optics using silicon photonics, as a recently emerged research area, has gained increasing interests. The strong light confinement in silicon waveguides results in a high effective nonlinearity since high intensities can be achieved in the silicon core for relatively low optical powers. Furthermore, the high confinement in silicon waveguides enables the fine tuning of waveguide dispersion, which is essential for phase matching of parametric nonlinear optical processes such as FWM. The FWM-based nonlinear process allows high speed signal processing including demultiplexing, waveform sampling which have already been demonstrated in silicon ridge waveguide for ultra-high speed data rate in this thesis.

However, if we want move towards higher data rate signal processing e.g. 5.12 $Tbit/s$, the conversion bandwidth may limit the performance of our current device since narrower pulses lead to broader spectrums. Therefore, careful tuning the dispersion of the waveguide to achieve phase-matched FWM is necessary in the future's research. This optimization should not limit to the dimensions of the ridge waveguide since altering the waveguide shape also enable dispersion engineering. An alternative is rib waveguides with proper cladding structures [158]. In addition, the slow dynamics of two-photon generated free carriers in silicon may also limit its use in the higher speed signal processing. To avoid this effect, one can use a reverse-biased p-i-n diode [159] for removing the generated carriers or use slot waveguide structure [160] for confining light into a high nonlinear material with a fast electronic properties.

Other than the conventional silicon waveguide, PhC waveguide could also be a candidate for the nonlinear optical signal processing. Due to the slow light phenomenon in PhC waveguide, the nonlinear effect can be

largely enhanced [61]. In addition to providing slow light propagation, PhC waveguides can be engineered so that slow light modes present a low dispersion. Since the nonlinear processes like FWM strongly depend on both nonlinearity and the dispersive characteristics of the waveguide, PhC waveguide appears very attractive in the nonlinear applications [161].

5.2.2 Microwave photonics

Microwave photonics is an area for processing microwave and millimeter-wave signals in the optical domain. Microwave systems benefit from the characteristics of photonic components such as compact size, large bandwidth, immunity to electromagnetic interference and light weight. The phase shifters based on silicon nano-photnoic devices (MRRs) have been investigated in this thesis. Such a phase shifter has also been successfully implemented in a tunable microwave filter. However, this proposed phase shifter can not serve as a true time delay used for phased array systems, which has major impacts on many fields, including radar, communications, and radio-astronomy.

With the proposed MRR- or DMRR-based phase shifters, a true time delay operation can only be achieved in a very limited bandwidth which hampers its applications. Therefore, it is worthwhile investigating the true time delay based on high order MRR. Since coupled MRRs offers the optical buffer functionality [33], this structure could be one solution for the true time delays. Another method is separate carrier tuning technique in a side-coupled integrated spaced sequence of resonator (SCISSOR) [162]. Then the implementation of phased array antennas by using MRR-based delay line could also be very interesting topic.

Bibliography

[1] G. Moore. Cramming more components onto integrated circuits. *Electronics Mag.*, 38(8):114–117, 1965.

[2] R. A. Soref, , and J. P. Lorenzo. All-silicon active and passive guidedwave components for λ=1.3 and 1.6 μm. *IEEE J. Quantum Electron.*, 22(6):873–879, 1986.

[3] B. Schuppert, J. Schmidtchen, and K. Petermann. Optical channel waveguides in silicon diffused from gesi alloy. *Electron. Lett.*, 25 (22):1500–1502, 1989.

[4] K. K. Lee, D. R. Lim, L. C. Kimerling, J. Shin, and F. Cerrina. Fabrication of ultralow-loss si-sio2 waveguides by roughness reduction. *Opt. Lett.*, 26(23):1888–1891, 2001.

[5] A. Liu, R. Jones, L. Ling, D. Samara-Rubio, D. Rubin, O. Cohen, R. Nicolaescu, and M. Paniccia. A high-speed silicon optical modulator based on a metal-oxide-semiconductor capacitor. *Nature*, 427:615–618, 2004.

[6] W. M. Green, M. J. Rooks, L. Sekaric, and Y. A. Vlasov. Ultra-compact,low rf power, 10 gb/s silicon mach-zehnder modulator. *Opt. Express*, 15(25):17106–17113, 2007.

[7] S. Manipatruni, R. K. Dokania, B. Schmidt, N. Sherwood-Droz, C. B. Poitras, A. B. Apsel, and M. Lipson. Wide temperature range operation of micrometer-scale silicon electro-optic modulators. *Opt. Lett.*, 33(19):2185–2187, 2008.

[8] S. Manipatruni, Q. Xu, and M. Lipson. Pinip based high-speed highextinction ratio micron-size silicon electrooptic modulator. *Opt. Express*, 15(20):13035–13042, 2007.

[9] L. Chen and M. Lipson. Integrated silicon wavelength division demultiplexer with 45 ghz germanium photodetectors. *CLEO*, 2009.

[10] H. Rong, R. Jones, A. Liu, O. Cohen, D. Hak, A. Fang, and M. Paniccia. A continuous-wave raman silicon laser. *Nature*, 433: 725–728, 2005.

[11] M. W. Groenert, C. W. Leitz, A. J. Pitera, V. Yang, H. Lee, R. J. Ram, and E. A. Fitzgerald. Monolithic integration of room-temperature gaas/algaas lasers on si substrates via relaxed graded gesi buffer layers. *J. Appl. Phys.*, 93:362–367, 2003.

[12] A. W. Fang, H. Park, O. Cohen, R. Jones, M. J. Paniccia, and J. E. Bowers. Electrically pumped hybrid algainas-silicon evanescent laser. *Opt. Express*, 14:9203–9210, 2006.

[13] Intel. http://www.intel.com/pressroom/archive/releases/.

[14] X. Sun, J. Liu, L. C. Kimerling, and J. Michel. Toward a germanium laser for integrated silicon photonics. *IEEE J. Sel. Top. Quantum Electron.*, 16(1):124–131, 2010.

[15] M. A. Foster, K. D. Moll, and A. L. Gaeta. Optimal waveguide dimensions for nonlinear interactions. *Opt. Express*, 12(13):2880–2887, 2008.

[16] M. A. Foster, A. C. Turner, M. Lipson, and A. L. Gaeta. nonlinear optics in photonic nanowires. *Opt. Express*, 16(2):1300–1320, 2010.

[17] H. K. Tsang, C. S. Wong, T. K. Liang, I. E. Day, S. W. Roberts, A. Harpin, J. Drake, and M. Asghari. Optical dispersion, two-photon absorption and self-phase modulation in silicon waveguides at 1.5μm wavelength. *Applied Physics Letters*, 80:2880–2887, 2002.

[18] O. Boyraz, P. Koonath, V. Raghunathan, and B. Jalali. All optical switching and continuum generation in silicon waveguides. *Opt. Express*, 12:4094, 2004.

[19] D. Dimitropoulos, V. Raghunathan, R. Claps, and B. Jalali. Phase-matching and nonlinear optical processes in silicon waveguides. *Opt. Express*, 12:149, 2004.

[20] R. Salem, M. A. Foster, A. C. Turner, D. F. Geraghty, M. Lipson, and A. L. Gaeta. Signal regeneration using low power four-wave mixing on silicon chip. *Nature Photonics*, 2:35–38, 2008.

[21] M. A. Foster, A. C. Turner, J. E. Sharping, B. S. Schmidt, M. Lipson, and A. L. Gaeta. Broad-band optical parametric gain on a silicon photonic chip. *Nature*, 44:960–963, 2006.

[22] B. G. Lee, A. Biberman, A. C. Turner-Foster, M. A. Foster, M. Lipson, A. L. Gaeta, and K. Bergman. Demonstration of broadband wavelength conversion at 40gb/s in silicon waveguides. *IEEE Photon. Technol. Lett.*, 21:182–184, 2009.

[23] M. A. Foster, A. C. Turner, R. Salem, M. Lipson, and A. L. Gaeta. Broad-band continuous-wave parametric wavelength conversion in silicon nanowaveguides. *Opt. Express*, 15(20):12949–12958, 2007.

[24] N. Ophir, A. Biberman, A. C. Turner-Foster, M. A. Foster, M. Lipson, A. L. Gaeta, and K. Bergman. First 80-gb/s and 160-gb/s wavelength converted data stream measurements in a silicon waveguide. *Proc. Optical Fiber Communication Conference (OFC)*, page OWP5, 2010.

[25] F. Li, M. Pelusi, D. Xu, A. Densmore, R. Ma, S. Janz, and D. J. Moss. Error-free all-optical demultiplexing at 160 gbit/s via fwm in a silicon naowire. *Opt. Express*, 18(4):3905–3910, 2010.

[26] Y. Dai, X. Chen, Y. Okawachi, A. C. Turner-foster, M. A. Foster, M. Lipson, A. L. Gaeta, and C. Xu. 1μs tunable delay using parametric mixing and optical phase conjugation in si waveguides. *Opt. Express*, 17(9):7004–7010, 2009.

[27] D. Taillaert, F. Van Laere, M. Ayre, W. Bogaerts, D. Van Thourhout, P. Bienstman, and R. Baets. Grating couplers for coupling between optical fibers and nanophotonic waveguides. *Jpn. J. Appl. Phys.*, 45(1):6071–6077, 2006.

[28] Y. Tang, Z. Wang, L. Wosinski, U. Westergren, and S. He. Highly efficient nonuniform grating coupler for silicon-on-insulator nanophotonic circuits. *Opt. Lett.*, 35(8):1290–1292, 2010.

[29] F. Van Laere, G. Roelkens, M. A. Schrauwen, D. Taillaert, D. Van Thourhout, T.F. Krauss, and R. Baets. Compact and highly efficient grating couplers between optical fiber and nanophotonic waveguides. *J. Lightwave Technol.*, 25(1):151–156, 2007.

[30] V.R. Almeida, R. Panepucci, and M. Lipson. Nanotaper for compact mode conversion. *Opt. Lett.*, 28(15):1302–1304, 2003.

[31] G. Roelkens, P. Dumon, W. Bogaerts, D. Van Thourhout, and R. Baets. Efficient silicon-on-insulator fiber coupler fabricated using 248-nm-deep uv lithography. *IEEE Photon. Technol. Lett.*, 17 (12):2613–2615, 2005.

[32] T. Shoji, T. Watanabe T. Tsuchizawa, K. yamada, and H. Morita. Low loss mode size converter from 0.3μm square si wire waveguides to singlemode fibres. *Electron. Lett.*, 38(25):1669–1670, 2002.

[33] F. Xia, L. Sekaric, and Y. Vlasov. Ultracompact optical buffers on a silicon chip. *Nature Photonics*, 1:65–71, 2007.

[34] P. Dumon, G. Roelkens, W. Bogaerts, D.V. Thourhout, J. Wouters, S. Beckx, P. Jaenen, and R. Baets. Basic photonic wire components in silicon-on-insulator. *Group IV Photonics*, pages 189–191, 2005.

[35] S. Xiao, M. H. Khan, H. Shen, and M. Qi. A highly compact third-order silicon microring add-drop filter with a very large free spectral range, a flat passband and a low delay dispersion. *Opt. Express*, 15:14765–14771, 2007.

[36] Q. Xu, D. Fattal, and R. G. Beausoleil. Silicon microring resonators with 1.5-μm radius. *Opt. Express*, 16(6):4309–4315, 2008.

[37] O. Schwelb. Transmission, group delay, and disperison in single-ring optical resonators and add/drop filters-a tutorial overview. *IEEE Journal of Lightwave Technology*, 22(5):1380, 2004.

[38] M. S. Nawrocka, T. Liu, X. Wang, and R. R. Panepucci. Tunable silicon microring resonator with wide free spectral range. *Appl. Phys. Lett.*, 89:071110, 2006.

[39] Q. Xu, S. Manipatruni, B. Schmidt, J. Shakya, and M. Lipson. 12.5 gbit/s carrier-injection-based silicon micro-ring silicon modulators. *Opt. Express*, 15:430–436, 2007.

[40] V. R. Almeida, C. A. Barrios, R. R. Panepucci, and M. Lipson. All-optical control of light on a silicon chip. *Nature*, 431:1081–1083, 2004.

[41] Q. Xu, B. Schmidt, J. Shakya, and M. Lipson. Cascaded silicon micro-ring modulators for wdm optical interconnection. *Opt. Express*, 14:9431–9435, 2006.

[42] M. Forst, J. Neihusmann, T. Plotzing, J. Bolten, T. Wahlbrink, C. Moormann, and H. Kurz. High-speed all-optical switching in ion-implanted silicon-on-insulator microring resonators. *Opt. Lett.*, 32(14):2046–2048, 2007.

[43] M. Waldow, T. Plotzing, M. Gottheil, M. Forst, J. Bolten, T. Wahlbrink, and H. Kurz. 25ps all-optical switching in oxygen implanted silicon-on-insulator microring resonator. *Opt. Express*, 16(11):7693–7702, 2008.

[44] L. Zhang, J. Y. Yang, M. Song, Y. Li, B. Zhang, R. G. Beauoleil, and A. E. Willner. microring-based modulation and demodulation of dpsk signal. *Opt. Express*, 15:11564–11569, 2007.

[45] L. Zhou, H. Chen, and A. W. Poon. On-chip nrz-to-prz format conversion using narrow-band silicon microring resonatro-based notch filters. *Journal of Lightwave Technology*, 26:1950–1955, 2008.

[46] A. J. Seeds and K. J. Williams. Microwave photonics. *IEEE/OSA Journal of Lightwave Technology*, 24(12):4628–4641, December 2006.

[47] J. Capmany and D. Novak. Microwave photonics combines two worlds. *Nature Photonics*, 1:319–330, June 2007.

[48] A. Loayssa and F. J. Lahoz. Broad-band rf photonic phase shifter based on stimulated brillouin scattering and single-sideband modulation. *IEEE Photon. Technol. Lett.*, 18(1):208–210, 2006.

[49] W. Xue, S. Sales, J. Capmany, and J. Mørk. Microwave phase shifter with controllable power response based on slow- and fast-light effects in semiconductor optical amplifiers. *Opt. Lett.*, 34(7): 929–931, 2009.

[50] M. R. Fisher and S. L. Chuang. A microwave photonic phase shifter based on wavelength conversion in a dfb laser. *IEEE Photon. Technol. Lett.*, 18(16):1714–1716, 2006.

[51] S.T. Goldstein, D. Dolfi, A. Monsterleet, S. Formont, J. Chazelas, and J. P. Huignard. Optical signal processing in radar systems. *IEEE Trans. Microw. Theory Tech.*, 54:847–853, 2006.

[52] J. Capmany, B. Ortega, D. pastor, and S. Sales. Discrete-time optical processing of microwave signals. *J. Lightwave Technol.*, 23:702–723, 2005.

[53] E. Yablonovitch. Inhibited spontaneous emission in solid state physics and electronics. *Phys. Rev. Lett.*, 58:2059, 1987.

[54] E. Yablonovitch. Photonic band-gap structures. *J. Opt. Soc. Amer. B, Opt. Phys.*, 10:283–296, 1993.

[55] J. D. Joannopoulos, P. R. Villeneuve, and S. Fan. Photonic crystals: putting a new twist on light. *Nature*, 386:143–149, 1997.

[56] A. Blanco, E. Chomski, S. Grabtchak, M. Ibisate, S. John, S. W. Leonard, C. Lopez, F. Meseguer, H. Miguez, J. P. Mondla, G. A. Ozin, O. Toader, and H. M. Van Driel. Large-scale synthesis of a silicon photonic crystal with a complete three-dimensional bandgap near 1.5 micrometres. *Nature*, 405:437–440, 2000.

[57] S. Noda, K. Tomoda, N. Yamamoto, and A. Chutinan. Full three-dimensional photonic bandgap crystals at near-infrared wavelengths. *Science*, 289:604–606, 2000.

[58] S. Fan, S. G. Johnson, J. D. Joannopoulos, C. Manolatou, and H. A. Haus. Waveguide branches in photonic crystals. *J. Opt. Soc. Am. B*, 18:162–165, 2001.

[59] E. Chow, S.Y. Lin, J. R. Wendt, S. G. Johnson, and J. D. Joannopoulos. Quantitative analysis of bending efficiency in photonic-crystal waveguide bends at $\lambda = 1.55$ μm wavelengths. *Opt. Lett.*, 26:286–288, 2001.

[60] P. R. Villeneuve S. Fan and J. D. Joannopoulos. Theoretical analysis of channel drop tunneling processes. *Phys. Rev. B*, 59:15882–15892, 1999.

[61] M. Soljacic and J. D. Joannopoulos. Enhancement of nonlinear effects using photonic crystals. *Nature Mater.*, 3:211–219, 2004.

[62] T. Baba. Slow light in photonic crystals. *Nature Photonics*, 2: 465–473, 2008.

[63] E. Kuramochi, M. Notomi, M. Mitsugi, A. Shinya, and T. Tanabe. Ultrahigh-q photonic crystal nanocavities realized by the local width modulation of a line defect. *Appl. Phys. Lett.*, 88:041112, 2006.

[64] T. Asano, B. S. Song, and S. Noda. Analysis of the experimental q factors ($\sim$1 million) of photonic crystal nanocavities. *Opt. Express*, 14:1996–2002, 2006.

[65] B. S. Song, S. Noda, T. Asano, and Y. Akahane. Ultra-high-q photonic double-heterostructure nanocavity. *Nat. Mater.*, 4:207–210, 2005.

[66] B. S. Song, S. Noda, and T. Asano. Photonic devices based on in-plane heterophotonic crystals. *Science*, 300:1537, 2003.

[67] M. Lončar, A. Scherer, and Y. Qiu. Photonic crystal laser sources for chemical detection. *Appl. Phys. Lett.*, 82(26):4648–4650, 2003.

[68] O. Painter, R.K. Lee, A. Scherer, A. yariv, J. D. O′Brien, P. D. Dapkus, and I. Kim. Two-dimensional photonic band-gap defect mode laser. *Science*, 284:1819–1821, 1999.

[69] P. michler, A. Kiraz, C. Becher, W. V. Schoenfeld, P. M. Petroff, L. Zhang, E. Hu, and A. Imanoğlu. A quantum dot single-photon turnstile device. *Science*, 290:2282–2285, 2000.

[70] M. F. Yanik and S. Fan. Stopping light all optically. *Phys. Rev. Lett.*, 92(8):083901–1–083901–4, 2004.

[71] T. Tanabe, M. Notomi, S. Mitsugi, A. Shinya, and E. Kuramochi. All-optical switches on a silicon chip realized using photonic crystal nanocavities. *Appl. Phys. Lett.*, 87:151112–1–151112–3, 2005.

[72] T. Tanabe, M. Notomi, S. Mitsugi, A. Shinya, and E. Kuramochi. Fast bistable all-optical switch and memory on a silicon photonic crystal on-chip. *Optics Lett.*, 30(19):2575–2577, October 2005.

[73] M. Notomi, A. Shinya, S. Mitsugi, G. Kira, E. Kuramochi, and T. Tanabe. Optical bistable switching action of si high-q photonic-crystal nanocavities. *Optics Express*, 13(7):2678–2687, April 2005.

[74] R. Ahmad, F. Pizzuto, G. Camarda, R. Espinola, H. Rao, and R. Osgood. Ultracompact corner-mirrors and t-brannches in silicon-on-insulator. *IEEE Photon. Technol. Lett.*, 14:689–691, 2003.

[75] B. Little, J. Foresi, G. Steinmeyer, E. Thoen, S. Chu, H. Haus, E. Ippen, L. Kimerling, and W. Greene. Ultra-compact si-sio2 microring resonator optical channel dropping filters. *IEEE Photon. Technol. Lett.*, 10:8212–8222, 1998.

[76] H. Fukuda, T. Watanabe, J. Takahashi, M. Takahashi, T. shoji, E. Tamechika, S. Itabashi, T. Tsuchizawa, K. Yamada, and H. Morita. Microphotonics devices based on silicon microfabrication technology. *IEEE J. Sel. Top. Quantum Electron.*, 11:232–240, 2005.

[77] Y. A. Vlasov and S. J. McNab. Losses in single-mode silicon-on-insulator strip waveguides and bends. *Opt. Express*, 12(8):1622–1631, 2003.

[78] J. D. Jackson. *Classical Electrodynamics*. 1962.

[79] E. a. J. Marcatili. Dielectric rectangular waveguide and directional coupler for integrated optics. *Bell System Technical Journal*, pages 2071–2102, 1969.

[80] K. Okamoto. *Fundamentals of Optical Waveguides*. 2000.

[81] M. Lohmeyer. Vectorial wave-matching mode analysis of integrated optical devices. *Optical and Quantum Electronics*, 30:385–396, 1998.

[82] A. Taflove and S. C. Hagness. *Computational Electrodynamics: The Finite-Difference Time-Domain Method*. 2005.

[83] M. K. Smit and C. V. Dam. Phasar-based wdm-devices: principles, design and applications. *IEEE Journal of Selected Topics in Quantum Electronics*, 2(2):236–250, 1996.

[84] A. W. Snyder and J. D. Love. *Optical Waveguide Theory*. 1983.

[85] C. R. Pollock and M. Lipson. *Integrated Photonics*. 2003.

[86] G. P. Agrawal. *Nonlinear Fiber Optics*. 1989.

[87] W. D. Cort, J. Beeckman, R. James, F. A. Fernandez, R. Baets, and K. Neyts. Tuning of silicon-on-insulator ring resonators with liquid crystal cladding using the longitudinal field component. *Opt. Lett.*, 34(13):2054–2056, 2009.

[88] T. Xu, N. Zhu, M. Y. Xu, L. Wosinski, J. S. Aitchison, and H. E. Ruda. Pillar-array based optical sensor. *Opt. Express*, 18:5420–5425, 2010.

[89] H. C. Hansen Mulvad, L. K. Oxenløwe, M. Galili, A. T. Clausen, L. Gruner-Nielsen, and P. Jeppesen. 1.28 tbit/s single-polarisation otdm-ook data generation and demux. *Electronics Letters*, 45(5): 280–281, 2009.

[90] H. Ji, L. K. Oxenløwe, M. Galili, K. Rottwitt, P. Jeppesen, and L. Gruner-Nielsen. Fiber optical trap deposition of carbon nanotubes on fiber end-faces in a modelocked laser. *Proceedings of CLEO*, page CtuV4, 2008.

[91] S. E. Miller. Integrated optics: An introduction. *Bell Labs Technical Journal*, 48:2059–2061, 1969.

[92] E. A. J. Marcatili. Bends in optical dielectric guides. *Bell Labs Technical Journal*, 48:2103–2132, 1969.

[93] B. C. Pile and G. W. Taylor. An investigation of the operation and performance of coherent microwave photonic filters. *IEEE Trans. Microw. Theory Tech.*, 57(2):487–495, 2009.

[94] A. Meijerink, C. G. H. Roeloffzen, R. Meijerink, L. Zhuang, D. A. I. Marpaung, M. J. Bentum, M. Burla, J. Verpoorte, P. Jorna, A. Hulzinga, and W. V Etten. *Journal of Lightware Technology*, (1):3–18, Title = Novel ring resonator–based integrated photonic beamformer for broadband phased array receive antennas–part I: design and performance analysis, Volume = 28, Year = 2010.

[95] L. Zhuang, C. G. H. Roeloffzen, A. Meijerink, R. Meijerink, D. A. I. Marpaung, A. Leinse, M. Hoekman, R. G. Heideman, and W. V Etten. Novel ring resonator-based integrated photonic beamformer for broadband phased array receive antennas-part ii: experimental prototype. *Journal of Lightware Technology*, 28(1): 19–31, 2010.

[96] R. Jakoby, P. Scheele, S. Muller, and C. Weil. Nonlinear dielectrics for tunable microwave components. *15th International Conference on Microwaves, Radar and Wireless Communications*, 2:369–378, 2004.

[97] A. Yariv. Universal relations for coupling of optical power between microresonators and dielectric waveguides. *Electronics Letters*, 36 (4):321–322, EL.

[98] J. C. Slater. *Microwave electronics*. 1950.

[99] Q. Xu and M. Lipson. Carrier-induced optical bistability in silicon ring resonators. *Optics Letters*, 31:341–343, 2006.

[100] G. Qi, J. Yao, J. Seregelyi, S. Paquet, and C. Belisle. Generation and distribution of a wide-band continuously tunable millimeter-wave signal with an optical external modulation technique. *IEEE Trans. Microw. Theory Tech.*, 53:3090–3097, 2005.

[101] W. Xue, S. Sales, J. Mork, and J. Capmany. Widely tunable microwave photonic notch filter based on slow and fast light effects. *IEEE Photon. Technol. Lett.*, 21:167–169, 2009.

[102] J. Capmany, B. Ortega, and D. Pastor. A tutorial on microwave photonic filters. *J. of Lightw. Technol.*, 24:201–229, 2006.

[103] R. Levy and S. B. Cohn. A history of microwave filter research, design and development. *IEEE Transactions on Microwave Theory and Technique*, 32(9):1055–1067, September 1984.

[104] R. W. Simon, R. B. Hammond, S. J. Berkowitz, and B. A. Willemsen. Superconducting microwave filter systems for cellular telephone base stations. *Proceedings of the IEEE*, 92(10):1585–1596, October 2004.

[105] D. Dolfi, J. Tabourel, O. Durand, V. Laude, and J. Huignard. Optical architectures for programmable filtering and correlation of microwave signals. *IEEE Trans. Microw. Theory Tech.*, 45: 1467–1472, 1997.

[106] D. Pastor, J. Capmany, and B. Ortega. Broadband tunable microwave transversal notch filter based on tunable uniform fiber bragg gratings as slicing filters. *IEEE Photon. Technol. Lett.*, 13: 726–728, 2001.

[107] F. Coppinger, S. Yegnanarayanan, P. D. Trinh, B. Jalali, and I. L. Newberg. Nonrecursive tunable photonic filter using wavelength-selective true time delay. *IEEE Photon. Technol. Lett.*, 8:1214–1216, 1996.

[108] Z. Wang, K.S. Chiang, and Q. Liu. Microwave photonic filter based on circulating a cladding mode in a fiber ring resonator. *Opt. Letters*, 35:769–771, 2010.

[109] M. Pu, L. Liu, W. Xue, Y. Ding, L.H. Frandsen, H. Ou, K. Yvind, and J.M. Hvam. Tunable microwave phase shifter based on silicon-on-insulator microring resonator. *IEEE Photon. Technol. Lett.*, 22 (12):869–871, 2010.

[110] M. Pu, L. Liu, W. Xue, Y. Ding, H. Ou, K. Yvind, and J.M. Hvam. Widely tunable microwave phase shifter based on silicon-on-insulator dual-microring resonator. *Opt. Express*, 18(6):6172–6182, 2010.

[111] A. M. Weiner. Femtosecond optical pulse shaping and processing. *Prog. Quantum Electron.*, 19:161–237, 1995.

[112] S. Kawanishi. Ultrahigh-speed optical time-division-multiplexed transmission technology based on optical signal processing. *IEEE J. Quantum Electron.*, 34(11):2064–2079, 1998.

[113] K.Yiannopoulos, K. Vyrsokinos, E. kehayas, N. Pleros, K. Vlachos, H. Avramopoulos, and G. Guekos. Rate multiplication by double-passing fabry-perot filtering. *IEEE Photonics Technology Letters*, 15:1294–1296, 2003.

[114] P. Petropoulos, M.Ibsen, M.N.Zervas, , and D.J. Richardson. Generation of a 40-ghz pulse stream by pulse multiplication with a sampled fiber bragg grating. *Opt. Lett.*, 25:521–523, 2000.

[115] L. H. Frandsen. Fabrication and characterization of photonic bandgap components. *Ph.D Thesis*, March 2006.

[116] T. H. P. Chang. Proximity effect in electron-beam lithography. *J. Vac. Sci. Technol.*, 12(6):1271–1275, Nov./Dec. 1975.

[117] R. W*ü*est, F. Robin, P. Strasser, H. J*ä*ckel, and D. Erni. Influence of proximity effects in electron-beam lithography on the optical properties of planar photonic-crystal waveguides. *Journal of Applied Physics*, 102(8):083110, Oct. 2007.

[118] R. W*ü*est, P. Strasser, M. Jungo, F. Robin, D. Erni, and H. J*ä*ckel. An efficient proximity-effect correction method for electron-beam patterning of photonic-crystal devices. *Microelectronic Engineering*, 67-68:182–188, Jun. 2003.

[119] H. Jansen, M. D. Boer, R. Wiegerink, N. Tas, E. Smulders, C. Neagu, and M. Elwenspoek. Rie lag in high aspect ratio trench etching of silicon. *Microelectronic Engineering.*, 35(7):45–50, April 1997.

[120] S. G. Johnson and J. D. Joannopoulos. Proximity effect in electron-beam lithography. *Opt. Express*, 8(3):173–190, 2001.

[121] A. Toflove. *Advances in Computational Electrodynamics, Teh Finite Difference Time Domain Method.* 1998.

[122] J. D. Joannopoulos, R. D. Meade, and J. N. Winn. *Photonic Crystals, Molding the flow of light.* 1995.

[123] A. J. Ward and J. B. Pendry. A program for calculating photonic band structures, green's functions and transmission/reflection coefficients using a non-orthogonal fdtd method. *Computer Physics Communications*, 128(3):590–621, 2000.

[124] A. Lavrinenko, P. I. Borel, L. H. Frandsen, M. Thorhauge, A. Harpøth, M. Kristensen, T. Niemi, and H. M. H. Chong. Comprehensive fdtd modelling of photonic crystal waveguide components. *Opt. Express*, 12(2):234–248, 2004.

[125] N. Skivesen, A. Têtu, M. Kristensen, J. Kjems, L.H. Frandsen, and P.I. Borel. Photonic-crystal waveguide biosensor. *Opt. Express*, 15 (6):3169–3176, 2007.

[126] M. Soljacic, S. G. Johnson, S. Fan, M. Ibanescu, E. Ippen, and J. D. Joannopoulos. Photonic-crystal slow-light enhancement of nonlinear phase sensitivity. *Journal of the Optical Society of America B (Optical Physics)*, 19(9):2052–2060, 2002.

[127] N. Notomi, K. Yamada, A. Shinya, J. Takahashi, C. Takahashi, and I. Yokohama. Extremely large group-velocity dispersion of line-defects waveguides in photonic crystal slabs. *Physical Review Letters*, 87(25):253902, 2001.

[128] M. Soljacic and J. D. Joannopoulos. Enhancement of nonlinear effects using photonic crystals. *Nature Materials*, 3(4):211–219, 2004.

[129] S.I. Inoue and Y. Aoyagi. Design and fabrication of tow-dimensional photonic crystals with predetermined nonlinear optical properties. *Physical Review Letters*, 94(10):1–4, 2005.

[130] R. Jacobsen, K. Andersen, P. I. Borel, J. F. Pedersen, L. H. Frandsen, O. Hanse, M. Kritensen, A. Lavrinenko, G. Moulin, H. Ou, C. Peucheret, B. Zsigri, and A. Bjarklev. Strained silicon as a new electro-optic material. *Nature*, 441:199–202, 2006.

[131] M. F. Yanik, W. Suh, Z. Wang, and S. Fan. Stopping light in a waveguide with an all-optical analog of elecromagetically induced transparency. *Physical Review Letters*, 93(23):233903–4, 2004.

[132] Y. A. Vlasov, M. O. Boyle, H. F. Hamann, and S. J. MaNab. Active control of slow light on a chip with photonic crystal waveguides. *Nature*, 438(7064):65–69, 2005.

[133] H. Altug and J. Vuckovic. Photonic crystal nanocavity array laser. *Optics Express*, 13:8819–8828, 2005.

[134] A. Y. Petrov and M. Eich. Efficient approximation to calculate time delay and dispersion in linearly chirped periodical microphotonic strucutres. *IEEE Journal of Quantum Elctronics*, 41(12): 1502–1509, 2005.

[135] A. Y. Petrov and M. Eich. Dispersion compensation with photonic crystal line-defect waveguides. *IEEE Journal on Selected Areas in Communications*, 23(7):1396–1401, 2005.

[136] L. H. Frandsen, A. B. Lavrinenko, J. Fage-Pedersen, and P. I. Borel. Photonic crystal waveguides with semi-slow light and tailored dispersion properties. *Optics Express*, pages 9444–9450, October 2006.

[137] J. Li, T. P. White, L. O'Faolain, A. Gomez-Iglesias, and T. F. Krauss. Systematic design of flat band slow light in photonic crystal waveguides. *Opt. Express*, 16(9):6227–6232, April 2008.

[138] Y. Hamachi, S. Kubo, and T. Baba. Slow light with low dispersion and nonlinear enhancement in a lattice-shifted photonic crystal waveguide. *Opt. Lett.*, 34(7):1072–1074, April 2009.

[139] Y.A. Vlasov and S. J. McNab. Coupling into the slow light mode in slab-type photonic crystal waveguides. *Optics Letters*, 31:50–52, 2006.

[140] E. Miyai and S. Noda. Structural dependence of coupling between a two-dimensional photonic crystal waveguide and a wire waveguide. *Journal of the Optical Society of America B (Optical Physics)*, 21(1):67–72, 2005.

[141] R. Baets, P. Bienstman, P. Dumon, B. Luyssaert, J. Mart, and P. Sanchis. Analysis and design of efficient coupling in photonic crystal circuits. *Optical and Quantum Elctronics*, 37(1-3):133–137, 2005.

[142] P. Kramper, M. Agio, C. M. Soukoulis, A. Birner, F. Muller, R. B. Wehrspohn, U. Gosele, and V. Sandoghdar. Highly directional emission from photonic crystal waveguides of subwavelength width. *Physical Review Letters*, 92(11):113903–4, 2004.

[143] M. P. Bendsøe and O. Sigmund. *Topology optimization-Theory, Methods and Applications*. 2003.

[144] P. Borel, A. Harpøth, L.H. Frandsen, M. Kristensen, P. Shi, J. Jensen, and O. Sigmund. Topology optimization and fabrication of photonic crystal structures. *Optics Express*, 12(1-3):1996–2001, May 2004.

[145] S. Noda, A. Chutinan, and M. Imada. Trapping and emission of photons by a single defect in a photonic bandgap structure. *Nature*, 407:608–610, 2000.

[146] H. Takano, Y. Akahane, T. Asano, and S. Noda. In-plane-type channel drop filter in a two-dimensional photonic crystal slab. *Appl. Phys. Lett.*, 84(13):2226–2228, 2004.

[147] H. Takano, B. S. Song, T. Asano, and S. Noda. Highly efficient in-plane channel drop filter in a two-dimensional heterophotonic crystal. *Appl. Phys. Lett.*, 86:241101–1–241101–3, 2004.

[148] H. Takano, Y. Akahane, T. Asano, and S. Noda. High-q photonic nanocavity in a two-dimensional photonic crystal. *Nature*, 425: 944–947, 2003.

[149] T. Asano, B. S. Song, Y. Akahane, and S. Noda. Ultrahigh-q nanocavities in two-dimensional photonic crystal slabs. *IEEE Journal of Selected Topics in Quantum Electronics*, 12:1123–1134, 2006.

[150] C. L. C. Smith C. Karnutsch, A. Graham, S. Tomljenovic-Hanic, R. McPhedran, B. J. Eggleton, L. O′Faolain, T. F. Krauss, S. Xiao, and N. A. Mortensen. Carrier-induced optical bistability in silicon ring resonators. *Applied Physics Letters*, 94:231114–1–231114–3, 2009.

[151] H. Kurt and D. S. Citrin. Annular photonic crystals. *Optics Express*, 13(25):10316–10326, 2005.

[152] H. Kurt, R. Hao, Y. chen, J. Feng, J. Blair, D. P. Gaillot, C. Summers, D. S. Citrin, and Z. Zhou. Design of annular photonic crystal slabs. *Optics Express*, 33(14):1614–1616, 2008.

[153] A. Säynätjoki, M. Mulot, K. Vynck, D. Cassagne, J. Ahopelto, and H. Lipsanen. Properties, applications and fabrication of photonic crystals with ring-shaped holes in silicon-on-insulator. *Photonics and Nanostructures - Fundamentals and Applications*, 6: 42–46, 2007.

[154] A. Säynätjoki, M. Mulot, J. Ahopelto, and H. Lipsanen. Dispersion engineering of photonic crystal waveguides with ring-shaped holes. *Optics Express*, 15:8323–8328, 2007.

[155] C. Kim and C. B. Su. Measurement of the refractive index of liquids at 1.3 and 1.5 micron using a fibre optic fresnel ratio meter. *Meas. Sci. Technol.*, 15:1683–1686, 2004.

[156] K. D. Vos, I. Bartolozzi, E. Schacht, P. Bienstman, and R. Baets. Silicon-on-insulator microring resonator for sensitive and label-free biosensing. *Opt. Express*, 15:7610–7615, 2007.

[157] K. Svanberg. The method of moving asymptotes: a new method for structural optimization. *Int. J. Numer. Meth. Engng.*, 24:359–373, 1987.

[158] A. C. Turner-Foster, M. A. Foster, R. Salem, A. L. Gaeta, and M. Lipson. Frequency conversion over two-thirds of an octave in silicon nanowaveguides. 18(3):1904–1908, 2010.

[159] Y. H. Kuo, H. Rong, V. Sih, S. Xu, , M. Paniccia, and O. Cohen. Demonstration of wavelength conversion at 40gb/s data rate in silicon waveguides. *Opt. Express*, 14(24):11721–11726, 2006.

[160] C. Koos, P. Vorreau, T. Vallaitis, P. Dumon, W. Bogaerts, R. Baets, B. Esembeson, I. Biaggio, T. michinobu, F. Diederich, W. Freude, and J. Leuthold. All-optical high-speed signal processing with silicon-organic hybrid slot waveguides. *Nature Photonics*, 3:216–219, 2009.

[161] M. Ebnali-Heidari, C. Monat, C. Grillet, and M. K. Moravvej-Farshi. A proposal for enhancing four-wave mixing in slow light engineered photonic crystal waveguides and its application to optical regeneration. *Opt. Express*, 17(20):18340–18353, 2009.

[162] Paul A. Morton and Jacob B. Khurgin. Microwave photonic delay line with separate tuning of optical carrieer. *IEEE Photon. Technol. Lett.*, 21(22):1686–1688, 2009.